University of Alberta

Electromagnetic Energy and Data Transfer for Low-Power Implantable Biomedical Devices

by

Navid Rezaei Sarchoghaei

A thesis submitted to the Faculty of Graduate Studies and Research in partial fulfillment of the requirements for the degree of

Master of Science

in

Communications

Department of Electrical and Computer Engineering

Fall 2013
Edmonton, Alberta

To my beloved wife

and

my dear family

Abstract

We investigated the problem of constructing a near-field link budget to wirelessly communicate with high data rate (e.g. 3.125 Mbps) implantable circuitry located few centimeters under the skin using spread spectrum technique. Different methods and frequency bands were analyzed to choose the appropriate 2.4-GHz ISM band. The nominal power consumption of the implantable baseband communications circuitry was estimated for smaller technology nodes using the Synopsys CAD tools. The effect of using the ultra low power subthreshold operation in different technology nodes was also analyzed using predictive technology models. By introducing an analysis flow and the corresponding implementation code, we were also able to predict the subthreshold power consumption of the circuitry in different technology nodes and importantly at the gate level.

Acknowledgment

I would like to express my honest appreciation to my M.Sc. supervisors, Professor Christian Schlegel and Professor Bruce F. Cockburn, for their continuous support and encouragement.

I would also like to offer my special thanks to Dr. Deyasini Majumdar for her generous support and help during my graduate studies.

I would like to thank Alberta Innovates for Health Solutions (AIHS) and the Project SMART group for their continued support, both financially and academically.

Last but not least, I would like to thank my beloved parents who devoted the best days of their lives to my growth and success. I truly appreciate their love and kindness.

Contents

List of Tables

List of Figures

List of Abbreviations

AM	Amplitude Modulation
ASK	Amplitude-Shift Keying
AWGN	Additive White Gaussian Noise
BFSK	Binary Frequency-Shift Keying
BPSK	Binary Phase-Shift Keying
DBPSK	Differential Binary Phase-Shift Keying
DC	Direct Current
DFSK	Differential Frequency Shift Keying
DSSS	Direct-Sequence Spread Spectrum
EIRP	Equivalent Isotropically Radiated Power
EMF	Electromotive Force
ESR	Equivalent Series Resistance
FCC	Federal Communications Commission
FDTD	Finite-Difference Time-Domain
FSK	Frequency-Shift Keying
GFSK	Gaussian Frequency-Shift Keying
HF	High Frequency
ISM	Industrial, Scientific and Medical
ISMS	Intra-Spinal Micro-Stimulation
LSK	Load-Shift Keying
MICS	Medical Implant Communication Service
NFC	Near-Field Communications
OOK	On-Off Keying
PCB	Printed Circuit Board
PISO	Parallel-In Serial-Out
PSD	Power Spectral Density
PTM	Predictive Technology Model
RF	Radio Frequency
Rx	Receiver
SAR	Specific Absorption Rate
SMART	Sensory Motor Adaptive Rehabilitation Technology
SNR	Signal-to-Noise Ratio
Tx	Transmitter
UHF	Ultra-High Frequency
ULP	Ultra-Low Power
UWB	Ultra-Wideband
VHF	Very-High Frequency

Chapter 1

Introduction

This thesis project is a part of a larger research effort, called Project SMART (Sensory Motor Adaptive Rehabilitation Technology) [1]. The ultimate goal of the group is to develop revolutionary neural interfaces to recover motor and sensory abilities after neural injuries and diseases. Neural interfaces are defined as devices that record from and stimulate the nervous system to regain lost functions.

Neural injuries and diseases affect individuals for the rest of their entire life because the neural axons in the central nervous system (including the brain and spinal cord) do not have the ability to regenerate. Recent estimates show that one in three Canadians of all ages will be affected by a disease, disorder, or injury of the brain or nervous system. Based on Health Canada data, the economical burden of neural pathologies is conservatively estimated to be $22.7 billion annually [2].

Our research subgroup, called the Embedded Recording Focus Group, is working towards the design and implementation of an implantable wireless neural recording device. The device is intended to record neural activities from the dorsal root ganglia in the spinal cord and then wirelessly transmit the signals to an external control system. The data obtained from the neural recorder is to be processed to provide feedback in a closed-loop intra-spinal micro-stimulation (ISMS) system, where the neural signals are used to obtain sensory information and predict limb position to modulate the ISMS pattern to produce controlled walking in real-time. This wireless neural recording system could be used for other neural recording purposes as well and even with some modifications can be ready for brain-computer interface.

As a member of the communications section of the subgroup, the author has worked on various research topics based on requirements of an implantable wireless transmitter. Among the project requirements, the communications method was considered first. As the main contribution, the link budgets for the uplink and downlink are analyzed to understand how much transmit power is needed to achieve a required data rate. Assuming that power should be transferred over an inductive downlink, the power consumption of the implantable wireless transmitter is estimated. Another analysis is that how much we can save in terms of circuitry power consumption by using smaller technology nodes and subthreshold regime.

The neural recording implant is assumed to be located a few centimeters under the skin and in muscle tissue close to the spinal cord. Therefore, the communications method should accommodate a few centimeters of biological tissue in the transmission path. We have freedom in choosing the location of the external receiver/transmitter and it can even be put close to skin. As the neural signals are inherently high data rate, we require the implantable transmitter to be able to transmit a few Mbps of data. According to the estimates with 16 channels of recording, around 3 Mbps transmission capability should be enough. The communications system should not be detuned much due to surrounding biological tissues. The communications method chosen should give enough protection against interference and should also give the ability to add extra implantable sensors in the case needed. As an implantable device, the form factor becomes important as well.

The rest of the thesis is organized as follows: A literature review on the research topics and some preliminary information is included in Chapter 2. A link budget analysis is presented in Chapter 3. The power consumption estimation of the wireless transmitter circuitry is included in Chapter 4. Chapter 5 summarizes the conclusions of the research and proposes directions for possible future work.

Chapter 2

Literature Review

2.1 Current Implantable Communications Systems

In this section, we consider the various options for communicating with an implant system. Section 2.1.1 reviews near-field communications methods, which have two main scenarios: one uses inductive powering only and the other uses inductive powering and telemetry. Section 2.1.2 analyzes far-field communications and reviews and compares the projects done in this field.

Based on electromagnetic wave characteristics from a transmitter antenna, the space surrounding the antenna is usually categorized in two regions of near-field and far-field [3]. Added to the propagation terms in the far-field distance from the antenna, there are some evanescent terms that fade out at a certain distance from the antenna. The electromagnetic waves in the near-field are therefore sometimes called quasi-static [4]. In vacuum, the electromagnetic waves from the antenna in the far-field are essentially transverse electromagnetic (TEM) and the angular distribution of the field is not dependent on the separation, however this may not be the case in the near-field and fields in the direction of the propagation may exist with an angular distribution that varies with distance. The near-field can be separated into two sections of reactive near-field and radiating near-field (Fresnel) with an approximate separation of $R < 0.62\sqrt{D^3/\lambda}$ and $0.62\sqrt{D^3/\lambda} \leq R < 2D^2/\lambda$, respectively. The far-field is then located in around $R \geq 2D^2/\lambda$. The parameters λ,

D and R in the inequalities are wavelength, largest dimension of the antenna and distance from antenna, respectively. Note that, D must be large compared to the wavelength for the inequalities to be valid [3].

2.1.1 Near-field Communications

Power and data can be transfered to an implant jointly via inductive coupling. There are two major factors to consider regarding inductive links. One is the amount of coupling between the magnetic coils at the transmitter and receiver, and the other is the heat dissipation in nearby tissues due to inductive heating.

Recall that, the near-field region can be categorized into the reactive near-field and radiative near-field. Inductive coupling is strong in the reactive near-field region of the transmitter coil. Typically, the reactive near-field extends out to a distance of $R_1 = 0.62\sqrt{D^3/\lambda}$ from the antenna. The radiative near-field begins at a distance of $R_1 = 0.62\sqrt{D^3/\lambda}$ to $R_2 = 2D^2/\lambda$ from the antenna [3]. For example, if a dipole antenna operates at $f = 2.4$ GHz and has the length of D =1 cm, then $R_1 \approx 1.75$ cm and $R_2 \approx 16$ cm. Accordingly, inductive links are suitable for short range power and data transfer.

The downlink (towards implant) can be used for inductive power transfer or joint power transfer and data telemetry. Note that the uplink (leaving body) is usually of greatest interest for data telemetry. In the next subsections, projects addressing these two attributes will be introduced. Data transfer can even be accomplished through the same coupled loop antennas for inductive powering.

Inductive Power Transfer

Electronic biomedical implants need a source of electrical energy to operate. Traditionally, the electric energy is supplied by batteries. However, limited battery life imposes relatively high risk and further costs to this solution, including the need to replace expended implanted batteries with surgery.

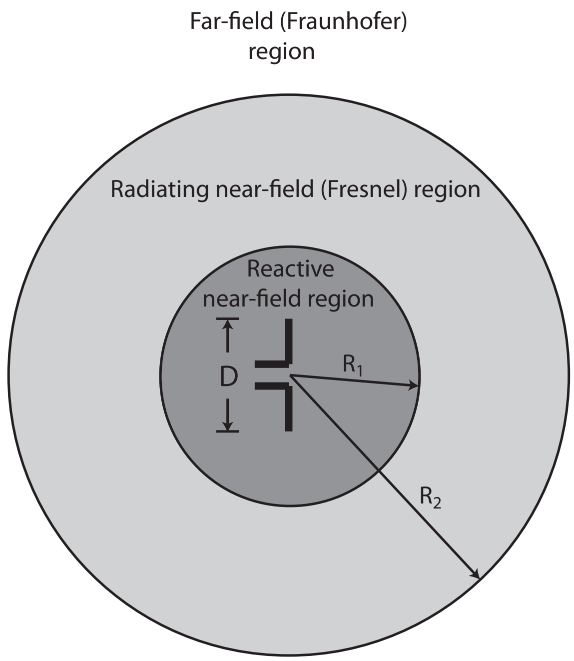

$$R_1 = 0.62\sqrt{D^3/\lambda}$$
$$R_2 = 2\,D^2/\lambda$$

Figure 2.1: Field regions of an antenna [3].

Battery systems can also be charged via wireless power transfer. One practical way to do this is to make use of inductive links. The power transfer is basically achieved by using two magnetic coils serving as external transmitter and implanted receiver. Figure 2.2 demonstrates this concept.

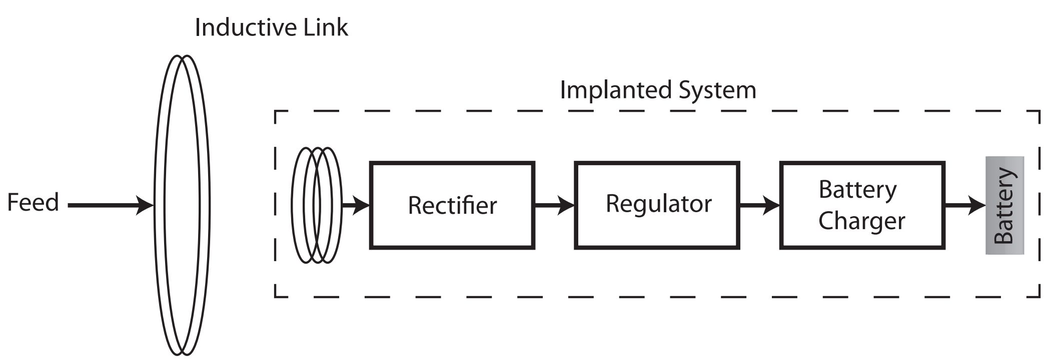

Figure 2.2: Inductive link concept [5].

Table 2.1: Inductive Power Transfer

Project	f_c (MHz)	Distance (cm)	External coil diameter (cm)	Implant coil diameter(cm)	Application
Lee2010a [6]	13.56	7–12	16.8	3.0	Brain Neural Recording
Song2007a [7]	13.56		1	1	Brain Neural Recording
Kiani2010a [8]	13.56	$\sim$1	2	1	Generic (No Implantation)
Kim2007a [9]	2.64	$<$1.2	$\geq$ 0.5	0.5	Generic (No Implantation)
RamRakhyani2011 [10]	0.7	1.0–2.0	$\leq$ 8	2.2	Generic (No Implantation)

The inductive coupling is described by Faraday's Law:

$$\oint \vec{E} \cdot \vec{dl} = -\frac{\partial \Phi_B}{\partial t} \tag{2.1}$$

where $\vec{E}$ is the electric field induced along an element $\vec{dl}$ of one loop of the coil, and Φ_B is the magnetic flux enclosed by the coil.

Let's assume that two coils are in each other's vicinity and current, i_1, is flowing in the first coil. If the current changes, a variable magnetic flux happens which leads to a total electromotive force (EMF) in the second coil [4].

$$v_2(t) = -n_2 \frac{\partial \Phi_B(t)}{\partial t} \tag{2.2}$$

where $v_2(t) = \oint \vec{E_2(t)} \cdot \vec{dl_2}$ and n_2 is the number of windings of the second coil.

Inductive coupling has been used in several projects to achieve magnetic power transfer. Table 2.1 compares some of their main specifications.

Joint Inductive Power Transfer and Data Telemetry

In another scenario, inductive link is used for transferring both data and energy. Before comparing these projects, we need to define some terminology. By downlink and uplink we mean the wireless connection towards the implant and external circuitry, respectively. Over the downlink, power signals, command signals or both kinds of signals can be transmitted. Over the uplink, data signals are transmitted. Table 2.2 compares recent projects that use both energy transfer and data telemetry. The energy transfer in all the projects of the chart is accomplished via inductive coil-to-coil links. However, the uplink data telemetry is done either by RF links or inductive links. A change in load can affect the transmitter in the near-field region. Based on this phenomenon, Load Shift Keying (LSK) modulation can be used to transmit data back through the same coil system that delivers power. The projects in this table do not meet our minimum requirements for data rates.

2.1.2 Far-field Communications

The far-field region of the antenna starts at a radial distance of approximately $R_2 = 2D^2/\lambda$ from the antenna, where D is the largest dimension of the antenna and λ is the wavelength. In the far-field region, the angular distribution of the electromagnetic field is essentially independent of the distance from antenna. Moreover, the field components are transverse in this region. These field properties make the analytical solutions much easier. In fact, closed-form solutions are reachable in simpler cases [3].

To model transmission in the far-field region, we can use the *Friis Transmission Equation* [3]. By means of this equation, the received power is computable in free space. This equation is the basis for link budget analysis. For reflection and polarization-matched antennas, which are aligned for maximum radiation and reception, the Friis Equation simplifies to [3]:

$$\frac{P_r}{P_t} = \left(\frac{\lambda}{4\pi R}\right)^2 G_{0t} G_{0r} \tag{2.3}$$

where P_t is the input power at the terminals of the transmitting antenna, P_r is the power delivered to the receiver load, G_{0t} is the maximum transmitter antenna gain, G_{0t} is the maximum receiver antenna gain, R is the distance between two antennas, and λ is the wavelength of the signal.

Table 2.3 compares the projects done in far-field category of implantable communications. The comparison is based on two main specifications for our work, which are power consumption and data rate. These projects in this table are the most relevant implantable systems that we are aware of. Some of these projects lack the

Table 2.2: Inductive Power Transfer and Data Telemetry

Project	Link type	Frequency (MHz) data / power	Data Rate (Mbps)	Modulation	External coil diameter (cm)	Implant coil diameter (cm)	Separation Distance (cm)	Application
Ghovanloo2004 [11]	Downlink (Inductive)	5/10 (pc*)	2.5	DFSK	0.2–0.3	1.2	0.5	Generic
	Uplink (NA)	–	–	–	–	–	–	(No Implantation)
Sodagar2009a [12]	Downlink (Inductive)	4/8	2	FSK		< 1 cm	~ 0.1 (Skin)	Neural Recording
	Uplink (RF)	70–200	2	OOK				
Harrison2007 [13]	Downlink (Inductive)	2.64 (pc)	0.0065	ASK	-	0.05	2	Neural Recording
	Uplink (RF)	433 (data)	0.330	FSK	NA	NA		(Tx** Not Implanted)
Harrison2009a [14]	Downlink (Inductive)	2.765 (pc)	-	ASK	5.8	0.5	3	Neural Recording
	Uplink (RF)	902/928 (data)		FSK	NA	NA	5	(Tx Not Implanted)
Mollazadeh2009 [15]	Downlink (Inductive)	4	NA	NA	5	2	3.5	Neural Recording
	Uplink (Inductive)	4	<0.032	LSK	same coil	same coil	3.5	(Tx Not Implanted)
Catrysse2004 [16]	Downlink (Inductive)	0.7	<0.06	AM	6	2	3	Generic
	Uplink (Inductive)	0.7	<0.06	LSK	same coil	same coil	3	(Tx Not Implanted)

* 'p' stands for power, 'c' stands for command, and 'pc' stands for joint power and command
** Tx stands for transmitter

minimum data rate required, such as in [17, 18, 19]. Some other projects are not implanted well in tissue (a few cm) and have also not well considered the deterioration due to other transmitters in the same congested 2.4-GHz ISM band; therefore, the data rates are expected to drop significantly due to the extra path loss and interference (Projects [20, 21, 22]). Some projects also need to discuss the detuning effects of surrounding tissues on the electric antennas used such as in [20, 22].

2.2 Antenna Designs and Their Compatibility with Implantation

In the antenna circuit model, the radiation resistance is the resistance that models the amount of radiated power radiated by the antenna. The loss at the antenna is modeled by a loss resistance, and the reactivity of the antenna is modeled by a reactance parameter. Using the antenna model parameters, we can calculate the antenna radiation efficiency as follows [3]:

$$e_{cd} = \frac{R_r}{R_L + R_r} \tag{2.4}$$

where R_r is the radiation resistance and R_L is the loss resistance.

Based on the antenna design, the radiation resistance has been improved. The gain of antenna is given by $G = \eta D$, where η is the antenna efficiency and D is the directivity. The efficiency in this formula includes impedance matching. As the radiation efficiency increases, more radiation is emitted from the transmitter antenna and more antenna gain is resulted.

If the radiation resistance of an antenna is very small, it cannot be efficiently used for radiation. Therefore the transmission range is limited. Loop antenna designs are usually split into two categories: electrically small antennas ($C < \lambda/10$) and electrically relatively large antennas ($C \sim \lambda$), where C is the loop circumference. The electrically small antennas are poor radiators, which means that their radiation

Table 2.3: Implantable Communications Systems using the Far-field Region.

Project	Purpose	f_c (GHz)	Stage	Data Rate (Mbps)	Tx Power Cons. (mW)	Mod.
Contaldo2010 [17]	Body Area Networks (Not Implanted)	2.4	bench-top	1	47.3	GFSK
Zhang2011 [20]	Body Area Networks (Not Implanted)	2.4	bench-top	4	4.86	OOK
Kahn2010 [21]	Generic (Implanted under Skin)	2.4	in vivo	8	1.05	BFSK
Anis2010 [18]	Generic (Not Implanted)	0.402-0.405 (MICS)	bench-top	Tx=0.5 Rx=0.12	Tx=0.3 Rx=0.5	OOK (UWB)
Bradley2006 [19]	Generic (Not Implanted)	0.402-0.405 (MICS)	bench-top	0.8	17.5	FSK
Jung2010 [22]	Generic (Not Implanted - Skin-Mimic Depth)	2.46 (ISM)	in vitro	136	3	OOK

resistance is very small. They are more typically used in the receive mode rather than the transmission mode [3].

Although loop antennas with very small radiation resistance cannot be efficiently used for radiation, they may have relatively strong near-fields and can be used well for the coupled transmission case. However, we should know that as the near-field is limited to a short range from the antenna ($R < 2D^2/\lambda$), the coupling between loop antennas is limited in range.

The circumference of the receive antenna used in the simulations in [23] is approximately 0.5 cm, which is less than $\lambda/10$ at 2.45 GHz ($\lambda = 12.245$ cm). Therefore, the receive loop antenna can be categorized as an electrically small loop antenna. Although, we can transmit signals on the uplink using this antenna, the efficiency is limited due to its size. The radiation resistance of a small loop antenna can be increased by increasing its total circumference, which is done simply by increasing the turns. Another way would be to use a high permeability ferrite core, which will increase the magnetic field intensity and thus the radiation resistance.

One potential concern with using loop antennas is the amount of specific absorption rate (SAR) that they produce in biological tissues. This can be overcome by operating the loop antennas at optimal frequencies, as suggested in [23]. Additionally, a new design for mm-size loop antennas has been proposed in [24], which includes segmentation of the loop antenna. Using this design, the SAR produced by the power link reduced by 30% and also 10% link loss reduction achieved. This result increases the power available by about 43% compared to the conventional loop antenna.

2.2.1 Loop Antennas for Data Communications

In contrast with other electric antennas, such as the dipole and patch, loop antennas are magnetic antennas. Magnetic antennas are less detuned compared to electric antennas by the dielectric properties of the surrounding materials in the reactive near field. This is the reason why loop antennas are often used in hand-held and body-worn applications [25].

Added to this advantage, the loop antenna structures are usually preferred because of functionality. One functional advantage is that solenoidal current sources produce a weaker electric near-field, which causes less tissue loss [23]. The other reason is that loop antennas demonstrate good magnetic coupling [24].

Loop antennas can be used in two different scenarios to transmit signals: one is coupled transmission and the other is radiative transmission.

In the coupled transmission scenario, the receiver is usually another loop antenna as well. The coupling occurs in the near-field and therefore the transmission range is limited to this region. Examples of this kind of transmission are a simple transformer and the near-field communication (NFC) system available in recent mobile handsets [26]. In the coupling case, transmitter radiation resistance is so small that not much radiation occurs and the antenna simply works as an inductor with high near-field magnetic intensity, which decays significantly with distance.

In the radiative case, the radiation resistance of the loop antenna, which is proportional to antenna efficiency, is an important characteristic. In this application, the loop antenna is used like any other antenna for far-field purposes and is analyzed similarly. As noted earlier, antennas can be categorized into two groups: small and large. If the loop circumference is smaller than one-tenth of free space wavelength, the loop is considered small and if it is in the order of the free-space wavelength, the loop is considered large. Small loops usually have a smaller radiation resistance compared to large loops. Therefore small loops are usually used in receive mode in radio communications. The loop antennas are mostly operated in the HF (3-30 MHZ), VHF (30-300 MHz), and UHF (300-3000 MHz) bands [3].

It is possible to have power transfer over the same communications link. Several designs using loop antennas, for both energy transfer and also data communications have been reported in the literature [15, 27, 16]. However, using the same coil-to-coil link for both uplink and downlink data transmission has not yet been applied to high data rates. In [15], 32 kbps with a 4 MHz carrier frequency for the uplink was achieved. The maximum data rate achieved in [16] is a bit higher with 60 kbps at a 700 kHz carrier frequency. The carrier frequencies used in the literature are, however, for smaller frequencies. As discussed, the optimal frequency for biological implants falls in the low-GHz range and as the efficiency of the loop antenna is higher at larger frequencies and the radiation resistance is larger, we expect an increase in the achievable data rate as well.

Sample Antenna Design for Radiative RF Communications

The formulas derived based on assumption of small loop and constant current can be used as a starting point for radiative loop antenna design. Under the constant current assumption, the loop can be considered as a radiating inductor with inductance L and radiation resistance R_r. Adding an appropriate capacitance C, produces a resonant circuit. Also a resistance R_{att} is often added in parallel to the capacitor to reduce the quality factor and therefore reduce the sensitivity to tolerances. The model of the loop antenna is illustrated in Fig. 2.3.

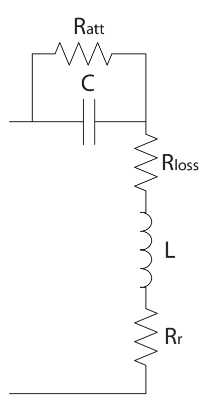

Figure 2.3: Loop antenna model with radiation resistance (R_r), capacitance (C), loss resistance (R_{loss}), inductance (L), and attenuation resistance (R_{att}) [25].

The model parameters are calculated using the following equations [25]:

$$R_{loss} = \frac{U}{2w}\sqrt{\frac{\pi f \mu_0}{\sigma}} + R_{ESR} \tag{2.5a}$$

$$L = \mu_0 a \left(\ln\left(\frac{a}{b}\right) + 0.079\right) \text{ (Circular loop)} \tag{2.5b}$$

$$L = \frac{2\mu_0}{\pi} a \left(\ln\left(\frac{a}{b}\right) - 0.774\right) \text{ (Square loop)} \tag{2.5c}$$

$$R_r = \frac{A^2}{\lambda^4} \times 31.171 \times 10^3 \ \Omega \tag{2.5d}$$

where the formulas are valid for a circular loop antenna with radius a, a square loop antenna with the side length a, or for a rectangular antenna with an equivalent square side length of $a = \sqrt{a_1 a_2}$, where a_1 and a_2 are the side lengths of the rectangular loop. The circumference of the loop is shown by U, the wire radius is called b and the equivalent b parameter for loop antenna realized with PCB trace is $b = 0.35d + 0.24w$, where d is the thickness of the copper layer and w is the trace width. The equivalent series resistance R_{ESR} accounts for the losses in the capacitor. A is the area of the loop antenna.

The maximum quality factor is calculated from the following formula [25]:

$$Q = \frac{1}{\sqrt{1 + \Delta C/C} - 1} \tag{2.6}$$

where $\Delta C/C$ is the capacitance tolerance.

Recall that the loop is modeled with an inductance, and so we will have [25]:

$$R_{att\_trans} = \frac{2\pi f L}{Q} - R_r - R_{loss} \tag{2.7}$$

where R_{att_trans} is the transformed attenuation resistance from parallel to series.

The radiative efficiency of the antenna can then be calculated as follows [3]:

$$\eta = \frac{R_r}{R_r + R_{loss} + R_{att\_trans}} \tag{2.8}$$

Using Eq. 2.7, the radiative efficiency can be calculated as [25]:

$$\eta = \frac{QR_r}{2\pi f L} \tag{2.9}$$

To compare the radiative efficiency of small loop antennas at different frequencies, consider Fig. 2.4 which plots the radiative efficiency of small loop antennas versus their diameter. In this figure, the capacitance tolerance is 5%, the PCB trace width is 1 mm, and the copper thickness is 5 μm. According to this plot, we can expect even higher efficiencies for the loop working in the 2.4-GHz ISM band, but Eq. 2.9 does not accurately define the behavior at 2.4-GHz and the efficiency value exceeds the 0 dB for larger diameter sizes. This is because for larger diameter sizes, the small loop antenna assumption is violated and as the radiation resistance formula is calculated assuming small loop antenna, the formula is not valid anymore.

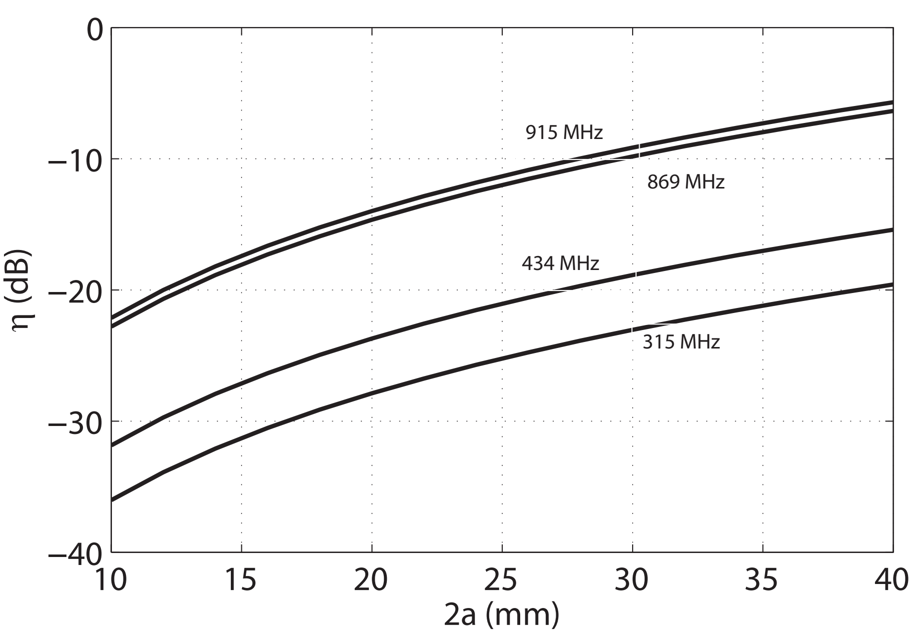

Figure 2.4: Radiative efficiency of a small circular loop antenna [25].

In order to match a loop antenna to a 50 Ω feed, the loop antenna is usually tapped as shown in Fig. 2.5. A series feed, as shown in the figure, gives a relatively small impedance and a parallel feed gives a large impedance. A tap gives an adjustable impedance between these two and by deciding the correct place for tap, it gives 50 Ω.

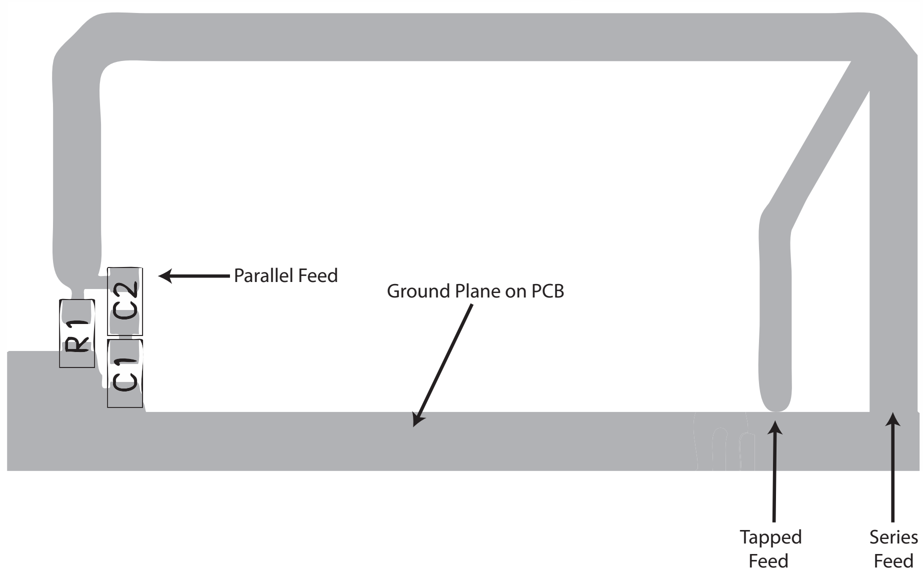

Figure 2.5: Example of a tapped PCB loop antenna [25].

As an example, to derive the antenna parameters for the first round of antenna design, we can first assume a loop antenna realized with PCB traces as in Fig. 2.5. The loop width is assumed to be 25 mm, the height 11.5 mm, the trace width 1.5 mm, and the copper thickness 50 μm. As in Eq. 2.5, the antenna's inductance only depends on the physical shape of the antenna and it is calculated to be $L = 40.9$ nH. The radiation resistance depends on the wavelength in combination with the physical shape and here it is $R_r = 10.6\ \Omega$. The calculated capacitance for resonance at 2.4 GHz is 4.24 pF. Assuming a total capacitance tolerance of 20% including the capacitance itself, the PCB pads, the damping resistor, and even the solder materials, the maximum quality factor achievable is $Q = 10.5$. The impedance of the loop inductance can be calculated to be $Z_L = 2\pi \times 2.4$ GHz $\times 40.9$ nH $= 616.8\ \Omega$. Using an attenuation resistor of R_{att} =2.2 kΩ in parallel with the capacitor, the transformed series resistance is then $R_{att\_trans} = Z_L/Q = 616.8/10.5 = 58.74\ \Omega$. Using these values and assuming that loss resistance is negligible, the radiative efficiency is given as:

$$\eta = \frac{10.6}{10.6 + 58.74} = 152.87 \times 10^{-3} = -8.2 \text{ dB} \tag{2.10}$$

It should be emphasized that these values are the basis only for a first round of design and they should be further tuned following electromagnetic simulations to calculate the exact values.

2.2.2 Comparison with Other Antenna Types

The microstrip antennas (patch antennas) demonstrate some benefits in many on-board applications, however their suitability for biomedical applications should be further examined.

Microstrip antennas have a low-profile, are conformal to planar and non-planar surfaces, are simple and inexpensive to manufacture using PCB technology, and are mechanically robust [3].

On the other hand, microstrip antennas have certain drawbacks. Since they are electric antennas, they are easily detuned in implanted applications with dielectric tissues surrounding it. They have relatively low efficiency and have a high quality factor, sometimes in excess of 100. They have poor polarization purity, spurious feed radiation, and also a narrow bandwidth because of their high quality factor [3, 25]. There are some methods to improve their efficiency, including increasing the height of the substrate, but this approach leads to more surface wave losses [3, 25]. It has also be shown that in the presence of surrounding muscle tissue, a patch antenna which had a resonance frequency of 2.45 GHz in air, completely loses its resonance at that frequency. Only with thick layer of insulation it starts to regain significant resonance at 2.45 GHz. [28]

According to [28] (Chapter 5), as a rule of thumb the most power-efficient small antenna in lossy material is a dipole (magnetic or electric) with as thick an insulation as possible. Magnetic dipole antennas (loop antennas) are more efficient than electric dipole antennas.

A comparison of some of the short range antennas is included in Table 2.4.

Table 2.4: Comparison of Short Range Antennas [25].

Antenna Type	**Applications and Interest**	**Efficiency**	**Sensitivity to Detuning**
Loaded stub	Small PCB and wire antennas	Moderate	High
Helical antenna (transversal)	Small wire antennas	Moderate	High
Dipole	Large wire antenna; balanced feed	High	Moderate
Monopole	Large wire antenna; single-ended feed	High	Moderate
Small loop	Body-worn antennas	Low	Low

2.3 Options for Powering Implants

Several methods to power biomedical implants have been investigated, including batteries, thermoelectric, and electromagnetic energy transfer. While batteries have high energy density, they need some sort of encapsulation, which makes them rather big for mm-size implants. They also need regular maintenance and replacement, which may require surgery. On the other hand, my understanding is that energy harvesting methods currently lack high power densities, but would have the potential to evolve and have higher power densities in the future. Analyzing the current proven technologies, power transfer using electromagnetic waves has been demonstrated to produce the highest power density among the alternative methods investigated [29]. A comparison of achievable power densities using different methods of powering is shown in Table 2.5.

In the electromagnetic energy transfer case, the power density is calculated using Poynting's theorem which governs the amount of electromagnetic power flux through space [4]. Recall that Poynting's vector is $\boldsymbol{S} = \boldsymbol{E} \times \boldsymbol{H}$, where the units of the electric field intensity ($\boldsymbol{E}$) and the magnetic field intensity ($\boldsymbol{H}$) are V/m and A/m, respectively.

In addition to the high power density of electromagnetic energy transfer, a further advantage is a reduction in the need for future surgeries compared to battery-powered implants. One main drawback of using electromagnetic energy transfer

Table 2.5: Achievable Power Densities using Different Implant Powering Methods [29].

Methods and Parameters	**Power Density**
Primary batteries [30]	0.09 $\mu W/mm^2/year$
Glucose bio-fuel cell, utilizing blood glucose (5 mM) [31]	2.8 $\mu W/mm^2$
Thermoelectric, ΔT = 5°C [32]	0.6 $\mu W/mm^2$
Pizoelectric microbender, f $\approx$ 800 Hz, 2.25 m/s^2 [33]	< 0.2 $\mu W/mm^3$
Electromagnetic energy transfer	10 to 1000 $\mu W/mm^2$

has been antenna size, which is usually much larger than the associated electronics. However, it has been recently shown that higher frequencies in the order of GHz are equally well-suited for electromagnetic energy transfer in biological tissue. This leads to a 100-fold smaller receiving antennas without sacrificing energy transfer efficiency or range [34].

Due to the advantages of the electromagnetic energy transfer compared to competitor technologies, we discuss this technology in more detail in the sequel.

2.4 Reason for Low-GHz Frequency Optimality

The low-frequency model of the relative permittivity used in the literature to model the electrical properties of biological tissue is as $\epsilon_r = \epsilon_{r0} + i\frac{\sigma}{\omega\epsilon_0}$. Using the definition $k^2 = \omega^2\mu\epsilon$ under the assumption of $\mu_r = 1$ for biological tissues as in [23], the wavenumber is approximately given by

$$k = \sqrt{\frac{\omega\mu_0\sigma}{2}}(1+i) \tag{2.11}$$

The factor ikz is the complex exponent in the wave equations, where the real part of k gives the propagation frequency and the imaginary part gives the attenuation with distance. Using the real part of the k, the wavelength is calculated as $\lambda = 2\pi/\text{Re}(k)$. According to [35], the absorption coefficient is defined as:

$$\alpha = 2\kappa \tag{2.12}$$

where κ is the imaginary part of the wavenumber ($\mathrm{Im}(k)$).

The absorption coefficient at low-frequencies is given as

$$\alpha = \sqrt{2\omega\mu_0\sigma} \propto \sqrt{\omega} \tag{2.13}$$

According to Eq. 2.13, the absorption coefficient increases with $\sqrt{\omega}$ in the low-frequency domain, which may lead to the erroneous conclusion that higher frequencies are not suitable for electromagnetic energy transfer. However, using the Debye relaxation model for biological tissues [36] the relative permittivity is modeled as

$$\epsilon_r(\omega) = \epsilon_\infty + \frac{\epsilon_{r0} - \epsilon_\infty}{1 - i\omega\tau} + i\frac{\sigma}{\omega\epsilon_0} \tag{2.14}$$

where ϵ_{r0} is the static relative permittivity, σ is the conductivity, τ is the relaxation time constant, and ϵ_∞ is the relative permittivity at frequencies where $\omega\tau \gg 1$.

The relaxation model is valid over the frequency range of $\omega\tau \ll 1$, where the relative permittivity can be approximated as

$$\epsilon_r(\omega) \approx \epsilon_{r0} + i\left(\frac{\sigma}{\omega\epsilon_0} + \omega\tau\Delta\epsilon\right) \tag{2.15}$$

where $\Delta\epsilon = \epsilon_{r0} - \epsilon_\infty$.

Based on Eq. 2.15, the wavenumber can be approximated as

$$k \approx \omega\sqrt{\mu_0\epsilon_0\epsilon_{r0}} + i\frac{\omega}{2}\sqrt{\frac{\mu_0\epsilon_0}{\epsilon_{r0}}}\left(\frac{\sigma}{\omega\epsilon_0} + \omega\tau\Delta\epsilon\right) \tag{2.16}$$

Using the imaginary part of the wavenumber, the absorption coefficient is calculated as

$$\alpha = (\sigma + \omega^2\tau\epsilon_0\Delta\epsilon)\sqrt{\frac{\mu_0}{\epsilon_0\epsilon_{r0}}} \tag{2.17}$$

Over a large range, the absorption coefficient is constant with frequency for $\omega \ll \sqrt{\sigma/\tau\epsilon_0\Delta\epsilon}$ (low frequencies) and then grows with the square of ω when $\omega \gg$

$\sqrt{\sigma/\tau\epsilon_0\Delta\epsilon}$ (high frequencies).

As the tissue absorption increases with frequency, it was conventionally believed that lower frequencies in the order of MHz would produce better transfer efficiency. Omitting the displacement current ($j\omega\epsilon\vec{E}$) in Maxwell equations, due to the low frequency, leads to the result that the diffusion length becomes inversely proportional to the square of frequency and this confirms that higher frequency decays faster in tissue. However, the mentioned diffusion approximation is valid for good conductors and tissue is better modeled as a low-loss dielectric with significant displacement current. Solving the Helmholtz equation shows that the penetration depth is asymptotically independent of frequency. On the other hand, the received power is proportional to the frequency of the incident magnetic field and this leads to the conclusion that higher frequency results in higher efficiency. As discussed earlier, the Debye model for tissue leads to higher absorption coefficient in higher frequencies, which leads to a possible optimal frequency for energy transfer [23].

2.5 High-Frequency Electromagnetic Energy Transfer

Power transfer using low-frequency electromagnetic waves as carriers in conjunction with inductive coupling has been common practice for a long time. In the past fifty years, the focus has been on frequencies of less than 10 MHz for energy transfer purposes. On the other hand, higher frequencies on the order of 10 MHz to a few GHz have been used for implant telemetry systems. In thermotherapy, in which electromagnetic energy is used to heat up a specific part of body, both low-frequency ($<$ 10 MHz) and high-frequency ($>$ 1 GHz) carriers have been used. With this wide selection of carrier frequencies, the question arises if there is an optimal carrier frequency, which maximizes the received power. It has been shown in [23] that the optimal frequency for energy transfer in biomedical tissues using electromagnetic waves in case of small receiver dimension compared to implantation depth is in the range of sub-GHz to low-GHz.

2.5.1 Energy Transfer in Homogeneous Tissue

Some assumptions have been made in the formulation of the energy transfer problem in [23] and [37]. First, a current source is considered at the transmitter in the equations. Since the separation of the transmitter and receiver is small, a full electromagnetic analysis was considered including details of the transmitter and receiver antennas. As a second assumption, only solenoidal current sources are considered because their electric near-field is smaller and this leads to less tissue loss. Since the receiver coil is assumed to be very small, we can model it with a magnetic dipole instead. Assuming the source to be in the center of the coordinates, the skin interface is located in $-d_1$ location and the receive dipole is located in $-d$ location.

Maxwell's equations can be manipulated to become symmetrical by introducing a magnetic current density ($\boldsymbol{M}$) as the dual of the electric current density ($\boldsymbol{J}$) and a magnetic charge density (ρ_m) as the dual of the electric charge density (ρ) [38]. Using these concepts, Maxwell's equations can be written as

$$\nabla \times \boldsymbol{E} = -\frac{\partial \boldsymbol{B}}{\partial t} - \boldsymbol{M} \tag{2.18a}$$

$$\nabla \times \boldsymbol{H} = \frac{\partial \boldsymbol{D}}{\partial t} + \boldsymbol{J} \tag{2.18b}$$

$$\nabla \cdot \boldsymbol{B} = \rho_m \tag{2.18c}$$

$$\nabla \cdot \boldsymbol{D} = \rho \tag{2.18d}$$

Even though actual net nonzero magnetic currents do not exist physically, we can use equivalent magnetic currents to simplify some equations. For example, a small loop antenna can be modeled with a magnetic dipole [3]. Then, a series of electric current loops, shaped as a solenoid or a toroid, generate a field similar to the one generated by an equivalent fictitious magnetic current.

If we model the transmit and receive antennas as magnetic dipoles or a multitude of magnetic dipoles, in case of a larger loop, we can then rewrite Maxwell's equations under the assumption of non-zero magnetic current sources ($M \neq 0$) and zero electric current sources ($J = 0$) as shown in the following equations

$$\boldsymbol{\nabla} \times \boldsymbol{E} = i\omega\mu_0 \boldsymbol{H} - \boldsymbol{M_{tx}} - \boldsymbol{M_{rx}} \tag{2.19a}$$

$$\boldsymbol{\nabla} \times \boldsymbol{H} = -i\omega\epsilon \boldsymbol{E} \tag{2.19b}$$

where $\boldsymbol{M_{tx}}$ is the equivalent transmit magnetic current and $\boldsymbol{M_{rx}}$ is the equivalent receive magnetic current density due to the induced current in the receive loop antenna. In case of a very small loop antenna, the antenna can be modeled with a magnetic dipole [3]. In case of a larger loop antenna, it can be modeled as an array of infinitesimal current loops which have an equivalent nonzero magnetic current density [39].

The complex Poynting vector is written as $\boldsymbol{E} \times \boldsymbol{H}^*$, which has a unit of $watts/m^2$ as in power density. Substituting Eq. 2.19 in Poynting's theorem and after some algebraic manipulations we can obtain

$$\nabla \cdot (\boldsymbol{E} \times \boldsymbol{H}^*) = i\omega\mu_0 |\boldsymbol{H}|^2 - i\omega\epsilon^* |\boldsymbol{E}|^2 - \boldsymbol{H}^* \cdot \boldsymbol{M}_{tx} - \boldsymbol{H}^* \cdot \boldsymbol{M}_{rx} \tag{2.20}$$

By rearranging the terms, we achieve the following equation

$$-\boldsymbol{H}^* \cdot \boldsymbol{M}_{tx} = \nabla \cdot (\boldsymbol{E} \times \boldsymbol{H}^*) - i\omega\mu_0 |\boldsymbol{H}|^2 + i\omega\epsilon^* |\boldsymbol{E}|^2 + \boldsymbol{H}^* \cdot \boldsymbol{M}_{rx} \tag{2.21}$$

where the left side is the complex transmitted power density, $\nabla \cdot (\boldsymbol{E} \times \boldsymbol{H}^*)$ is the radiation power loss, the imaginary part of $\omega\epsilon^* |\boldsymbol{E}|^2$ is the sum of the dielectric loss and the induced-current loss, and $\boldsymbol{H}^* \cdot \boldsymbol{M}_{rx}$ is the complex received power density.

Using Poynting's theorem and the fact that the tissue layer is in the region $z < -d_1$ and the receive dipole is located at $z = -d$, we conclude that

$$P_{loss} = \frac{w}{2} \int_{z<-d_1} \mathrm{Im}\ \epsilon(\boldsymbol{r}) |\boldsymbol{E}(\boldsymbol{r})|^2 \, \mathrm{d}\boldsymbol{r} \tag{2.22a}$$

$$P_r = \mathrm{Re} \left\{ \frac{1}{2} \boldsymbol{H}^*(-\hat{\boldsymbol{z}} d) \cdot (-i\omega\mu_0 I_r A_r \hat{\boldsymbol{n}}) \right\} \tag{2.22b}$$

where I_r is the induced current on the receive loop and A_r is the area of the receive loop. Note that $-i\omega\mu_0 I_r A_r \hat{\boldsymbol{n}}$ is the equivalent magnetic dipole moment ($\boldsymbol{M_{rx}}$) of a small current loop with current I_r and area A_r. P_{loss} in Eq. 2.22a is the sum of the dielectric power loss and induced-current power loss.

One concern is the amount of the power absorbed by the biological tissue. The power transfer efficiency is defined in [23] as the ratio of the received power to the dissipated power, i.e.,

$$\eta \mathrel{\widehat{=}} \frac{P_r}{P_{loss}} \tag{2.23}$$

It is assumed that a fixed load is connected to the receive coil with impedance Z_L and it is also assumed that the effect of scattering fields by the receive coil's induced current is negligible in the calculation of the total fields. Using these assumptions and calculating both the resultant field vectors and the integral over the tissue depth,

$$\eta = \frac{|k|^2 A_r^2 \mathrm{Re}\ \frac{1}{Z_L}}{\omega\epsilon_0 \mathrm{Im}\ \epsilon_r} \frac{\boldsymbol{x}^\dagger \boldsymbol{h}\boldsymbol{h}^\dagger \boldsymbol{x}}{\boldsymbol{x}^\dagger \bar{\boldsymbol{K}} \boldsymbol{x}} \tag{2.24}$$

where the orientation of the transmit dipole is given by $\boldsymbol{x}$, the orientation of the receive dipole is given by $\boldsymbol{h}$, and the dielectric properties of the medium are captured by $\bar{\boldsymbol{K}}$. $\boldsymbol{x}$, $\boldsymbol{h}$, and matrix $\bar{\boldsymbol{K}}$ are as follows

$$\boldsymbol{x} = \begin{pmatrix} \alpha_{-1} \\ \alpha_0 \\ \alpha_1 \end{pmatrix} \tag{2.25}$$

$$\boldsymbol{h} = \begin{pmatrix} \boldsymbol{\psi}^*_{1,-1}(-\hat{\boldsymbol{z}}d).\hat{\boldsymbol{n}} \\ \boldsymbol{\psi}^*_{1,0}(-\hat{\boldsymbol{z}}d).\hat{\boldsymbol{n}} \\ \boldsymbol{\psi}^*_{1,1}(-\hat{\boldsymbol{z}}d).\hat{\boldsymbol{n}} \end{pmatrix} \tag{2.26}$$

$$\bar{\boldsymbol{K}} = \begin{pmatrix} \int_{z<-d_1} |\boldsymbol{\xi}_{1,-1}(\boldsymbol{r})|^2 \, \mathrm{d}\boldsymbol{r} & 0 & 0 \\ 0 & \int_{z<-d_1} |\boldsymbol{\xi}_{1,0}(\boldsymbol{r})|^2 \, \mathrm{d}\boldsymbol{r} & 0 \\ 0 & 0 & \int_{z<-d_1} |\boldsymbol{\xi}_{1,1}(\boldsymbol{r})|^2 \, \mathrm{d}\boldsymbol{r} \end{pmatrix} \quad (2.27)$$

where the direction of the transmit dipole is given by the unit vector of the Cartesian vector $((\alpha_{-1} - \alpha_1)/\sqrt{2}, (\alpha_{-1} + \alpha_1)/\sqrt{2}, \alpha_0)$ whose magnitude equals the transmit magnetic moment, and the dyadic Green's function for the wave equation resulted from Eq. 2.19 is decomposed into $\psi_{n,m}$ and $\xi_{n,m}$ multipoles [38].

Using the matrix representations of $\boldsymbol{x}$, $\boldsymbol{h}$, and $\bar{\boldsymbol{K}}$, the efficiency can be written as

$$\eta = \frac{|k|^2 A_r^2 \mathrm{Re}\ \frac{1}{Z_L}}{\omega\epsilon_0 \mathrm{Im}\ \epsilon_r} \cdot \frac{(|\alpha_{-1}|^2 + |\alpha_0|^2 + |\alpha_1|^2)(|\boldsymbol{\psi}^*_{1,-1}(-\hat{\boldsymbol{z}}d).\hat{\boldsymbol{n}}|^2 + |\boldsymbol{\psi}^*_{1,0}(-\hat{\boldsymbol{z}}d).\hat{\boldsymbol{n}}|^2 + |\boldsymbol{\psi}^*_{1,1}(-\hat{\boldsymbol{z}}d).\hat{\boldsymbol{n}}|^2)}{|\alpha_{-1}|^2 \int_{z<-d_1} |\boldsymbol{\xi}_{1,-1}(\boldsymbol{r})|^2 \, \mathrm{d}\boldsymbol{r} + |\alpha_0|^2 \int_{z<-d_1} |\boldsymbol{\xi}_{1,0}(\boldsymbol{r})|^2 \, \mathrm{d}\boldsymbol{r} + |\alpha_1|^2 \int_{z<-d_1} |\boldsymbol{\xi}_{1,1}(\boldsymbol{r})|^2 \, \mathrm{d}\boldsymbol{r}} \quad (2.28)$$

The key difference between the recent research and the previous erroneous conclusion of low frequency optimality is in the adoption of high-frequency dielectric models, i.e. Debye and Cole-Cole relaxation models instead of low frequency models. More information about how these models affect the conclusion is provided in Sec. 2.4.

If we use a low-frequency model for the relative permittivity ($\epsilon_r(\omega) = \epsilon_{r0} + i\frac{\sigma}{\omega\epsilon_0}$), the efficiency defined in Eq. 2.24 increases with frequency. However, this increase cannot continue forever and starting at a certain frequency, the change in dielectric polarization cannot follow the applied electric field and the time lag between the polarization and the electric field intensity starts to produce an energy loss [37, 40]. The dielectric polarization at lower frequencies and in isotropic and linear dielectric media is directly proportional to the electric field through the equation $\boldsymbol{P} = \epsilon_0 \chi_e \boldsymbol{E}$, where χ_e is a dimensionless quantity called electric susceptibility [4]. The Debye relaxation model describes this phenomenon. This dielectric relaxation loss results in a decrease of the efficiency and it is because the imaginary part of the relative permittivity in Eq. 2.15, which is in the denominator of the efficiency as in Eq. 2.24, has an extra added $\omega\tau\Delta\epsilon$ term compared to the low frequency model of relative permittivity ($\epsilon_r = \epsilon_{r0} + i\frac{\sigma}{\omega\epsilon_0}$). Therefore, an optimal frequency is expected to emerge.

Using the transmit dipole orientation ($\boldsymbol{x}_{opt} = \bar{\boldsymbol{K}}^{-1}\boldsymbol{h}$) that maximizes the efficiency in Eq. 2.24, the frequency that maximizes the optimized efficiency due to transmit dipole orientation is calculated [23]. The optimized efficiency using the transmit dipole orientation is as follows

$$\eta = \frac{|k|^2 A_r^2 \mathrm{Re}\ \frac{1}{Z_L}}{\omega\epsilon_0 \mathrm{Im}\ \epsilon_r} \boldsymbol{h}^\dagger \bar{\boldsymbol{K}}^{-1} \boldsymbol{h} \tag{2.29}$$

Assuming that d_1 (the distance from source to interface) is much smaller than the skin depth, the optimal frequency to maximize Eq. 2.29 can be calculated as

$$f_{opt} \approx \frac{1}{2\pi} \sqrt{\frac{c\sqrt{\epsilon_{r0}}}{\tau d(\epsilon_{r0} - \epsilon_\infty)}} \tag{2.30}$$

where c is the speed of light.

The optimal frequencies for 17 different biological tissue types are given in Table 2.6, assuming $d = 1$ cm [23]. According to [23], the optimal frequencies even exceed 1 GHz for tissue thickness of 10 cm. Note that, the transmit antenna's distance to tissue is assumed to be much smaller than the skin depth. All of these frequencies fall in the low-GHz range. At the optimal frequency, the efficiency is lower bounded by a term which decays by the inverse cube of the transmit-receive separation ($1/d^3$). In the far-field, the efficiency is proportional to the inverse square of the separation distance, and in the near-field, the efficiency is inversely proportional to the 6th power of the transmit-receive separation. Therefore, we can conclude that the optimal efficiency is somewhere in between the near field and the far field.

As a numerical example, energy transfer in muscle is considered in [23]. The receive coil is considered to have an area of 2 mm^2 and a 45° angle with respect to

Table 2.6: Approximate Optimal Frequency for Electromagnetic Energy Transfer through 17 Different Biological Tissues, using Coils as Antennas with Transmit-Receive Separation of 1 cm [23].

Type of Tissue	Approximate Optimal Frequency (GHz)
Blood	3.54
Bone (cancellous)	3.80
Bone (cortical)	4.50
Brain (gray matter)	3.85
Brain (white matter)	4.23
Fat (infiltrated)	6.00
Fat (not infiltrated)	8.64
Heart	3.75
Kidney	3.81
Lens cortex	3.93
Liver	3.80
Lung	4.90
Muscle	3.93
Skin (dry)	4.44
Skin (wet)	4.01
Spleen	3.79
Tendon	3.17

the z-axis. The transmit coil is considered to have the optimal orientation in the range of 10 MHz and 10 GHz. Under these assumptions, the maximum efficiency and also the frequency which maximizes the efficiency have been plotted versus the implant's depth $(d - d_1)$ in muscle tissue in Fig. 2.6.

According to [41], the muscle thickness in an L1 position of the spinal cord in the neutral posture is approximately 2.5 cm. Based on this value and the plots in Fig. 2.6, the optimal frequency for muscle tissue lies in the range 2-3 GHz. If we want to choose an FCC-approved medical band that matches this optimal frequency, the best choice will thus be the ISM 2.4-GHz band.

2.5.2 Energy Transfer in Multiple Layers of Tissue

In Sec. 2.5.1, the transmitter was considered to be very close to the tissue interface, which made the analysis approximately equivalent to energy transfer through a homogeneous medium. In this section, the transmitter is not necessarily close to the tissue interface and therefore reflection losses at the interfaces have to be considered

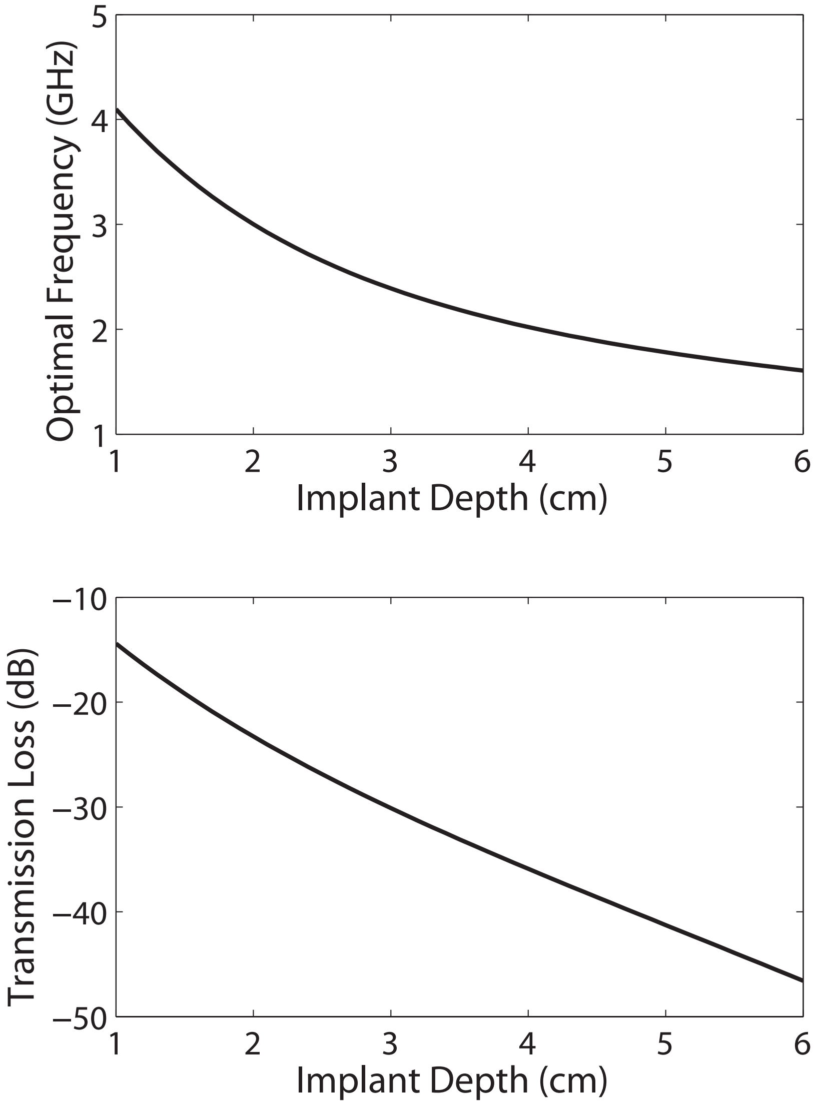

Figure 2.6: Optimal frequency and transmission loss assuming that $d_1 = 2$ mm, receive dipole tilted by 45°, $A_r = 2\ \text{mm}^2$, and $Z_L = 1\ \Omega$ [23].

in the equations. Two scenarios of tissue layers have been considered in this section, one is one layer of tissue and the other is three layers of tissue (air-skin-fat-muscle, as shown in Fig. 2.7). Based on how big the transmitter coil is, we can consider the transmitter to be a magnetic dipole source or a uniform source region.

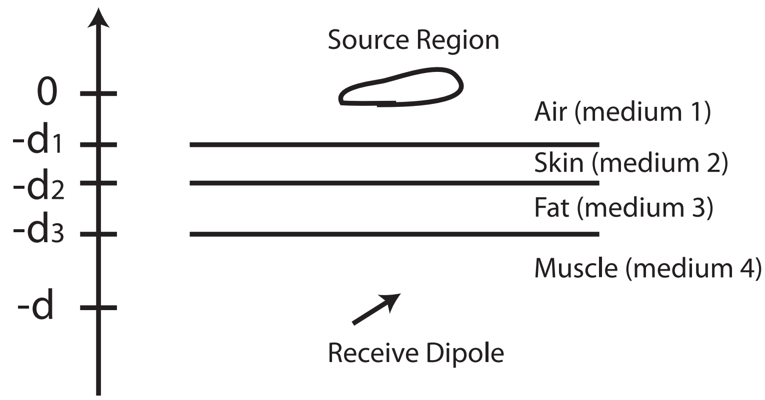

Figure 2.7: Multiple layers of medium, modeled as planar layers [23].

Magnetic Dipole Source

A very small circular loop current results in a vector potential field that is analogous to the scalar potential field produced by electric dipoles, with only small variable changes. Here a small loop size is defined relative to the distance within which the magnetic field is calculated, and this separation distance must be much larger than the radius of the loop. By analogy with the electric dipole, a very small current loop is called a magnetic dipole. This model for a magnetic dipole is called the Ampère model. Interestingly this model can be used to explain why splitting a magnet in two parts still results in two independent magnets [35, 4].

Under the assumption of a very small loop, the optimal efficiency with the optimal orientation of the transmit dipole becomes

$$\eta_{opt} = \frac{A_r^2 \mathrm{Re}\ \frac{1}{Z_L}}{\omega\epsilon_0} \sum_{m\in\{x,y,z\}} \frac{|\beta_m|^2 |\boldsymbol{\psi}_m(-\hat{\boldsymbol{z}}d)|^2}{\int_{z<-d_1} \mathrm{Im}\ \epsilon_r(\boldsymbol{r}) |\boldsymbol{\xi}_m(\boldsymbol{r})|^2 \,\mathrm{d}\boldsymbol{r}} \tag{2.31}$$

Unlike the homogeneous case, a closed form expression for the summation terms is not feasible; therefore, a closed form optimal frequency is not available.

Numerical methods are used for the case where the transmit dipole is located 1 cm above the tissue interface and the receive dipole is tilted 45° tilted with respect to the z axis. In the air-skin-fat-muscle case, the skin and fat thicknesses are assumed to be 2 mm and 5 mm, respectively. The efficiency and also the optimal frequency for the layered tissues are plotted in Fig. 2.8 for different implant depths. The variation of the efficiency versus the implant depth $(d - d_1)$ remains approximately inversely proportional to d^3, and the results are quite comparable to the homogeneous case.

Considering a muscle thickness of ∼2.5 cm in the L1 position of the spinal cord [41], the optimal frequency for the energy transfer in an air-skin-fat-muscle configuration according to Fig. 2.8 is in the region of 2-3 GHz. Using this fact the most suitable medical band for energy transfer again turns out to be the 2.4-GHz ISM band.

Uniform Source Region

If we assume a uniform square loop antenna of area A_t with uniform current I_t, the efficiency will also depend on the area of the transmitter loop antenna [23].

For $A_t = 2$ cm^2, the optimal efficiency and frequency have been plotted versus the implant depth $(d - d_1)$ in Fig. 2.9 [23]. As we can see in the muscle thickness of 2.55 cm, the optimal frequency for energy transfer using this configuration is a bit less, around 1.5-2 GHz. The closest medical bands for this configuration are the 900-MHz and 2.4-GHz ISM bands.

2.5.3 Experimental Validations

As an experimental verification of the concept, an experiment was conducted in [42]. The experiment includes an air-skin-fat-bone tissue configuration as in case of a brain-computer interface application. The transmitter is a square loop antenna of size 20 mm^2 and the receiver is a square loop antenna of size 1 mm^2. The skin and bone thicknesses are 6 mm and 13 mm, respectively. In the rat's case, the

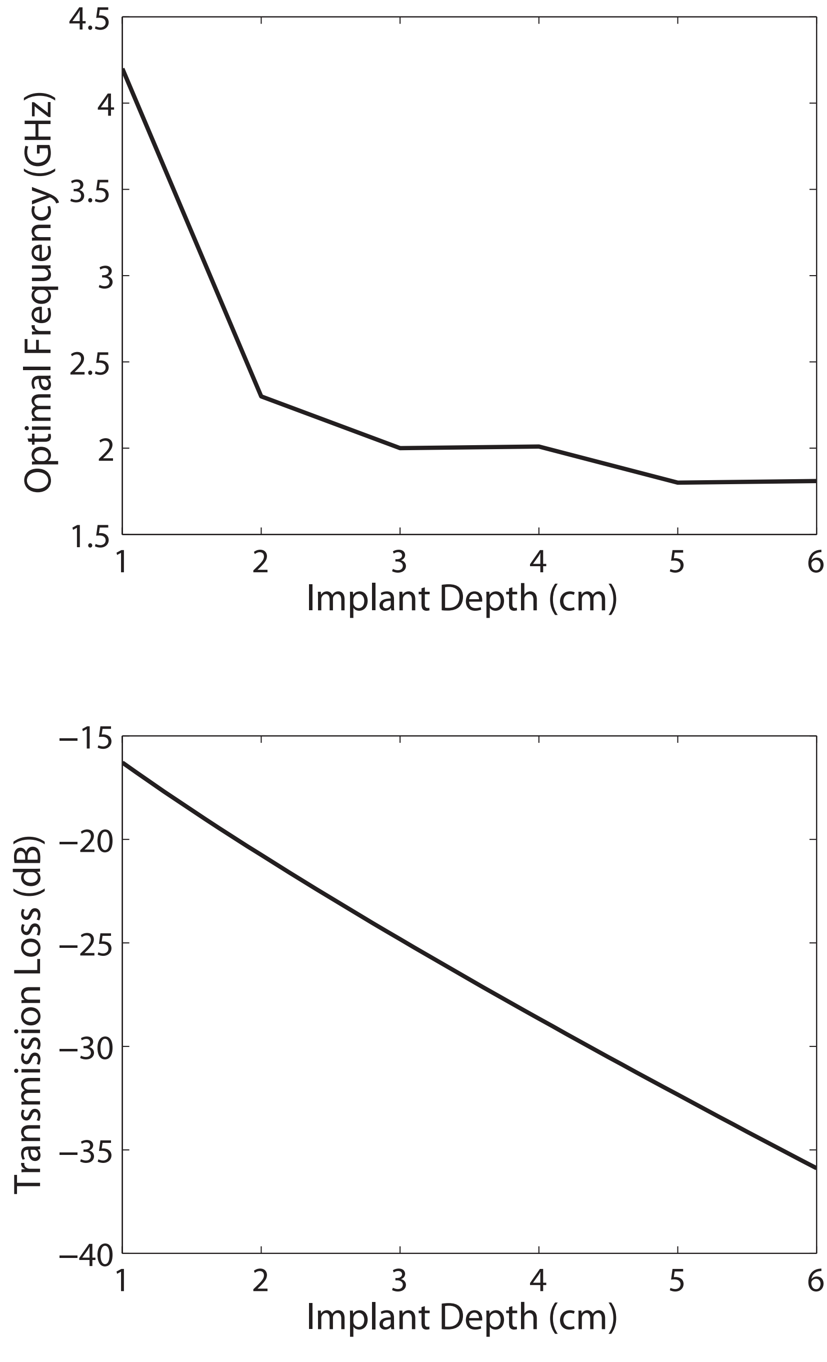

Figure 2.8: Optimal frequency and efficiency assuming that (d_1, d_2, d_3) = (1 cm, 1.2 cm, 1.7 cm), receive dipole tilted by 45°, $A_r = 2$ mm^2, and $Z_L = 1\ \Omega$ [23].

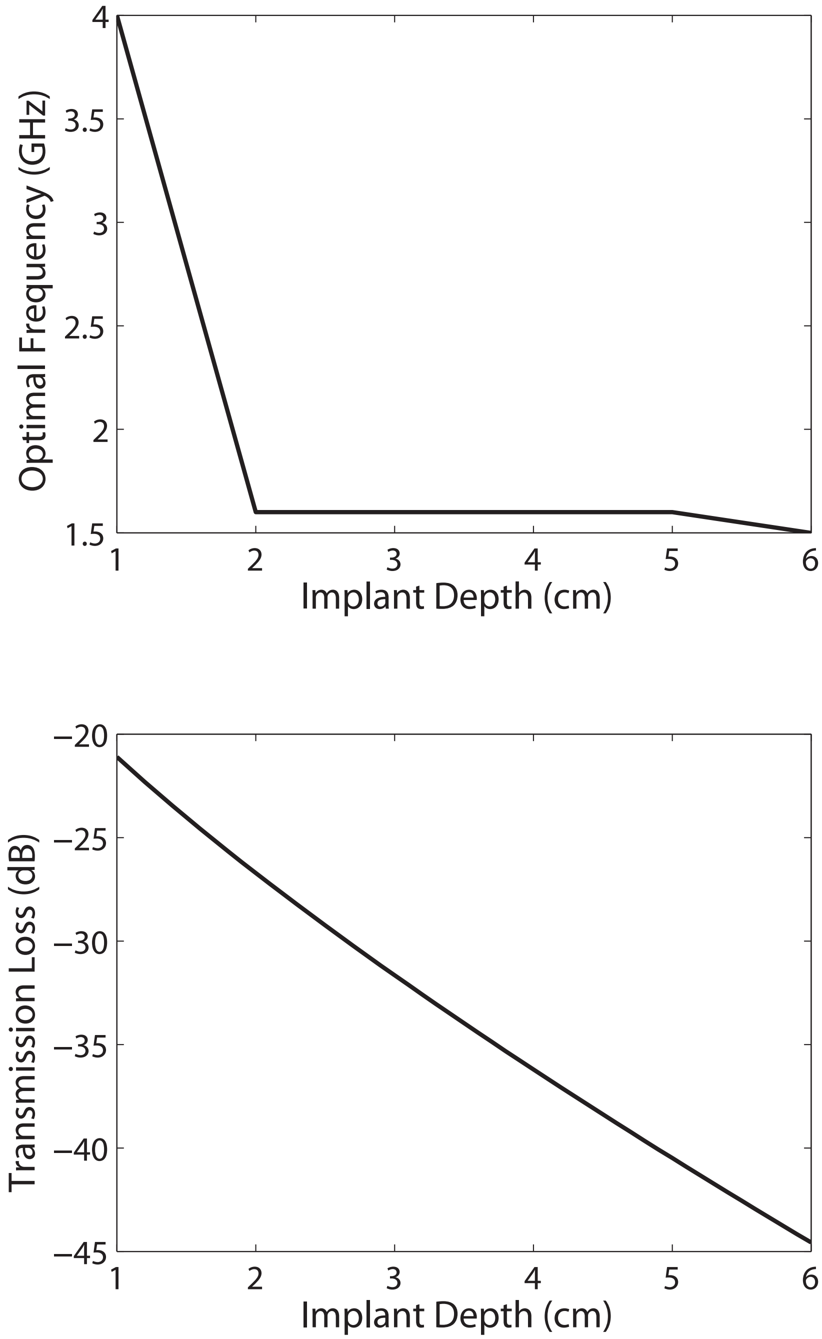

Figure 2.9: Optimal frequency and efficiency assuming that $(d_1, d_2, d_3) = (1$ cm, 1.2 cm, 1.7 cm), receive dipole tilted by $45°$, $A_r = 2\ \mathrm{mm}^2$, $A_t = 2\ \mathrm{cm}^2$, and $Z_L = 1\ \Omega$ [23].

thicknesses of skin and bone are 0.9 mm and 1 mm respectively. In both cases, the air gap is 4 mm and most of the fat is surgically removed. As a result the maximum gains achieved are -30 dB and -25 dB in pig and rat experiments, respectively. The optimal frequency as seen in [42] (Fig. 3) is in the range of 2-4 GHz, which matches the conclusions in [23].

In [43], an application of simultaneous conjugate matching for wireless energy transfer has been demonstrated. The transmitter antenna is a loop of 2 cm^2 area, and the receiver is a loop of 2 mm^2. The tissue in between is 1.5 cm of bovine muscle. The gain of the link, rectifier, and the regulator combined is approximately -33.2 dB and the DC output power is 140 μW at a DC regulator output of 1.2 V.

Chapter 3

Link Budget Analysis

3.1 Near-field Data Link Budget

In the case of near-field link-budget, we assume the transmitter and receiver loop antennas to be coupled. As the implant is surrounded by biological tissues, the transmission loss should be taken care of carefully. For the tissue loss values, we use the results of [23].

3.1.1 Uplink

If the antennas are linear and bidirectional and the heterogeneous medium is linear and isotropic, we can conclude that the transfer efficiency is the same on the uplink and downlink paths. According to Fig. 3.1, reproduced from [23], the amount of path loss at the center frequency of the 2.4-GHz ISM band using the setup illustrated on the left is roughly -30 dB. Using different antenna designs may affect the optimal frequency, but transfer efficiencies of around the same value are still achievable. As shown in [44] (Table VI), coil setup realized on FR4 PCB with muscle and air media in between the coils reaches -27.8 dB efficiency for frequency of 915 MHz, this is compared to -28.4 dB in [45].

Before using the reciprocity theorem, we need to prove that this theorem is valid in our case. We assume that the antennas are both bilateral, which means they have the same propagation characteristics, regardless of transmission or reception. About

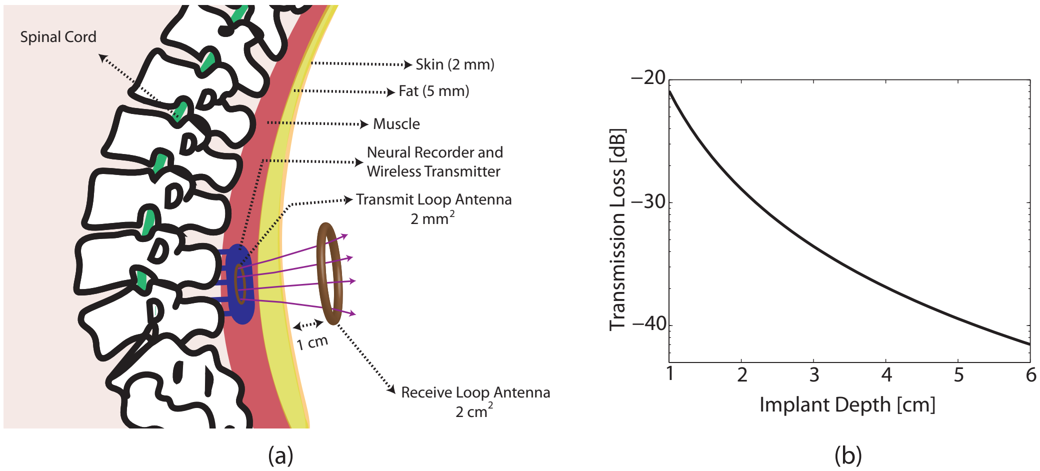

Figure 3.1: Coupled energy transfer characteristics: (a) location of the transmitter close to the spinal cord and the receiver above the skin, (b) the associated optimal path loss ([23]) for the optimal frequency.

the medium in which the waves propagate, the biological tissues are assumed to be linear and isotropic, which means that the dielectric properties are independent of the radiation direction, and this makes the loss in each homogeneous biological tissue independent of direction. The last things to consider in order to conclude reciprocity of the medium are the boundary conditions. In the special case of a plane-wave, the reflection coefficient from medium one to medium two can be calculated as $\Gamma = (\eta_2 - \eta_1)/(\eta_2 + \eta_1)$. The reflection coefficient from medium two to one differs difference of π radians, but has the same magnitude. In case needed, the reciprocity should also be analyzed for the general case where the electromagnetic field is not assumed to be plane-wave. For simplicity, we assume planar wave propagation.

Noise in the 2.4-GHz ISM band

To calculate the amount of the received signal-to-noise ratio (SNR), it is important to model the noise correctly. In this part, we consider the noise power spectral density (PSD) at the receiver in case of coupled uplink communications from an implant to an external receiver in the 2.4-GHz ISM band.

The noise calculations in this part are done assuming an implanted transmitter and an external receiver. Noise modeling on the downlink, where the signal is transmitted from the external control unit to the implanted chip will differ due to the tissue loss attenuation of interfering signals from other systems working in the same frequency band.

The noise power spectral density (PSD) in the 2.4-GHz ISM band is not the usual thermal noise, but includes man-made activity in this congested band, which includes WiFi and Bluetooth systems. Experimental measurements of noise levels in the 2.4-GHz ISM band are reported in [46]. These measurements were made in the San Francisco Bay area, using a custom L and S band Spectrum Measurement (LSSM) system with a noise figure of 3 dB. The temperature in which the measurements were made was $T = 296$ K, which leads to a thermal noise power spectral density of -114 dBm/MHz. The noise value was measured by two antennas with different receiver polarizations and a 50-Ω load was used to verify that the correct thermal noise level is assumed. Averaging the values from the two urban site measurements (both horizontal and vertical) leads to an average noise PSD of -86 dBm/MHz at a temperature of 296 K. Recall that the receiver has a 3-dB noise figure. By subtracting the noise figure, we end up with an average -89 dBm/MHz noise power spectral density in the 2.4-GHz ISM band at 296 K. Therefore, we can conclude that man-made sources exceed the thermal noise floor by roughly 25 dB.

Table 3.1: Measured Received Noise in the 2.4-GHz ISM Band.

Site	Average (dBm/MHz)			Standard Deviation (dBm/MHz)		Percentage of man-made signal (%)		Average of HOR and VER (dBm/MHz)
	HOR	VER	50 Ω	HOR	VER	HOR	VER	
Urban I	-83.1	-84.4	-111.1	-66.6	-67.5	6.08	4.50	-84
Urban II	-92.2	-89.9	-111.3	-71.5	-70.1	4.35	3.58	-91

For more information about the spectrum occupancy of noise, we refer to [46] (Fig. 10), which plots the power spectral density (PSD) of the noise in the 2.4-GHz ISM band.

In biomedical applications, since the receiver antenna is facing the body, the antenna temperature is 37 °C (310.15 K). This leads to an approximate thermal noise power spectral density of -113.5 dBm/MHz, which still leads to a number close to -89 dBm/MHz with inclusion of 25 dB noise level increase effect by man-made sources.

The man-made signals mostly originate from sources for which the receive antenna is in the far-field. A loop antenna has a low radiation resistance, which reduces the effective area and therefore the received far-field man-made signal power. An antenna's effective area is the ratio of the available power at the terminals of a receiver antenna to the incident plane-wave's power flux density. The amount of received noise depends on the antenna's maximum effective area, which is calculated as follows (assuming small single-turn circular receive loop and plane-wave man-made signals) [3]

$$A_{em} = \left(\frac{R_r}{R_r + R_L}\right) \cdot \left(\frac{3\lambda^2}{8\pi}\right) \tag{3.1}$$

where $R_r = 20\pi^2(C/\lambda)^4$ is the radiation resistance, and $R_L = (C/2\pi b)\sqrt{\omega\mu_0/2\sigma}$ is the loss resistance. C is the loop's circumference, b is the wire radius, and σ is the wire conductivity. We have assumed no reflection loss and no polarization mismatch. In the antenna's equivalent circuit, the radiation resistance (R_r) is the equivalent resistance accounting for the amount of radiation and the loss resistance (R_L) is the equivalent resistance accounting for the ohmic antenna losses.

Even assuming no reflection loss and no polarization mismatch the calculations lead to -27.65 dB maximum effective area for the receiver loop antenna with 2 cm^2 area and 0.5 mm wire radius. This means that man-made noise is not a dominant noise source for a typical loop antenna and the noise level is roughly equal to the thermal noise level.

Quality of Reception

The quality of reception using spread spectrum modulated packet transmission is determined by two probabilities: one is the probability of missing a packet and the second is the probability of having a false alarm [47]. To have a certain amount of reception quality, $P(miss)$ and $P(false)$ are considered to be 10^{-6} and 10^{-3}, respectively. According to [47], the signal-to-noise ratio (SNR) for the packet preamble is defined as $\mathrm{SNR_p} = PL_bE_c/N_0$, where L_b is the processing gain, P is the preamble length, and E_c/N_0 is the energy of each chip over the noise power spectral density. Using Fig. 3 in [47], the values of $P = 10$ and $L_b = 5$ where used, together with the assumptions that P(miss) = 10^{-6} and P(false) = 10^{-3}, the required $\mathrm{SNR_p}$ should roughly be 17 dB for the preamble. Based on the definition of the preamble SNR, E_c/N_0 value should be equal to 0 dB. Since the SNR for the carrier signal is defined as $\mathrm{SNR} = 10\log\big((E_c/N_0)\cdot(R_c/W_n)\big)$, we calculate the SNR as $10\log\big((10^{1.7}/50)\cdot(R_c/W_n)\big)$, where R_c is the chip rate and W is the noise bandwidth.

Link Budget

To calculate the uplink budget we go through a procedure explained here: We first assume the required amount of reception quality, then using this assumption we can calculate the required E_b/N_0 in the receiver side, as described in Section 3.1.1. We calculate the noise floor in the receiver side as well as the path losses that attenuate the signal to reach the receiver from the transmitter. We also add relevant excess loss and fade margins to the link budget to account for unexpected losses in the link. Using all of these information the required transmit power can be calculated in terms of the data rate. We can also calculate the required bandwidth for transmission using the spectral efficiency of the modulation scheme and the data rate.

As explained in Sec. 3.1.1, to achieve minimum reception quality, the required E_c/N_0 has to be no less than 0 dB. With $L_b = 16$, we have: $E_b/N_0 = L_b \cdot E_c/N_0 =$ 12 dB. The received SNR is given by

$$SNR = 10\log\left(\frac{E_c}{N_0}\cdot\frac{R_c}{W_n}\right) \tag{3.2}$$

where R_c is the chip rate in Hz and W_n is the noise bandwidth in Hz.

The received signal power is the transmit power that remains after overcoming path losses and antenna directional gains, and is given by

$$P_R = P_T + P_L \quad \text{[dBm]} \tag{3.3}$$

where P_L is the total path loss in dB, including the tissues, free path loss and the antenna gains, and P_T is the transmit power in dBm.

The noise power in the receiver can be expressed as in Eq. 3.4. The noise power spectral density in the 2.4-GHz ISM band is calculated as explained in Sec. 3.1.1.

$$P_N = \mathrm{PSD_n} + 10\log(W_n) + \mathrm{NF} \quad \text{[dBm]} \tag{3.4}$$

where $\mathrm{PSD_n}$ is the noise spectral density in the 2.4-GHz ISM band, and NF is the receiver noise figure in dB, which is due to noise enhancement by the receiver's own circuitry. In our case, the PSD_n is equal to thermal noise and is calculated as $10\log(kT_0 \cdot 10^3)$ in dBm/Hz, where k is the Boltzmann constant and T_0 is the ambient temperature.

Recall that the SNR in dB is the difference of the received signal power and noise ($\mathrm{SNR} = P_R - P_N$). Using this equation and then Eqs. 3.2, 3.3 and 3.4, the required transmit power to achieve a certain quality of reception is given by

$$P_T = 10\log\left(R_c \cdot \frac{E_c}{N_0}\right) + 10\log(kT_0 \cdot 10^3) + \mathrm{NF} - \mathrm{P_L} \quad \text{[dBm]} \tag{3.5}$$

The energy required to transmit one chip from the transmitter antenna to the receiver antenna, E_{ct}, is given by

$$E_{ct} = \frac{P_T - P_R}{R_c} \quad \text{[J/chip]} \tag{3.6}$$

where R_c is in Hz, P_T and P_R are in W, and E_{ct} is in J/chip.

Using Eq. 3.3, received power is calculated as

$$P_R = P_T \cdot 10^{(P_L/10)} \quad \text{[W]} \tag{3.7}$$

Using Eq. 3.5, the value of the transmitted power in watts can be calculated as

$$P_T = (kT_0 \cdot R_c \cdot \frac{E_c}{N_0}) \cdot 10^{((NF-P_L)/10)} \quad [\mathrm{W}] \tag{3.8}$$

By substituting Eq. 3.8 into Eq. 3.7 and substituting Eqs. 3.7 and 3.8 into Eq. 3.6, the energy to transmit one chip is calculated as follows

$$E_{ct} = kT_0 \cdot \frac{E_c}{N_0} \cdot 10^{((NF-P_L)/10)} \cdot \left(1 - 10^{(P_L/10)}\right) \quad [\mathrm{J/chip}] \tag{3.9}$$

The energy to transmit one bit is then $E_{bt} = E_{ct} \cdot L_b$, where L_b is the processing gain. Therefore, the energy to transmit one bit is approximately computed as

$$E_{bt} \approx kT_0 \cdot \frac{E_b}{N_0} \cdot 10^{\left((NF-P_L)/10\right)} \quad [\mathrm{J/bit}] \tag{3.10}$$

where the last factor on the right hand side of Eq. 3.9 is omitted as it is negligible.

Added to the known factors in the link budget, we should also account for some margins as of several different circumstances. In a report by ITU-R [48] using the MICS band (401-406 MHz) the fading margin is introduced to be 10 dB in a non-spread-spectrum FSK transmission. For excess loss, which accounts for patient orientation, antenna misalignment and obstructions, 15 dB of margin is assumed. These numbers have been used in [28] as well as approximately the same numbers used in [49] for 2.4-GHz ISM band. Although our previous calculations show insignificant reception from other transmitters in the same band by loop antenna, we use more pessimistic assumptions and we account for 25 dB of loss due to possible interference from other transmitters in the same band. We use 25 dB according to the current knowledge described before that noise spectral density in the 2.4-GHz ISM band is roughly 25 dB more than the thermal noise level. This number may also account for other losses, including implementation and polarization losses. Without loss of generality, we can include these extra losses with negative value in the P_L parameter in the above-mentioned equations of this section.

The uplink budget is detailed in Table 3.2 [50]. To calculate the required transmit power for a specific data rate, we multiply the transmission energy per bit (in this case $\sim$ 68 pJ/bit) by the data rate. For example, to achieve a data rate of 2 Mbps, the required transmit power is equal to $\sim$ 68 pJ/bit$\times$2 Mbps $\approx$ 136 μW or -8.6 dBm.

Table 3.2: Link Budget Values to Achieve P(miss) $= 10^{-6}$ and P(false) $= 10^{-3}$ using Spread Spectrum Modulation in the 2.4-GHz ISM Band.

Parameters	**Value**
Desired Quality of Reception	$P(miss) = 10^{-6}$ & $P(false) = 10^{-3}$
Required E_b/N_o	12 dB
Receiver Noise Figure	10 dB
Thermal Noise	-174 dBm/Hz
Extra Man-Made Noise Margin	-25 dB
Path Loss (2 cm tissue depth)	-30 dB
Fading / Orientation Loss Margin	-10 dB
Excess Loss	-15 dB
Energy Required to Transmit a Bit	68 pJ/bit
Approximate Required Transmit Power (Assuming data rate of 2 Mbps)	-8.6 dBm

If we use BPSK modulation alongside Direct-Sequence Spread Spectrum (DSSS) with processing gain of 16 to have a sampled data rate of say 2 Mbps, we require 64 MHz of bandwidth. This is because the BPSK modulation's spectral efficiency is 0.5 bps/Hz [51], and the processing gain increases the required channel bandwidth by 16. This required bandwidth is less than the maximum 2.4-GHz ISM bandwidth of 83.5 MHz.

To summarize the references used for the link budget analysis, we have used the article [47] to find the required E_b/N_o for the desired quality of reception. The receiver noise figure is selected to be 10 dB assuming a moderate receiver noise. Thermal noise has been calculated using the Boltzmann's formula. The extra man-made noise margin is used from the experimental article [46]. Near-field path loss amount is concluded from the article [23]. As mentioned before, we have used ITU-R recommendations for the MICS band [48] for fading margin and excess loss. The same margin numbers have been used in [28] and for the 2.4-GHz ISM band in [49].

The loss numbers in the link budget are overestimating the amount of real loss, as there has been several margins included, which may overestimate the real losses. As we showed before, a small loop antenna has a small effective area, which leads to less signal reception from a far-field interferer. Therefore, less than 25 dB of man-made interference could happen in a real setup. The thermal noise considered is a mean value as thermal noise has a Gaussian distribution. The noise figure is a typical value and as we have enough flexibility in designing an external receiver, it even overestimates the potential receiver's noise figure. The path loss is a typical value according to the referred article and also the considered tissue depths. The excess loss and orientation or fading margins are also middle of the road values. Therefore, we can conclude that the overall link budget is likely to be overestimating the losses. This permission should guarantee the quality of reception given the recommended transmit power.

3.1.2 Downlink

The downlink can be used for both powering the implant and data communications. Since the path loss is the same for the up- and downlink [23] and given that the man-made signals are attenuated in human tissue but still keeping the margin, we can use the same link budget as the uplink. We conclude that around 68 pJ/bit is required to transmit one bit in the downlink using the spread spectrum modulation scheme. However, some of the losses may not be realistic in the downlink, e.g. the extra man-made noise which is insignificant on the implant as shown later in this chapter. Assuming negligible man-made interference and no fading margin and only accounting for excess loss, which includes orientation mismatch effect, we can conclude that the required energy to transmit one bit through the tissues in the near-field downlink is roughly 22 pJ/bit.

It has been shown in [23] that up to 1 mW of power could be transfered to a mm-sized receive antenna by a cm-size transmit antenna within a few cm of separation. This amount is enough to power a low-power implant for continuous real-time operation. In our case, we are expecting a few milliwatts of required implant power including the neural recording, baseband and RF communications. This may necessitate a rechargeable battery or another powering scheme, such as ultrasound, for real-time powering.

Noise Attenuation

As described in Sec. 3.1.1, the noise power spectral density in the 2.4-GHz ISM band is roughly 25 dB above the usual thermal noise. To calculate the amount of man-made noise contribution at the implanted receiver, we model the man-made source in the 2.4-GHz ISM band as a separate transmitter. We assume that the modeled transmitter is located far enough from the body skin and for simplicity we assume that the received electromagnetic wave is a plane wave. The assumption of far-field radiation is reasonable because most of the devices working in the same 2.4-GHz frequency band are located far from the body.

Recall that the man-made sources contribute around 25 dB of the total noise PSD.

We assume the tissue model shown in Fig. 2.7, with 2.5 cm of muscle in the L1 position, 0.5 cm of fat, and 0.2 cm of skin. Using the in-body path loss models derived in [52], we can calculate the path loss due to homogeneous tissues. The path loss model in 2.457 GHz frequency, which is based on electromagnetic simulations and is validated with measurements [52], is as follows

$$P_L|_{dB} = \begin{cases} (10\log_{10} e^2)\ \alpha_1\ d + C_1|_{dB} & , d < d_{bp} \\ (10\log_{10} e^2)\ \alpha_2\ d + C_2|_{dB} & , d \geq d_{bp} \end{cases} \tag{3.11}$$

where α_1 and α_2 are the attenuation constants [1/cm], d is the separation of transmitter and receiver, d_{bp} is the separation from which the coupling breaks, and $C_1|_{dB}$ and $C_2|_{dB}$ are two constants.

The parameters α_1, α_2, $C_1|_{dB}$ and $C_2|_{dB}$ can be calculated from the following formulas:

$$\alpha_1 = (A_1 e^{(B_1 \epsilon_r)} + D_1) \cdot (E_1 \sigma + F_1) \text{ for } d < d_{bp} \tag{3.12a}$$

$$\alpha_2 = (A_2 e^{(B_2 \epsilon_r)} + D_2) \cdot (E_2 \sigma + F_2) \text{ for } d \geq d_{bp} \tag{3.12b}$$

where A_1, A_2, B_1, B_2, D_1, D_2, E_1, E_2, F_1, and F_2 are the constants used in the model [52].

$$C_1|_{dB} = (U_1 e^{(V_1/\epsilon_r)} + W_1) \cdot (X_1 \sigma + Y_1) \text{ for } d < d_{bp} \tag{3.13a}$$

$$C_2|_{dB} = (U_2 e^{(V_2/\epsilon_r)} + W_2) \cdot (X_2 \sigma + Y_2) \text{ for } d \geq d_{bp} \tag{3.13b}$$

where U_1, U_2, V_1, V_2, W_1, W_2, X_1, X_2, Y_1 and Y_2 are the constants used in the model [52].

For the dielectric parameters used in the equations for α and C parameters, we can use the values from [53]. The dielectric parameters are $(\epsilon_r, \sigma) = (50.8$ F/m, 2.01 S/m), $(\epsilon_r, \sigma) = (5.28 \text{ F/m}, 0.10 \text{ S/m})$ and $(\epsilon_r, \sigma) = (38 \text{ F/m}, 1.46 \text{ S/m})$ for muscle, fat, and skin tissues, respectively.

Using these numerical values, the path loss in each muscle (2.5 cm), fat (0.5 cm), and skin (0.2 cm) tissues are roughly -28.7 dB, -7 dB, and -10.3 dB, respectively.

Added to the homogeneous tissue path losses, we must also consider the return losses due to the transition from each tissue to the other one. Using the 4-term Cole-Cole model [36] for the dielectric properties of the tissues, numerical values of the dielectric parameters from [54] and also the reflection coefficients, we can determine the reflection losses. The Cole-Cole model is as follows:

$$\epsilon_r(\omega) = \epsilon_\infty + \sum_n \frac{\Delta\epsilon_n}{1 + (j\omega\tau_n)^{(1-\alpha_n)}} + \frac{\sigma_i}{j\omega\epsilon_0} \tag{3.14}$$

where $\epsilon_r(\omega)$ is the complex relative permittivity, the magnitude of the dispersion is defined as $\Delta\epsilon = \epsilon_s - \epsilon_\infty$, ϵ_∞ is the permittivity at field frequencies where $\omega\tau \gg 1$, ϵ_s is the permittivity at $\omega\tau \ll 1$, σ_i is the static ionic conductivity, ϵ_0 is the permittivity of free space, and the distribution parameter α is a measure of the broadening of the dispersion. The number of summations depends on the dispersion regions. We use a 4-term Cole-Cole model. By choosing the parameters related to each tissue, the dielectric behavior over the desired part of the spectrum can be predicted.

The reflection coefficient due to medium transition from medium one to medium two is shown in Eq. 3.15, where $\eta_1 = \sqrt{\mu_1/\epsilon_1}$ and $\eta_2 = \sqrt{\mu_2/\epsilon_2}$ are the complex intrinsic impedances of the media one and two, respectively. Magnetic permeability can be written as $\mu = \mu_r\mu_0$, where for biological tissues μ_r is usually unity. Electric permittivity is also written as $\epsilon = \epsilon_r\epsilon_0$.

$$\Gamma = \frac{\eta_2 - \eta_1}{\eta_2 + \eta_1} \tag{3.15}$$

Including the values of the dielectric parameters from [54] (Table 1) for skin, fat, and muscle, the amplitude of the reflection coefficients can be calculated as: 0.74 for air to skin, 0.49 for skin to fat, and 0.52 for fat to muscle. Using the reflection coefficients, the reflection losses can be calculated by $RL = -20\log_{10}|\Gamma|$. The total approximate path loss for the noise of 2.4-GHz ISM band is then calculated as follows:

$$\begin{aligned} PL = -(&-20\log|\Gamma_{air-skin}| + PL_{skin} - 20\log|\Gamma_{skin-fat}| \\ &+ PL_{fat} - 20\log|\Gamma_{fat-muscle}| + PL_{muscle}) \end{aligned} \tag{3.16}$$

Using the numerical values, the total path loss for the noise in the 2.4-GHz frequency is approximately -60.5 dB.

Normalizing the power for one MHz and using the numerical values -114 dB-m/MHz for the thermal noise PSD and 25 dB for the man-made contribution, the total man-made noise normalized for one MHz of frequency is calculated roughly as $P_{mm} \approx -89$ dBm.

Assuming man-made noise to have plane-wave far-field radiation on the biological tissues, we can conclude that the wave by passing the tissues and teaching the implanted receiver antenna has -60.5 dB of path loss including the homogeneous tissue path losses and the reflection coefficients. This loss is much more than the 25 dB man-made contribution to the noise power spectral density in 2.4-GHz ISM frequency band. Thus, we can neglect the effect of the man-made sources on the noise power spectral density on the implant's side.

This result leads to the conclusion that for the downlink, a communications scheme that is much simpler than DBPSK-DSSS can be used because much less interference mitigation is needed in the downlink compared to the uplink in the 2.4-GHz ISM band.

3.2 Far-field Data Link Budget

It is also interesting to know how the link performs when the antennas are further separated. When the separation distance of the antennas becomes roughly more than $2D^2/\lambda$, we can say that the pattern of radiation does not depend on distance anymore and we can use usual antenna formulations to derive the link budget. There also exists some specific challenges, which are explained in the appropriate sub-section.

3.2.1 Downlink

In this case, we consider the transmission from the external antenna towards the implanted receiver antenna. In the calculations, we assume that antennas are separated enough so the radiation reached the skin of the person is in the far-field and we can also model the field as plane wave.

The received power by the implanted antenna can be given as follows:

$$P_R = P_T + G_T - P_{L\_FS} - R_{L\_AS} - R_{L\_SF} - R_{L\_FM} - P_{L\_S} - P_{L\_F} - P_{L\_M} + G_R \quad (3.17)$$

where P_R is the received power in dBm, P_T is the transmitted power in dBm, G_T is the transmitter gain, P_{L_FS} is the free-space path loss in dB, R_{L_AS} is the return loss from air to skin, R_{L_SF} is the return loss from skin to fat, R_{L_FM} is the return loss from fat to muscle, P_{L_F} is the path loss in skin tissue, P_{L_F} is the path loss in fat tissue, P_{L_M} is the path loss in muscle tissue, and G_R is the receiver gain.

We assume the same size of antennas as in [23] (Section V), which is a square loop antenna with 2-cm sides as the external antenna and a square loop antenna with 2-mm sides as the implanted antenna.

To calculate the gain of the external antenna we need to have the efficiency factor and directivity of the antenna and use the relation $G = \eta D$. For now, we assume an antenna with no efficiency loss and also assume the gain in the direction of the maximum, which is in the direction of the line perpendicular to the center of the antenna. The directivity itself can be calculated by the following formula [3]:

$$D_{max} = \frac{4\pi U_{max}}{P_{rad}} \tag{3.18}$$

where U_{max} is the maximum of radiation intensity and P_{rad} is the total radiated power. The radiation intensity can be calculated by Eq. 3.19 and the total radiated power can be calculated as in Eq. 3.20 [3].

$$U(\theta, \phi) = \frac{r^2}{2\eta}|\mathbf{E}(r, \theta, \phi)|^2 \approx \frac{r^2}{2\eta}(|E_\theta|^2 + |E_\phi|^2) \tag{3.19}$$

where r is the radial distance from the antenna in spherical coordinates, η is antenna efficiency, and $\mathbf{E}$ is the electric field intensity.

To calculate the total radiated power, we need to integrate the radiation intensity over the entire solid angle of a sphere about the antenna position. This integration is as follows:

$$P_{rad} = \int_0^{2\pi} \int_0^{\pi} U \sin\theta \, \mathrm{d}\theta \, \mathrm{d}\phi \tag{3.20}$$

Using the electric field intensity of the square loop in the far-field from [3] (Chapter 5), we can rewrite the radiation intensity as follows:

$$U(\theta, \phi) = \frac{\eta k^2 I_0^2 a^2}{8\pi^2} \sin^2(\frac{ka}{2} \sin\theta) \tag{3.21}$$

To make the Eq. 3.19 integrable, we need to make an approximation for the $\sin(\cdot)$ function. As the wavelength in 2.457 GHz is approximately 0.122 m, the side length of the square loop is approximately equal to $\lambda/6$, where λ is the wavelength in 2.457 GHz frequency. Using this, we can see that the argument in the $\sin^2(\cdot)$ is roughly equal to 0.5 radians at its maximum. Using a Taylor series ($\sin(x) = x - x^3/3! + x^5/5! - \cdots$) and evaluating the Taylor series for $x = 0.5$ rad, the first term becomes 0.5 and the magnitude of the second term becomes 0.021, which is 95.8% less than the first term. Thus, we can approximate $\sin(x)$ with x in our calculations. This result leads to the following equation:

$$U(\theta, \phi) = \frac{\eta k^4 I_0^2 a^4}{32\pi^2} \sin^2\theta \tag{3.22}$$

Using this result and also the point that the maximum occurs in $\theta = \pi/2$ radians, we can calculate the directivity in the direction of maximum as $D_{max} = 1.5$, which is roughly equal to $D_{max} = 1.76$ dB. Assuming $\eta = 1$, $G = 1.76$ dBi as well.

We assume that we could approximate the gain of the receiver insulated antenna surrounded by body tissues with an isolated antenna with the same characteristics in vacuum. As in [3], the gain of a small circular loop antenna is roughly equal to 1.76 dBi.

The transmitted power is limited by two main limitations: one is the Specific Absorption Rate (SAR) and the other is the Equivalent Isotropically Radiated Power (EIRP). According to [55], the EIRP is the dominant limitation for an external antenna for biomedical applications. Based on the FCC sections 15.247 [56] and 15.249 [57], the EIRP limitation for 2.4-GHz ISM band with spread spectrum and antenna gain of up to 6 dBi is 36 dBm. As $EIRP = P_T + G_{ant}$, the maximum allowed transmit power equals to 34.24 dBm or equivalently 2.65 W.

To calculate the free path loss, we can use the following equation [55, 58]:

$$P_L = 10\log\left(\frac{4\pi d_0}{\lambda}\right)^2 + 10\log\left(\frac{d}{d_0}\right)^\gamma + [X] \tag{3.23}$$

where the first term after on the right hand side is the path loss in the reference distance of d_0 from the antenna, γ is the path loss exponent, X is a random variable indicating the deviation and [X] is its mean. For the case of free-space propagation ($\gamma = 2$), the formula simplifies to $P_{L\_FS} = 10\log(4\pi d/\lambda)^2 + [X]$. All the terms in the formula are in dB.

Using free-space path loss ($\gamma = 2$) and mean deviation of zero ($[X] = 0$ dB) in Eq. 3.23, the free-space path loss can be calculated as:

$$P_{L\_FS} = 20\log\left(\frac{4\pi d}{\lambda}\right) \tag{3.24}$$

The reflection coefficients (Γ) are calculated for frequency of 2.457 GHz at Sec. 3.1.2. The magnitude of the reflection coefficients using the dielectric parameters from [54] are: 0.74 for air to skin, 0.49 for skin to fat, and 0.52 for fat to muscle. The reflection loss can be calculated by $R_L = -20\log|\Gamma|$.

The tissue path losses are also calculated in Sec. 3.1.2 and the path loss for muscle (2.5 cm) is 28.7 dB, for fat (0.5 cm) is 7 dB, and for skin (0.2 cm) is 10.3 dB.

Based on the findings mentioned, we can write the received power as in Eq. 3.25. As both the transmitter and receiver antenna gains are approximated by 1.76 dBi and the total loss due to tissue attenuation and return factors is 60.5 dB, the equivalent total loss can be written as $P_L = -56.98 - 20\log(4\pi d/\lambda)$, where the last term is due to free path loss. Using this definition for the total path loss (P_L) and the same spread spectrum modulation as in the near-field case, we can use the Eqs. 3.5 and 3.10 to find the required transmit power and the energy required to transmit one bit of data, respectively. The energy required to transmit each bit is illustrated in Fig. 3.2.

$$P_R = P_T - 56.98 - 20\log(\frac{4\pi d}{\lambda}) \tag{3.25}$$

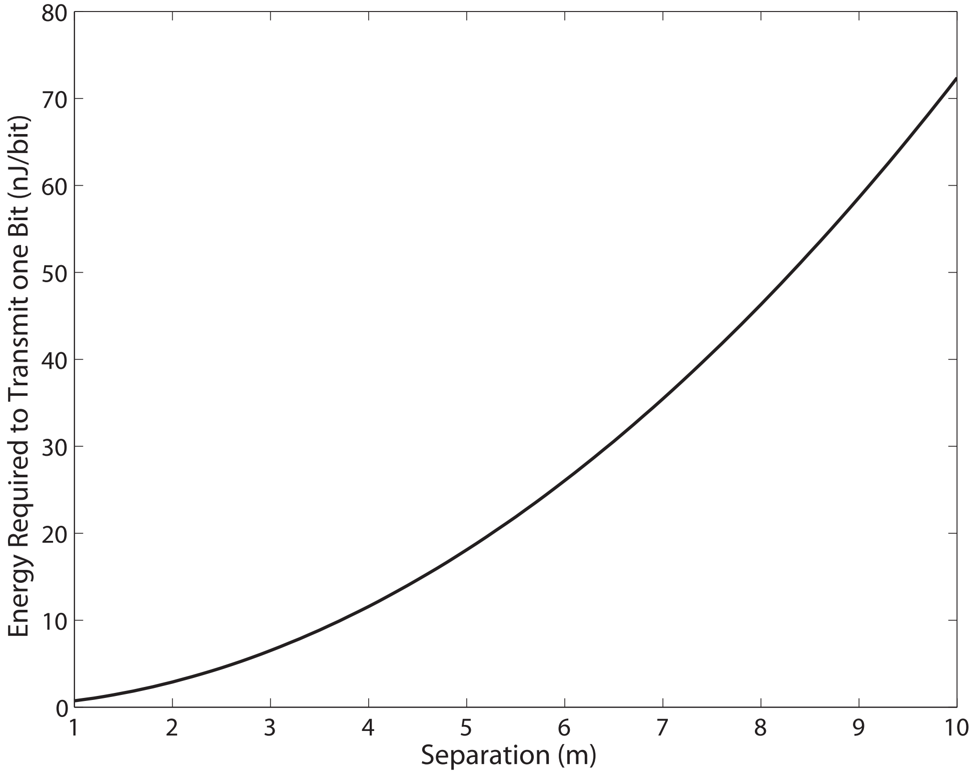

Figure 3.2: Energy required to transmit one bit in the downlink versus the separation from the skin surface.

3.2.2 Uplink

When a transmitter antenna is implanted in biological tissue, its characteristics deviates from an isolated antenna in free space. The gain of transmitter must be considered in presence of the surrounding conducting tissues. As of [59], the definition of antenna parameters change in presence of conducting tissues in the immediate vicinity and the usual free space antenna analysis methods are no longer useful. As a better calculation the antenna and all the surrounding tissues can be combined as one radiating transmitter. This way, the resulting transmission gain can be calculated in the far-field, where the external receiver is outside the patient's body.

More specifically, the method described in [55, 60] is to use an electromagnetic solver to do finite-difference time-domain (FDTD) numerical analysis on the implanted transmitter to find the new antenna gain affected by surrounding body tissues. In these publications, Remcom XFDTD software was used [61]. Using the resulting gain, the link budget can be calculated as follows:

$$P_{rx} = P_{tx} + G_{tx} + G_{rx} + P_L \tag{3.26}$$

where P_{rx} is the received power, P_{tx} is the transmitted power, G_{tx} is the transmitter antenna gain, G_{rx} is the receiver antenna gain, and P_L is the free path loss. Here we have assumed no polarization and impedance mismatches. The free path loss is also assumed in open environment without fading.

The maximum available transmit power is limited by two factors. One is the specific absorption rate (SAR) limitation and the other is the equivalent isotropically radiated power (EIRP) limitation by IEEE standards. In the case of the implanted transmitter and external receiver (uplink), the SAR is usually the bottleneck and in the case of the downlink, EIRP limits are usually more dominant. For free path loss calculations, Friis equation can be used as described before.

For illustrative purposes, a simple implanted patch antenna is simulated using the FDTD methods provided in the Remcom XFDTD software close to the spinal cord in the muscle layer of a full male body model at 2.45 GHz frequency. The patch antenna and the implantation configuration can be seen in Fig. 3.3. The patch antenna size is 20 mm by 32 mm with 2 mm thickness and the relative permittivity of the substrate is 9.5. The FDTD initial mesh cell sizes are set to be equal to patch thickness (2 mm), which is the smallest dimension.

The resulting maximum gain calculated using this method is approximately -44 dBi and is shown in Fig. 3.4.

As future work, one can further analyze the different antenna designs to find the most compatible design for high data rate implantable communications. Furthermore, the specific absorption rate (SAR) conditions should also be taken into account.

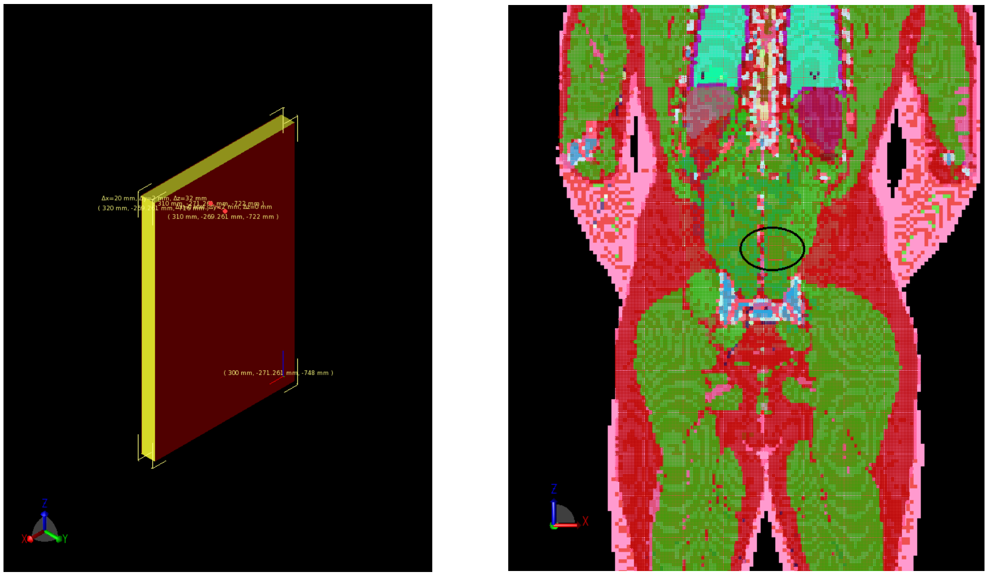

Figure 3.3: FDTD simulation setup using the Remcom XFDTD software: (a) Patch antenna sized as 20 mm × 32 mm × 2 mm, (b) Patch antenna implanted close to spinal cord and the black circle shows the approximate place of implantation.

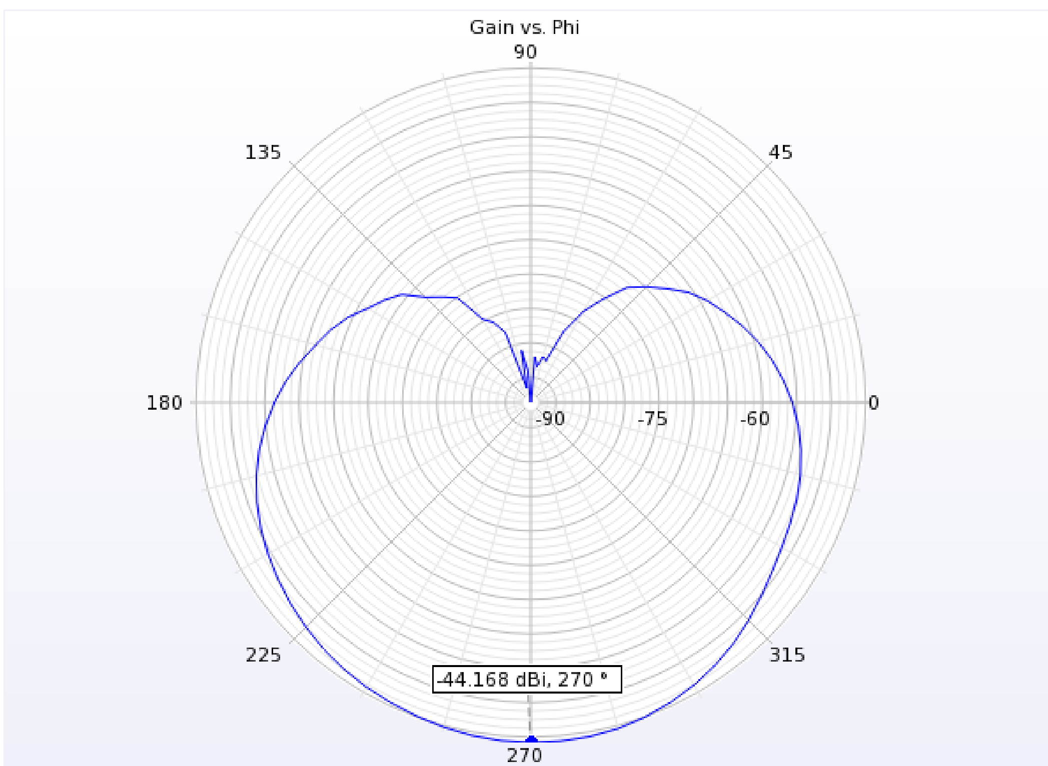

Figure 3.4: Transmit antenna radiation pattern produced by the patch antenna and surrounding tissues considered together.

Chapter 4

Circuitry Power Consumption and Wireless Power Feasibility

It has been shown in [23] that up to 1 mW of power could be transferred to a mm-sized receive antenna by a cm-sized transmit antenna within a few cm of separation. This amount is enough to power a low-power implant for continuous real-time operation. We therefore need to know how much power is expected to be consumed by a typical implantable high data rate transmitter system using spread spectrum modulation in the 2.4-GHz ISM band. As shown in Fig. 3.1, a radio-frequency (RF) wireless transmitter for implant purposes, such as neural recording, consists of a baseband communications subsystem and an RF front-end.

4.1 Power Consumption Estimate at a Nominal Voltage

The current complete version of the baseband transmitter IC in the group was developed in 130 nm IBM technology [62]. Operated at a 1.2 V nominal supply voltage and using a 12.5 MHz chip clock frequency, the chip includes baseband transmitter, testing units and pulse shaping filter. The power consumption is 600 μW and thus the associated energy consumption efficiency is 768 pJ/bit at 12.5 MHz chip clock frequency. The power consumption of the spread-spectrum baseband design can be further reduced by using smaller technology nodes, removing testing units and shaping filter and also operating the circuitry in subthreshold regime [63].

Scaling down to 65 nm technology is expected to result in power reduction [64]. However, smaller than 65 nm technology nodes suffer from more leakage currents, which increase the static power consumption compared to bigger technology nodes. The issue needs further research to mitigate the problem. Using the Synopsys Design Compiler tool, we analyzed the amount of possible power reduction due to using TSMC's 65-nm technology at a 1 V nominal supply voltage and using the same data rate as for the IBM 130-nm case (3.125 Mbps). The total baseband power consumption in the 65-nm TSMC process after removing the JTAG test mode units and the shaping filter is expected to be roughly 370 μW (118 pJ/bit at 3.125 Mbps). The power consumption can be reduced even more by operating in the subthreshold regime desirable for medium throughputs (1-10 MHz) as explained in [64]. In subthreshold operation, the transistors are either kept off (nonconducting) or just short of conducting in the triode region (barely conducting). The relatively high on resistance of the barely conducting transistors will slow down the operation of logic gates and storage elements.

Assuming 4.5 mW of expected power consumption for the RF front end at TSMC's 65-nm technology and 370 μW for the baseband circuitry in TSMC's 65-nm process, the resulting transmitter circuit power consumption is 4.87 mW (1.56 nJ/bit at 3.125 Mbps). Note that the baseband power consumption for spread spectrum modulation is much less than the required power consumption for the RF front end circuitry, which is in the order of milliwatts. As calculated in Sec. 3.1.1, the energy required to transmit one bit from the transmit antenna to the receive antenna is $\sim$ 68 pJ/bit. Therefore the energy absorbed by the path loss is negligible compared to the energy required to drive the transmitter circuitry. Based on these numbers, the overall power consumption is expected to be above one milliwatt, which is the maximum wireless power that could be delivered safely to the implant [23]. This may necessitate a rechargeable battery or another powering scheme, such as ultrasound, for real-time powering.

4.2 Technology Scaling in the Subthreshold Regime

To further reduce the power consumption of the baseband transmitter, we can use the subthreshold regime for medium throughputs. It has been shown in [65] (Chapter 1) that we can save almost up to a factor of 15 in energy per operation by using a 0.3 V subthreshold supply voltage in place of the 1.3 V nominal voltage in 130 nm CMOS. To study the effects of technology scaling on the power consumption of subthreshold circuits, we have done a simple trend analysis on baseband circuit power consumption assuming subthreshold operation in different technology nodes. This analysis is based on a theoretical gate-level reconstruction of the baseband transmitter and is not intended to produce accurate numbers. However, it should clarify the approximate trends on how power consumption may be reduced by using smaller technology nodes in the subthreshold regime.

The system diagram of the proposed digital baseband circuit is shown in Fig. 4.1. This circuit does differential encoding and spreading of BPSK modulated signals. The main blocks of the circuit consist of one multiplexer and two shift registers. To reduce the power consumption of the circuit, a smaller technology node could be used. In addition to a reduction in the technology node, the circuit can be designed to operate in the subthreshold regime. This technology reduction should decrease the dynamic power consumption quadratically [64]. There is a trade-off between the dynamic power reduction, and the circuit speed. Smaller supply voltages lead to slower circuit speeds; however, as long as we are dealing with medium-throughput (1-10 Mbps), a subthreshold supply voltage might be suitable [64].

The energy consumption of the circuit in Fig. 4.1 can be theoretically analyzed to estimate the energy consumption decrease by using smaller technology nodes and subthreshold regime. This combination is usually called Ultra-Low Power (ULP) in literature [64]. The theoretical results can further be verified by simulation using SPICE.

To analyze the energy consumption, we describe the whole circuit at the gate level, i.e. using NAND, NOR, and inverter gates. For example the multiplexer is

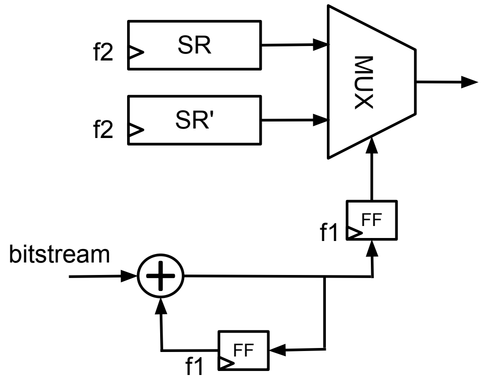

Figure 4.1: Circuit diagram of the baseband transmitter.

constructed of three NAND gates and one inverter gate. By continuing this process, we are able to find the total number of logic gates used in the circuit.

In order to calculate the dynamic power consumption, we only consider the dominant power dissipation factor, which are the switching capacitances, in comparison to other sources of dynamic power consumption, e.g. short circuit current, which happens when there is a slow rise/fall time and therefore both NMOS and PMOS are conducting at the same time. By switching capacitances, we mean the capacitances that switch between charge and discharge states to perform an operation. To find the switching capacitance for nominal voltages, one can use the Predictive Technology Models (PTM), which provide the capacitance of PMOS/NMOS in various sub-micron technology nodes [66]. In the subthreshold regime, the transistor capacitances change. This effect is explained in [64]. Then, we can use these transistor capacitance values to calculate the input capacitance of the inverter, NAND, and NOR gates. Without considering the throughput constraints yet, which introduce a practical barrier on the operating frequency, we can assume that the clock frequency equals the inverse of the circuit intrinsic delay. For loading, we can assume that all gates to have a capacitance loading approximately equivalent to a fan-out of four (FO4) inverter. This is a standard modeling approach in digital logic. By using these assumptions, we are able to calculate the energy consumption per operation, where by operation we mean the process of modulating and spreading one bit.

To calculate the static power consumption, we consider the dominant contributor, which is the subthreshold leakage current, and ignore other sources, e.g. gate leakage and junction leakage [64]. When a MOSFET's gate to source voltage (V_{gs}) is less than its threshold voltage V_t, it is said to be in subthreshold or weak inversion regime. When a V_{ds} voltage is applied in subthreshold regime, a diffusion current starts to appear. In case of off-state MOSFET ($V_{gs} = 0$), this subthreshold current acts as a leakage current and contributes to the static power consumption. When gate oxide is made thinner, the gate leakage increases due to tunneling. Junction leakage is due to reverse biased drain to substrate junction. In order to find out how many transistors are in the off-state on average, we need to do a statistical analysis for each logical gate's activity. To do so, we analyze each logic gate, i.e., NAND, NOR, and Inverter, and estimate the statistical probability of being off for each of the transistors. The average number of off transistors leads to the average amount of subthreshold leakage drawn from the supply voltage. The amount of the leakage current for PMOS/NMOS transistors in each technology node and at nominal voltages are calculated in [66]. For subthreshold supply voltages, we can use the transistor characterization from [64].

Adding the dynamic and static power consumption, we obtain the total power consumption of the circuit. By calculating the logic depth of the circuit, we can calculate the worst-case maximum delay of the circuit to perform an operation. By operation, we mean the process of differentially encoding a BPSK sequence and then spreading it by replacing each bit (0 or 1) with the chip sequence. Using the circuit delay and the power consumption, we arrive at the total energy consumption per operation, which is calculated in various technology nodes and supply voltages.

To do the analysis at the gate level, we need to better understand the behavior of gates in the subthreshold regime. In subthreshold operation, the intrinsic gate capacitance is lower than in the nominal operating regime. Therefore, by using the modified values of transistor parameters in the subthreshold regime [64], we are able to find the switching capacitance of each logic gate. Added to the internal switching capacitance, there is a capacitance at the output node of each gate. This capacitance, which is due partly to diffusion capacitance of the driving transistors but mostly due to the fan-out, adds to the amount of the capacitance switching at the output node of the logic gate. Based on the combined value of the internal switching capacitance and the output capacitance seen at the node, the dynamic power consumption can be evaluated for each logic gate. To calculate the static power consumption, we need to calculate the off-state leakage of each device in the subthreshold regime. When calculating the subthreshold current, we also consider the effects of the drain-induced barrier lowering (DIBL) and subthreshold swing [64]. In each logic gate, only some of the devices are off at a time. Therefore, we statically calculate how many of them are off at a time under certain assumptions of input signal probabilities. We also consider the effects of the width difference of PMOS and NMOS, due to the difference in mobility of holes versus electrons, in the final value for the leakage of each device.

By knowing the dynamic power consumption for each logic gate ($P_{dyn} = 0.5 \cdot \alpha \cdot C_{sw} \cdot V_{dd}^2 \cdot W_{eff} \cdot f$), the operating frequency, and also the statistical average of the static power consumption for each logic gate, we can estimate the dynamic power consumption of each cell, e.g. MUX and shift register. This produces a modular way of estimating the power. This way, we will be able to have a modular view of where in the circuit the power consumption is consumed the most.

4.2.1 Switching Capacitance of Logic Gates

In this section, we are going to discuss how to calculate the switching capacitance of the logic gates. As we can build all of the cells with NAND, NOR, and inverter logic gates, we are only going to analyze these three logic gates. This analysis includes both the internal and fan-out capacitances contributing to the total switching capacitance at the output node of each logic gate. The internal capacitances of a MOSFET are demonstrated as in Fig. 4.2.

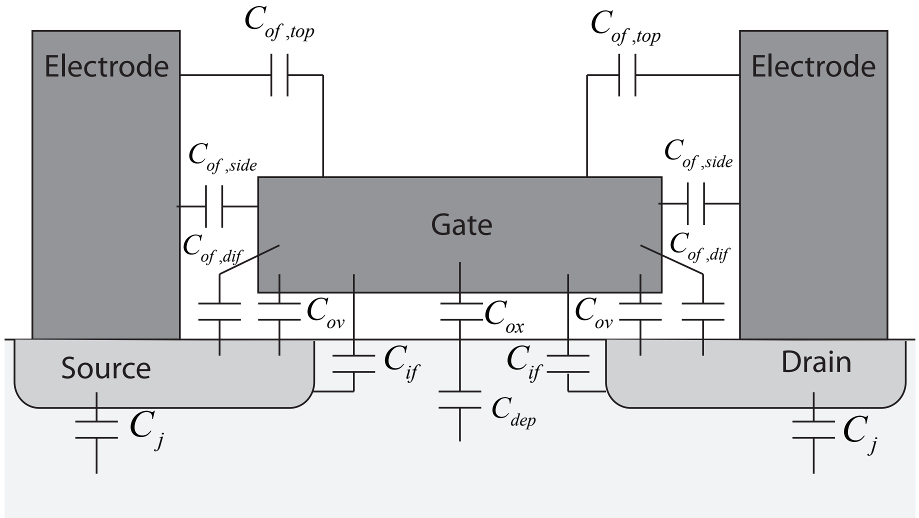

Figure 4.2: MOSFET capacitances in subthreshold regime [64].

FO4 Inverter Capacitance

In order to model all the internal capacitances, we assume a lumped capacitance model connected between the drain of the transistors and ground. This lumped capacitance model will serve as the total switching capacitance, including the internal and the loading capacitances.

We use the MOSFET-level capacitance values as shown in Fig. 4.3 to reach the FO4 inverter capacitance values. These values correspond to the internal capacitances demonstrated in Fig. 4.2. $C_{g,nom}$ is extracted from the PTM BSIM4 models, and it includes the oxide layer capacitance of $C_{ox} = \epsilon_{ox} L_{eff}/T_{ox}$. As T_{ox} scales almost in the same pattern as L_{eff} from 250 nm to 130 nm ([64]), not much change is expected due to the ratio L_{eff}/T_{ox} in this technology range. After shrinking below 90 nm technology, C_{ox} and therefore $C_{g,nom}$ start to decay faster than T_{ox} scaling, which scales more slowly due to manufacturing limitations. In the subthreshold regime, the depletion capacitance in series with C_{ox} is dominant by being smaller. This leads to a much smaller $C_{g,sub}$ compared to $C_{g,nom}$. As of this small $C_{g,sub}$, the effect of other small parasitic capacitances become significant. $C_{g,ext}$ includes the fringing and overlap parasitic capacitances, i.e. overlap capacitance (C_{ov}), inner fringing capacitance (C_{if}), and outer fringing capacitances ($C_{of,side}$, $C_{of,top}$, and

$C_{of,dif}$). In the calculation of $C_{g,ext}$, both the drain and source sides have been considered. The last capacitance considered is the junction capacitance (C_j), which is between drain and substrate and also between source and substrate.

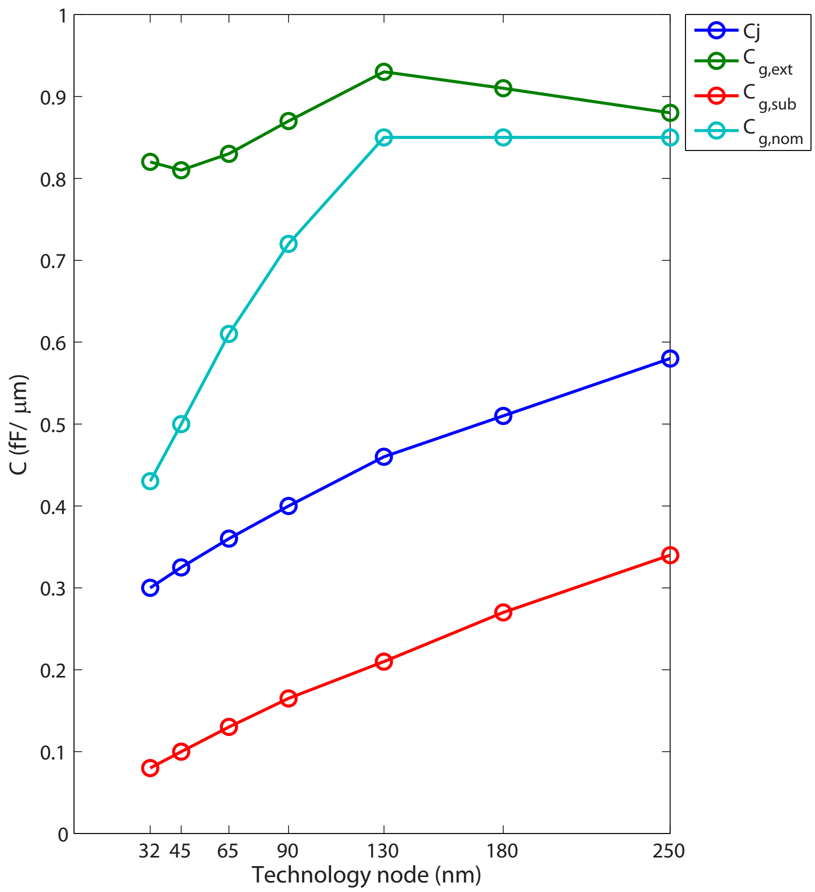

Figure 4.3: Internal capacitance values of a MOSFET [64].

Without considering the fanout yet, we take into account the effect of the capacitances connected to the drain. These capacitances contribute to the overall lumped capacitance model (sample FO1 inverter is shown in Fig. 4.4).

The capacitance $C_{g,ext}$ includes all fringing capacitances and overlap capacitances, i.e. C_{if}, C_{ov}. However, not all of the capacitances are connected to the drain. Only half of the $C_{g,ext}$ is connected to the drain (According to [64], the sum

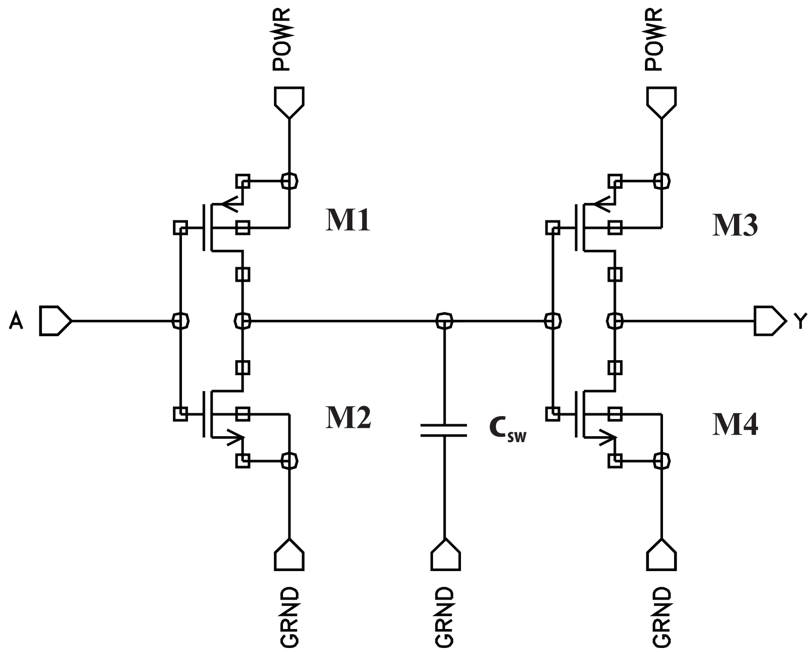

Figure 4.4: Inverter with one inverter connected to an output node. The lumped model switching capacitance is denoted by C_{sw}.

of both drain and source sides is considered in $C_{g,ext}$). This connection is between drain and gate, therefore we need to use the Miller theorem ([67]) to calculate the impact on the lumped capacitance model between drain and ground. Eq. 4.1 shows the effective amount of $C_{g,ext}$ on the C_{sw} for NMOS.

$$C_{g,ext,eff} = 0.5C_{g,ext}(1 - A) \tag{4.1}$$

where A is the gain and is equal to -1 for the inverter.

Capacitance C_j is connected between the drain and substrate and we assume that substrate is grounded. On the other hand, the capacitance $C_{g,sub}$ is connected between the gate and substrate and therefore has no impact on the C_{sw} model. The total capacitance for an inverter ignoring the fanout load is shown in Eq. 4.2.

$$C_{sw,withoutFO} = (C_{g,ext,eff} + C_j) \cdot (1 + NP) \tag{4.2}$$

where NP is the ratio of the PMOS gate width to the NMOS gate width. Because of the lower mobility of holes compared to electrons, the width of the PMOS transistor should be increased to give the same rise time as the fall time produced by the NMOS transistor. According to [64], the PMOS gate width is roughly three times the NMOS gate width (i.e., $NP = 3$).

To consider the fanout effect, we need to know what capacitances affect the lumped capacitance model, C_{sw}, from the load. In the case of an inverter as a load, the capacitances connected to the gate of the inverter load have an impact on C_{sw}. As before, we calculate the fanout capacitance for one NMOS in an inverter and then expand it to the overall inverter by the $(1 + NP)$ factor.

Half of the capacitance $C_{g,ext}$ is connected between the gate and source, and half is connected to the drain, for which Miller theorem can be used to calculate the amount of resulting capacitance between the gate and ground. Using these data, the effective $C_{g,ext}$ is shown in Eq. 4.3.

$$C_{g,ext,eff,F} = 0.5C_{g,ext} + 0.5C_{g,ext}(1 - A) \tag{4.3}$$

where the first term on the right side is the gate-source contribution and the second term is the gate-drain contribution.

Capacitance C_j lies across the drain and substrate or between the source and substrate; thus, it has no significance on the lumped capacitance C_{sw} model between the load's gate and ground. Capacitance $C_{g,sub}$ is between the gate and substrate, which is assumed to be grounded. Therefore, it contributes to the overall C_{sw}. The total capacitance due to the fanout capacitance is shown in Eq. 4.4.

$$C_{fanout} = FO \cdot (1 + NP) \cdot (C_{g,ext,eff,F} + C_{g,sub}) \tag{4.4}$$

where FO is the fanout number.

Using Eqs. 4.2 and 4.4, C_{sw} can be derived as shown in Eq. 4.5. This capacitance is depicted in Fig. 4.5 to better visualize the capacitance value of an FO4 inverter.

$$C_{sw} = (1+NP)\cdot\left[C_{g,ext}\Big(0.5(1-A)+FO\cdot(1-0.5A)\Big)+C_j+FO\cdot C_{g,sub}\right] \quad (4.5)$$

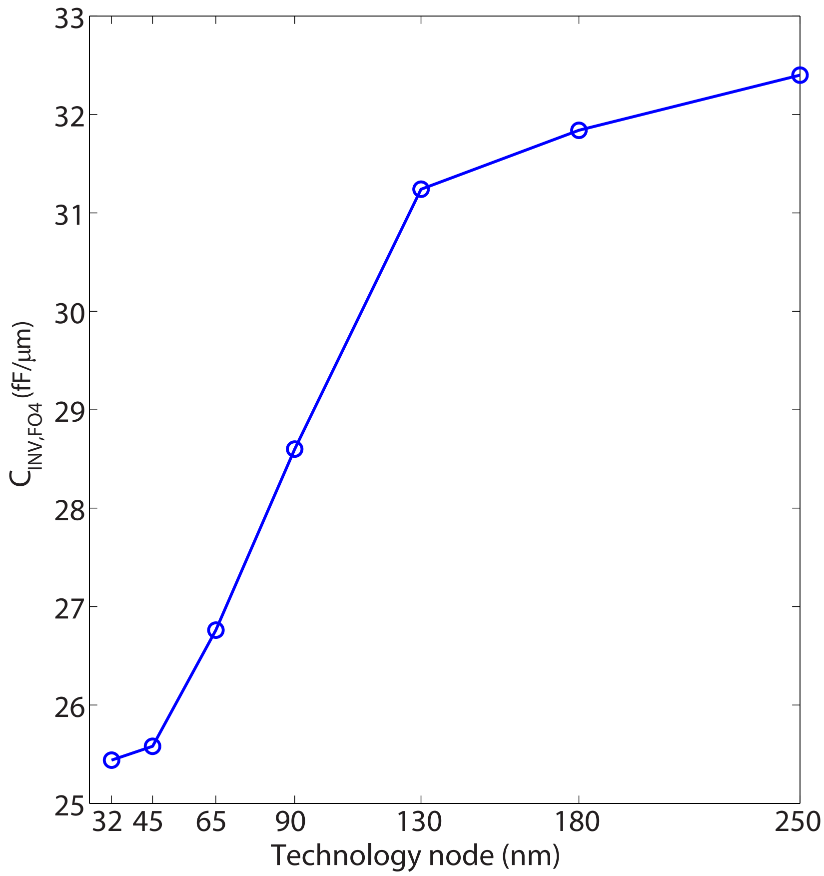

Figure 4.5: Switching capacitance of an FO4 inverter.

To verify the results, we can compare the C_{sw} value results in Eq. 4.5 with the values in Fig. 8 of [64]. From Fig. 4 of [64] for the 250 nm technology node, the capacitance values are roughly: $C_j = 0.59\ fF/\mu m$ and $C_{g,sub} = 0.35\ fF/\mu m$, and $C_{g,ext} = 0.9\ fF/\mu m$. Substituting these values into Eq. 4.5, we will end up with $C_{sw} = 33.16\ fF/\mu m$. As shown in Fig. 8 of [64], the final value is approximately $C_{sw} = 30\ fF/\mu m$. This small difference between results could be because of the limited accuracy of values read from figures or the approximations made to calculate the final capacitance.

NAND and NOR Capacitance

Each conventional n-input NAND or NOR logic gate is built from n complementary transistor pairs, as shown in Fig. 4.6. The capacitance of each complementary transistor pair is assumed to be approximately equal to a transmission gate capacitance (C_p) [68]. For now, we will assume the pair's capacitance to be approximately equal to an inverter capacitance. Although this is not something usual in literature, it should give a correct power consumption trend. As a future work, we may need some modifications to include the transmission gate capacitance for further accurate results.

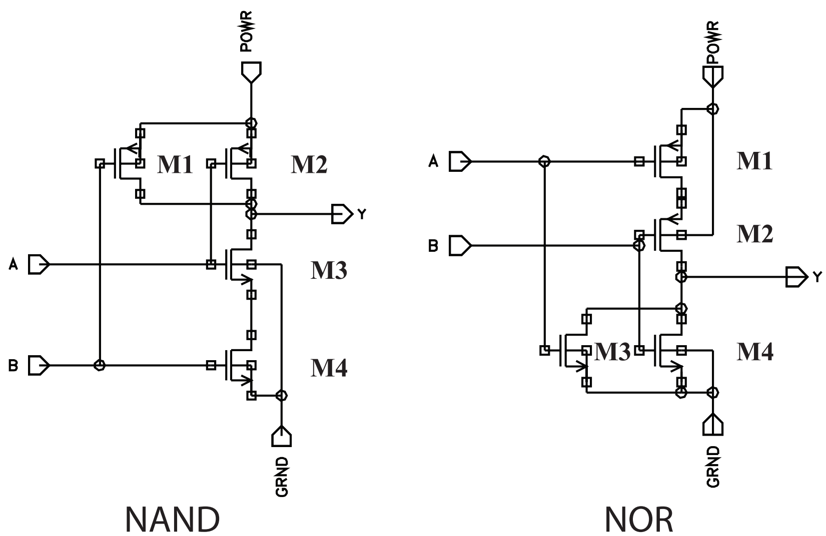

Figure 4.6: Two input NAND and NOR gates.

With the approximation presented in [68], we can estimate the switching capacitance of the NAND or NOR logic gates according to the number of the transistor pairs inside. The number of transistor pairs (PMOS/NMOS) is equal to the number of gate inputs. Therefore, the estimated switching capacitance due to the logic gate itself is nC_p, where n is the number of inputs and C_p is the pair capacitance value. The total switching capacitance at the output node also includes the capacitance due the following loading logic gates. Thus, the total switching capacitance of a NAND or NOR gate is as in Eq. 4.6.

$$C_{sw} = nC_p + C_{FO} \tag{4.6}$$

where C_{sw} is the total switching capacitance in the output node of NAND or NOR gate, n is the number of inputs or number of pairs, C_p is the transistor pair model capacitance value, and C_{FO} is the amount of capacitance due to loading logic gates, which contributes to the total switching capacitance at the output node.

As described before, we use the inverter switching capacitance as an approximation for the transmission gate capacitance for now. Therefore, C_p is approximated as

$$C_p = [0.5C_{g,ext}(1 - A) + C_j] \cdot (1 + \mathrm{NP}) \tag{4.7}$$

where $C_{g,ext}$ is the sum of all fringing and overlap capacitances in an NMOS transistor, which includes both drain and source contributions; A is the inverter's gain, which is -1; C_j is the junction capacitance of an NMOS transistor; and NP is the ratio of the PMOS gate width to the NMOS gate width.

About the fan-out capacitance, we assume that all logic gates have a loading equal to a FO4 inverter. The FO4 inverter loading capacitance is shown in Eq. 4.4. Later on, we may need to improve this assumption by digging into the correct amount of the average loading capacitance for each logic gate.

4.2.2 Activity Factor

The output switching factors of the gates are based on knowing the switching probability of the inputs. For example, for AND, OR, and XOR gates, the output node switching probabilities are as in Eq. 4.8 ([69] and [70]).

$$p_{AND} = (1 - p_A p_B) p_A p_B \tag{4.8a}$$

$$p_{OR} = (1 - p_A)(1 - p_B)(1 - (1 - p_A)(1 - p_B)) \tag{4.8b}$$

$$p_{XOR} = (1 - (p_A + p_B - 2p_A p_B))(p_A + p_B - 2p_A p_B) \tag{4.8c}$$

where p_A and p_B are switching probabilities of inputs A and B, respectively.

To correctly calculate the switching factor for all the logic gates, we need to start from the inputs and propagate signal probabilities through the outputs. Just as in Eq. 4.8, we can calculate the output switching probability by knowing the input switching probabilities. However, this process becomes challenging for large circuits. If we do not mind calculating the switching factors for all the gates of the current circuit design, still there is a major challenge left. In calculating the previous probabilities, we assumed that all the input signals of the logic gates are statistically independent. However, this is not always the case. For example, the output switching of the NAND gate in Fig. 4.7 cannot be calculated using the conventional probability formulas assuming signal independence because the inputs of the gate are logically dependent in this case. If the inputs were independent, the output probability would be: $p_{OUT} = 1 - (1 - p_A)p_A$. However, in this case the output is always one and therefore the switching probability is actually zero [69].

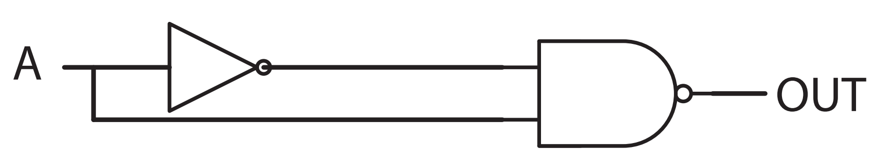

Figure 4.7: NAND gate with statistically dependent input signals.

Based on the challenges of calculating the switching factor at each logic gate node, we use an upper bound for the switching factor value to obtain an upper bound on energy consumption.

4.2.3 Leakage Current

To calculate the static power consumption at the gate level, we need to know how much leakage current flows through each logic gate. To obtain this, we need to first look at the device-level leakage in the subthreshold regime.

Subthreshold Leakage Current of a MOSFET

In nanometer MOSFETs, there are three main leakage components, which contribute to the final leakage current: subthreshold, gate, and junction leakage. These leakages have been described in previous sections and their are plotted in Fig. 1.4 of [65]. As subthreshold leakage is the dominant factor, we count it as the dominant component and neglect the other small components [64, 71]. The subthreshold region is where $V_{gs} < V_{dd}$, which is also called weak inversion. The subthreshold current can be evaluated as shown in [64, 71]

$$I_{sub} = W_{eff} \cdot I_0 \cdot 10^{\left(\frac{V_{gs}+\eta V_{ds}}{S}\right)} \left(1 - e^{\left(-\frac{V_{ds}}{U_{th}}\right)}\right) \tag{4.9}$$

where I_0 is the subthreshold reference current ($I_0 = I_{OFF,nom} 10^{\frac{-\eta V_{dd,nom}}{S}}$), S is the subthreshold swing, η is the DIBL factor, and U_{th} is the thermal voltage of around 26 mV at room temperature. The S and η parameters are plotted in Fig. 4.8 versus the technology node from 250 nm to 32 nm.

In static CMOS logic, we consider the off state to be when $V_{gs} = 0$ and $V_{ds} = V_{dd}$. Using these considerations, parameters provided, and also Eq. 4.9, we end up with the subthreshold leakage currents as shown in Fig. 4.9 for one NMOS. As seen in this figure, the subthreshold current increases as the minimum linewidth of the technology shrinks. In smaller technologies; however, the increase in the subthreshold current becomes smaller. Independent of the technology, the subthreshold current always decreases with smaller supply voltages.

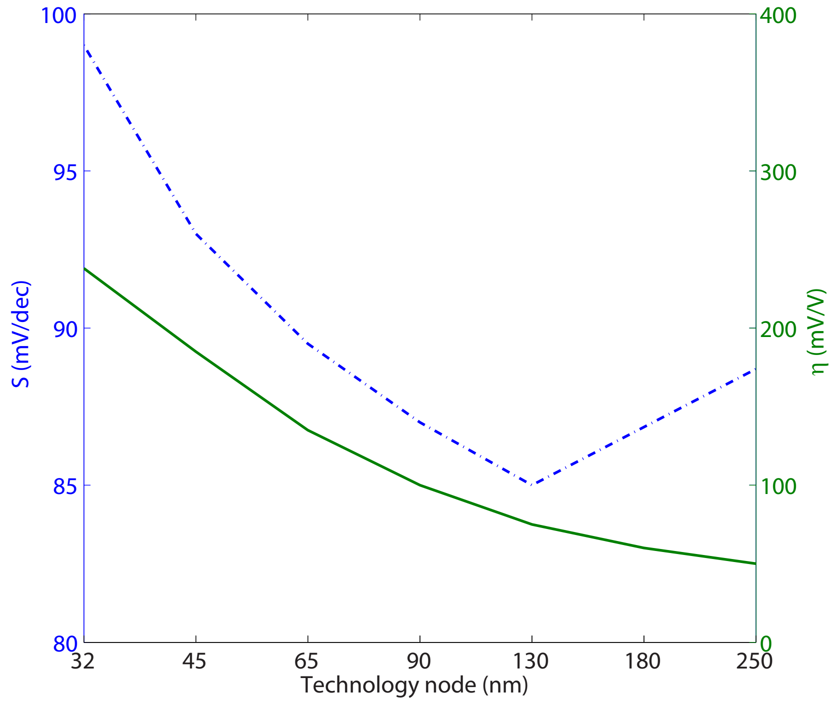

Figure 4.8: Subthreshold swing S (solid line style) and DIBL coefficient (η - dotted line style) [64].

Gate-level Subthreshold Leakage Current

While a logic gate is switching at some definite frequency, the complementary transistors change between the on and off states to perform the required task (We only assume fully powered and active operation of the circuit for now, and ignore the possibility of sleep modes for the moment). Not all the transistors are on at a time; therefore there is leakage current going through each off device. We can analyze the pattern of switching of the devices in each gate, and based on this pattern estimate a statistical average of the leakage current contributed by each gate.

As shown in Fig. 4.10, each of the transistors of the inverter, 2-input NAND, or NOR logic gates have an average of 0.5 off probability. This conclusion is based on assumption of equal input signal probabilities. For a greater number of inputs, e.g. 3-input NAND, it can be shown that we still have the same 0.5 off probability for each device in the logic gate, under the assumption of equal input signal probabilities. Based on this result, we can say that the leakage currents for each logic gate can be

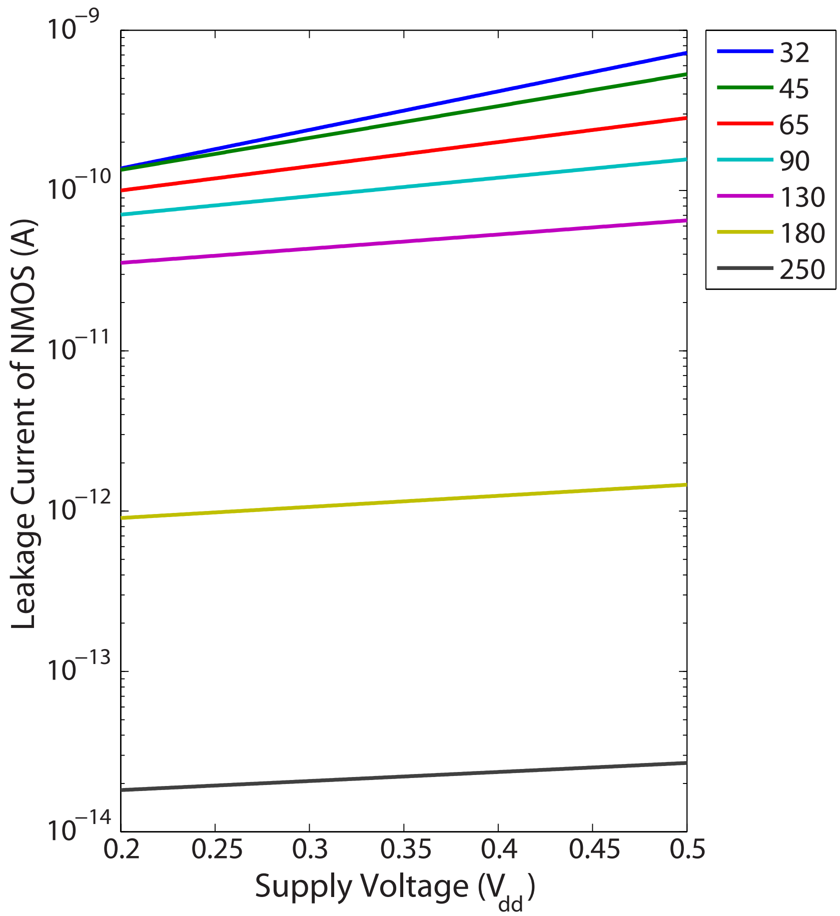

Figure 4.9: Subthreshold current of one NMOS assuming $V_{gs} = 0$ and $V_{ds} = V_{dd}$. Legend has technology nodes in nm.

calculated as in Eq. 4.10.

$$I_{INV} = 0.5 \cdot I_{leak,NMOS} \cdot (1 + \mathrm{NP}) \tag{4.10}$$

$$I_{NAND,MX1} = 0.5 \cdot I_{leak,NMOS} \cdot M \cdot (1 + \mathrm{NP})$$

$$I_{NOR,MX1} = 0.5 \cdot I_{leak,NMOS} \cdot M \cdot (1 + \mathrm{NP})$$

where $I_{leak,NMOS}$ is the leakage current of one NMOS described in Sec. 4.2.3, M is the number of inputs for the corresponding logic gate, NP is the ratio of the gate width of the PMOS transistors over the NMOS transistors.

Based on Eq. 4.10, we can calculate the leakage current of each logic gate described. As an example, the leakage current of an inverter is shown in Fig. 4.11.

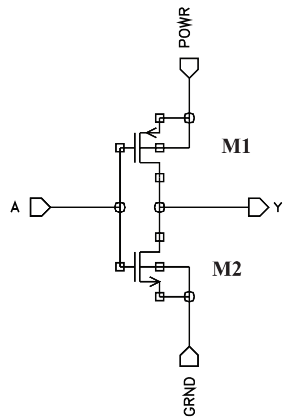

A	M1	M2	OUT
HIGH	OFF	ON	LOW
LOW	ON	OFF	HIGH

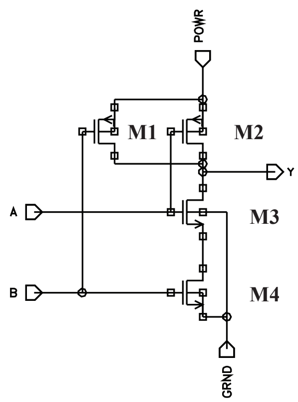

A	B	M1	M2	M3	M4	OUT
HIGH	HIGH	OFF	OFF	ON	ON	LOW
HIGH	LOW	ON	OFF	ON	OFF	HIGH
LOW	HIGH	OFF	ON	OFF	ON	HIGH
LOW	LOW	ON	ON	OFF	OFF	HIGH

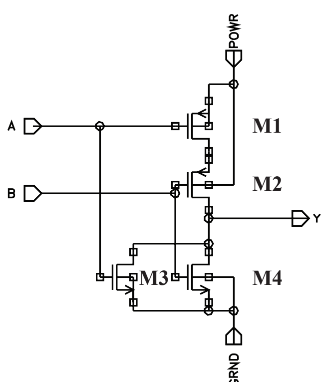

A	B	M1	M2	M3	M4	OUT
HIGH	HIGH	OFF	OFF	ON	ON	LOW
HIGH	LOW	OFF	ON	ON	OFF	LOW
LOW	HIGH	ON	OFF	OFF	ON	LOW
LOW	LOW	ON	ON	OFF	OFF	HIGH

Figure 4.10: State of each device in the inverter, NAND, and NOR gates during logical operations.

The trend of the change in the leakage current is pretty much the same as in Fig. 4.9 for an NMOS transistor.

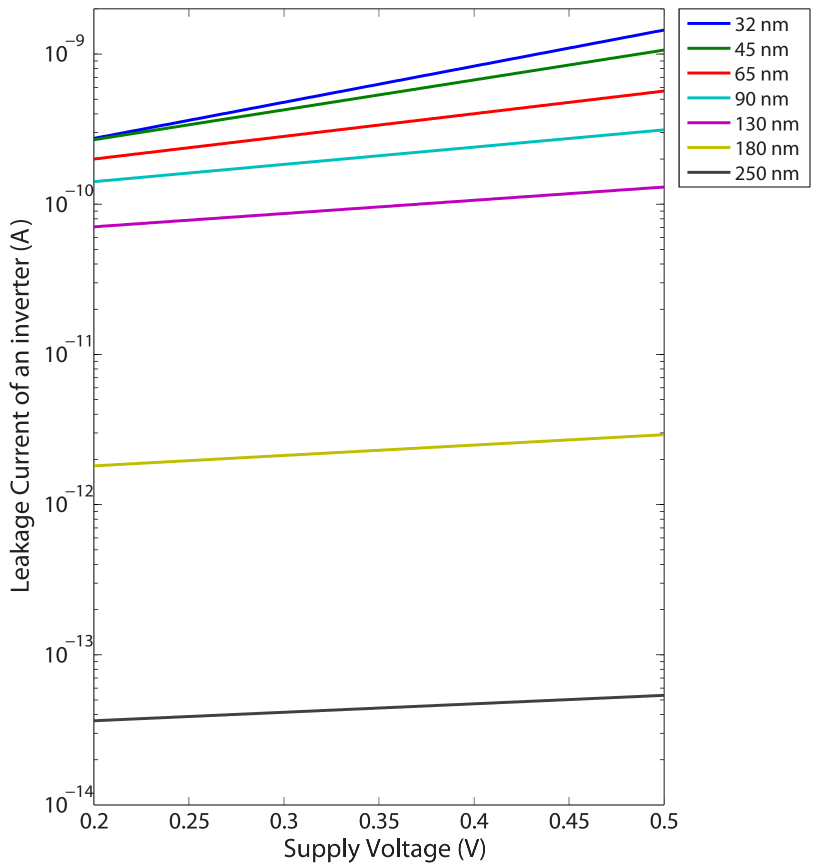

Figure 4.11: Inverter leakage current calculated assuming that NP = 3.

4.2.4 Power Consumption

To calculate the power consumption of each logic gate, we consider the output switching capacitance of the logic gate to calculate the dynamic power consumption and the leakage current for the static power consumption. By having the power consumption for each logic gate, we can proceed to the next level and calculate the power consumption of each cell. By cell we mean the main building blocks of the circuit, which are shift registers, flip-flops, multiplexers, and some logic gates. Some of these cells might use cells of other types as building blocks.

Power Consumption of Logic Gates

To calculate the power consumption of the logic gates we need data from the transistor-level analysis. These data include the switching capacitance of the logic gates and the effective width of the transistors. The effective width of the transistors is assumed to be approximately equal to 1.5 times the effective channel length ($W_{eff} = 1.5L_{eff}$) [64]. The values of L_{eff} for different technology nodes from 250 nm to 32 nm are shown in [64].

To calculate the dynamic power consumption of the inverter, NAND, and NOR logic gates, we use the power consumption formula in Eq. 4.11. Each logic gate has its own specific switching capacitance, as discussed in Sec. 4.2.1. Moreover, based on the different places in the circuit, the logic gates may be in different conditions in terms of frequency and switching factor. The supply voltage and the effective gate width are chosen by the designer and can be adjusted according to the purpose.

$$P_{dyn} = \frac{1}{2} \cdot \alpha \cdot C_{sw} \cdot V_{dd}^2 \cdot W_{eff} \cdot f \tag{4.11}$$

where α is the switching factor, C_{sw} is the switching capacitance of the gate including the loading effects, V_{dd} is the supply voltage, W_{eff} is the effective gate width of the NMOS transistor, and f is the operating frequency.

The static power consumption of each logic gate is determined by the leakage current of its off transistors. As in Fig. 4.10, the transistors of a logic gate transition from the on and off states to perform certain logical operations. As not all of the devices are off at a time, we estimated the average off time of each device in a logic gate in order to know how much leakage current is drawn from supply voltage by a logic gate (I_{leak}). Once we have this amount of leakage, we can model the logic gate as a constant impedance connected to a supply voltage. Therefore, the static power consumption in active period can be calculated as in Eq. 4.12.

$$P_{stat} = V_{dd} \cdot I_{leak} \tag{4.12}$$

Power Consumption of the Cells

Each cell can be constructed using the basic NAND, NOR, and inverter logic gates. Based on this fact and also on the power consumption of each logic gate described in Sec. 4.2.4, we can estimate the entire power consumption of each cell.

Multiplexer As shown in Fig. 4.12, a 2-to-1 multiplexer consists of three NAND gates and one inverter. Therefore, the total power consumption of this cell is the sum of the power consumption of the component logic gates. The multiplexer in the baseband circuit works at the f_2 chip operating frequency, which is sixteen times the f_1 bit frequency (for a processing gain of 16). Concerning the loading capacitance, we assume a loading equal to the loading of an FO4 inverter for all the logic gates. We will later improve this assumption.

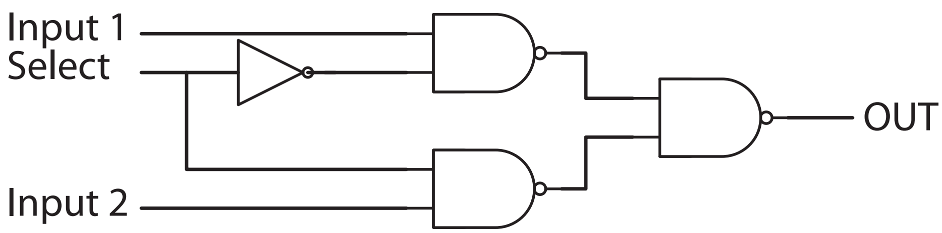

Figure 4.12: 2-to-1 multiplexer.

Positive-Edge-Triggered D Flip-Flop The positive-edge-triggered flip-flop, without the set and reset pins, consists of six NAND gates as shown in Fig. 4.13. The flip-flops used in the baseband circuit design have different operation frequencies depending on where they are used in the design. In the shift register, the flip-flops use the f_2 clock, but in the differential encoder and the connection to the multiplexer, they use the f_1 clock.

Shift Register The most power-hungry cell is the shift register. The parallel-in serial-out (PISO) register used in the design, without set and reset functionality, includes one inverter, $3(n-1)$ NAND gates, and n flip-flops, where n is the number of the bits in the shift register. In our specific design, the number bits in the shift register is sixteen ($n = 16$). The shift registers of the circuit work with the faster f_2

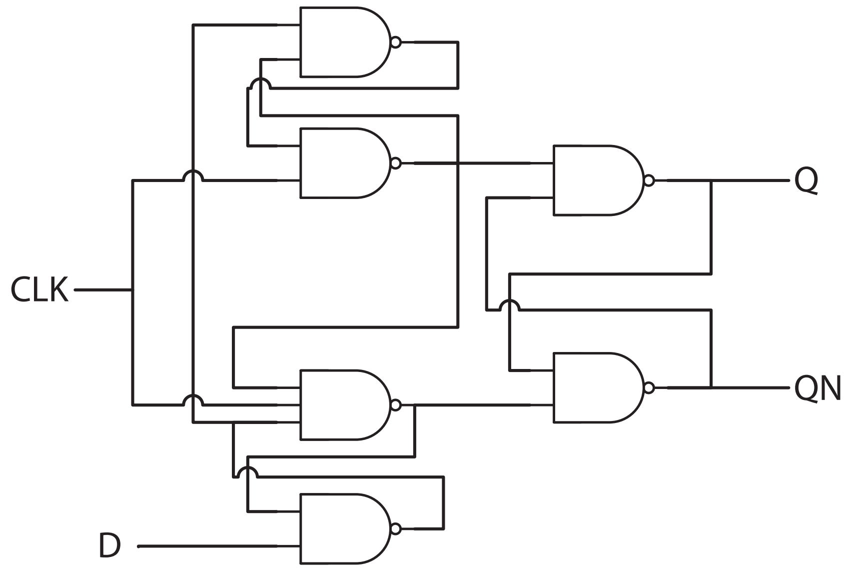

Figure 4.13: Positive-edge-triggered D flip-flop.

chip clock signal and their total energy equal the cumulative power of their building blocks. A four-bit shift register is shown in Fig. 4.14 as an example.

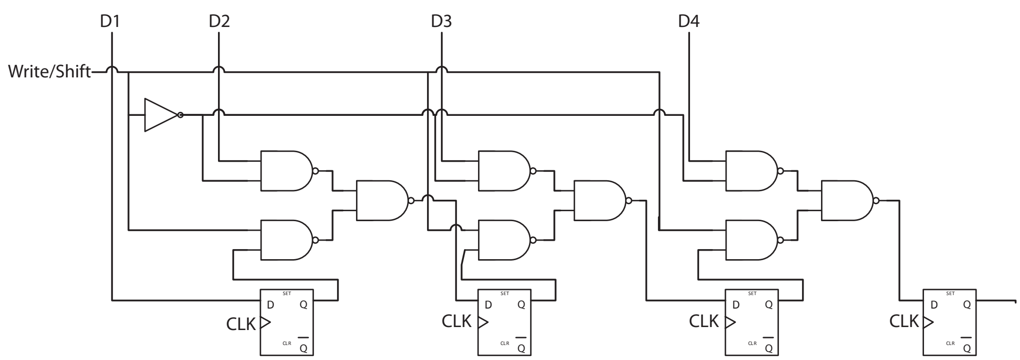

Figure 4.14: 4-bit non-circular shift register.

XOR An XOR logic gate can be constructed using four NAND gates, as shown in Fig. 4.15. The operating frequency of the NAND gate is assumed to be the bit clock f_1 for this power analysis.

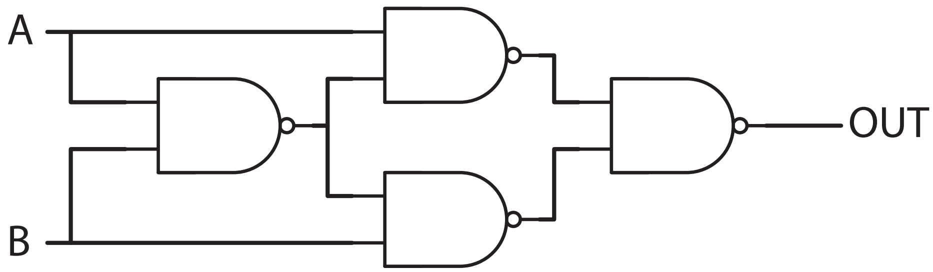

Figure 4.15: XOR logic gate.

Power Trend Plots

To calculate the power consumption in the subthreshold regime, we have assumed the bit frequency f_1 to be sixteen times smaller than the chip frequency f_2 ($f_1 = f_2/16$). Loading capacitances for gates are approximated to be equal to the FO4 inverter capacitive, or in some cases more or less than the FO4 inverter capacitance loadings, based on the gate location. Although not always in the subthreshold regime, we consider the V_{dd} to be in the range of 0.2 V to 0.5 V. The threshold voltages of the 32 nm, 45 nm, 65 nm, 90 nm, 130 nm, 180 nm and 250 nm technologies are 0.27 V, 0.27 V, 0.3 V, 0.32 V, 0.36 V, 0.49 V and 0.63 V, respectively. We also assume that the switching factor of 0.5 represents an upper bound. The transistor data in subthreshold supply voltages is used from the data [64]. The energy consumption of the circuit in different technologies and subthreshold supply voltages is demonstrated in Fig. 4.16. As it is demonstrated in this figure, in smaller technologies the effect of subthreshold current cannot be neglected. In smaller supply voltages the increased static energy consumption increases the total energy consumption per operation. This trend leads to a sweet spot in terms of the optimal supply voltage. For example, in case of using 65 nm technology the optimal voltage for subthreshold energy consumption is between 0.2 V and 0.3 V. This optimal voltage is also confirmed through our collaborator from Lund University, who have calculated approximately 0.24 V for the optimal voltage through their standard cell simulator. The details of Lund University researchers' work can be found in [72]. To further verify our results, we can compare the calculated energy consumptions with multiplier energy consumption calculated in [64]. As the calibration curves in Fig. 4.17 show for the 65 nm technology our calculated numbers are approximately linearly aligned by the results in [64].

In Fig. 4.18 the total power consumption of the baseband transmitter is plotted assuming that $f_2 = 5$ MHz and $V_{dd} = 0.5$ V. If we operate at this frequency, the static power consumption becomes more significant at smaller technology nodes. This relative increase in the static power consumption increases the total power a bit in 45-nm technology. Working at $f_2 = 5$ MHz and with the present assumptions to calculate the final power, we determine that using smaller technologies, such as 32 nm, does not necessarily gain us much in terms of power consumption. The low-power sweet spot thus seems to be 65 nm technology given the present knowledge and expertise. This conclusion is further confirmed by Lund University collaborator. To make smaller technologies more feasible, it is necessary to invent and utilize methods to reduce the subthreshold current and therefore the overall static power consumption.

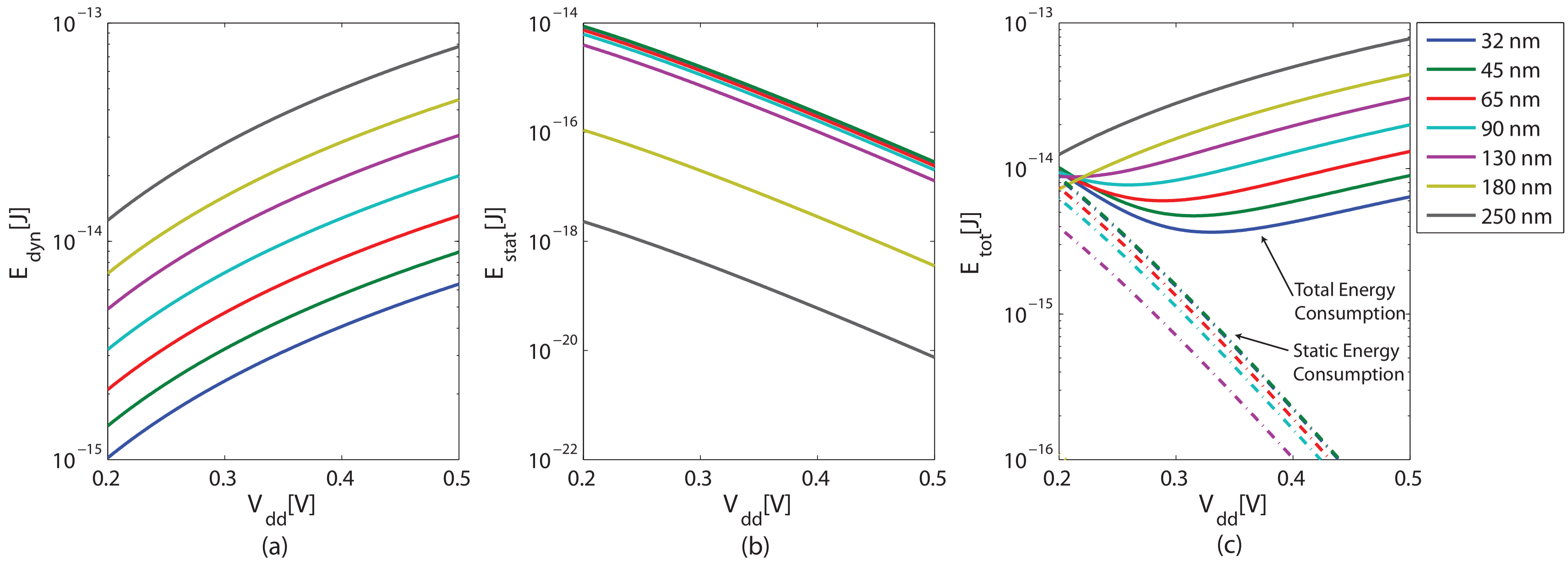

Figure 4.16: Energy consumption of the baseband transmitter circuit assuming capacitive loading: (a) Dynamic energy consumption; (b) Static energy consumption; (c) Total energy consumption is plotted in solid line style and static energy consumption is plotted in the same figure in dotted line style.

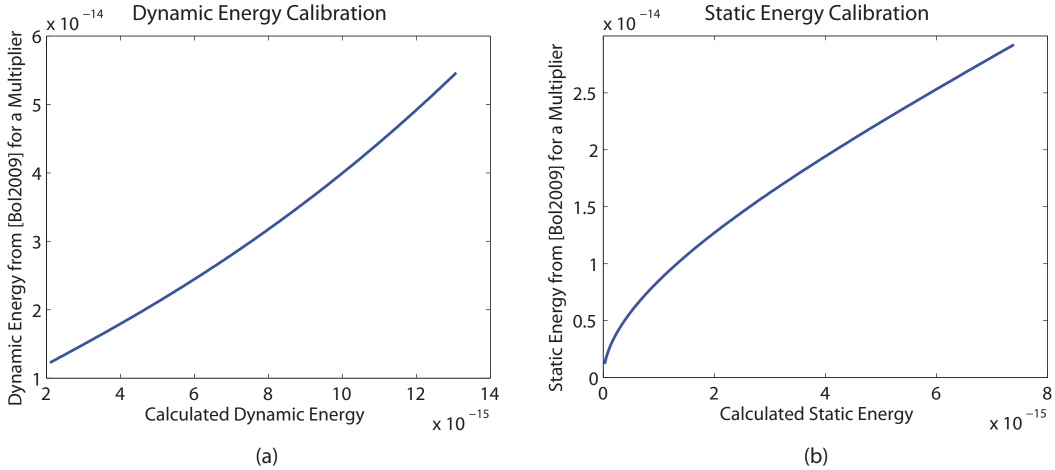

Figure 4.17: Calibration curves for the calculated energy results: (a) Dynamic energy consumption, (b) Static energy consumption.

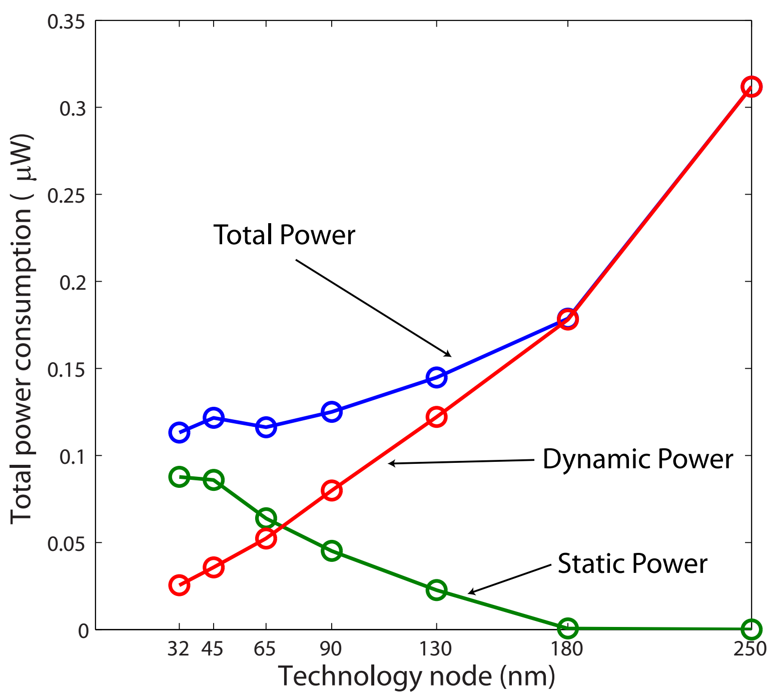

Figure 4.18: Power consumption of the baseband transmitter circuit in $V_{dd} = 5$ V with approximative capacitive loading for each logic gate and $f_2 = 5$ MHz.

Chapter 5

Conclusions

In this thesis, we investigated the problem of constructing a link budget for loop antennas that are capable of wireless data transmission to devices that are implanted in biological tissues. We focused primarily on a near-field communications scenario but we also briefly considered the far-field link budget problem. From several different perspectives, near-field communications is preferred over far-field communications because of lower path loss and because of greater compatibility with surrounding biological tissues. To transmit one bit over the near-field uplink or downlink in the recommended 2.4-GHz ISM band, $\sim$68 pJ/bit of energy is required using spread spectrum modulation, when one considers the predicted link losses and gains.

The power consumption of the implanted baseband communications circuitry was estimated for TSMC's 65-nm technology using the Synopsys Design Compiler tool and the results were compared to previous results in IBM's 130-nm technology. The effect of using the ultra low power subthreshold operation in different technology nodes was also analyzed using a generic design for the baseband transmitter. We confirmed our working assumption that the dominant power consumption in a typical spread spectrum high data rate implantable transmitter is due to the RF front end. According to the analysis, the transmitter circuitry cannot be safely powered in continuous operation using the described inductive links as the required operation power would exceed SAR-safe inductive power transfer limits. This may necessitate a rechargeable battery to boost the power that would be provided by wireless power transfer.

The expected power consumption of the RF front end at TSMC's 65-nm technology is approximately 4.5 mW (as reported by our collaborator in Washington State University). Assuming a data rate of 3.125 Mbps, the RF front end's energy consumption per bit is 1.44 nJ/bit. The expected power consumption of the baseband section with TSMC's 65-nm technology and at a nominal voltage is 370 μW (118 pJ/bit at 3.125 Mbps). According to our calculations the link losses are predicted to be 68 pJ/bit. Using these numbers we plotted a pie chart in Fig. 5.1 that compares the energy requirements of the different modules. As we can see, the most energy is consumed in the RF front end module. Therefore, in order to reduce the overall energy consumption drastically, more research should be done to reduce the energy consumption in the RF front end.

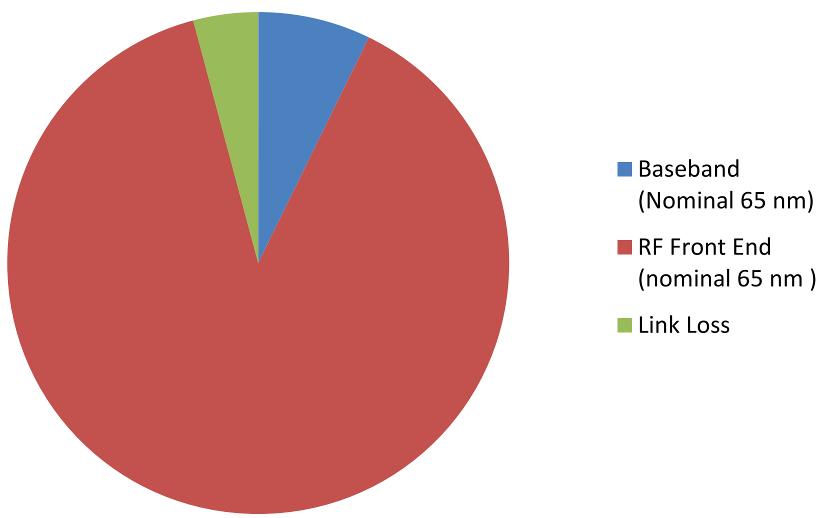

Figure 5.1: Comparison of energy consumption in different modules of an implantable transmitter.

In summary, the main contributions of this thesis were:

- Thorough literature review and analysis of published communication and powering configurations for the purpose of implantable electronics.

- Detailed consideration of candidate methods to communicate with devices implanted in biological tissues. The discussion included both wired and wireless (optical or RF) methods. This analysis led to the selection of near-field wireless communications.

- Selection of the most appropriate band for high data rate communications with an implantable device: Based on the knowledge of the optimal frequency for energy transfer in biological tissues, bandwidth requirements and regulatory policies, we chose the 2.4-GHz ISM band.

- Link budget analysis for nearfield communications between an implanted neural recording sensor and an external control device using spread spectrum technique in 2.4-GHz ISM band: The link budget is theoretically constructed based on the knowledge of the required signal-to-noise ratio for packet-based spread spectrum transmission and appropriate tissue losses and margins from literature. Using the link budget, the required transmit power and the energy required to transmit a bit using DSSS technique was calculated.

- Nominal power estimation of the baseband communications circuitry using Synopsys tools in IBM's 130-nm process and TSMC's 65-nm process was done to understand how much transistor scaling can affect the nominal power consumption. Added to this, the power effect of removing pulse-shaping filter and testing units in the next versions of the IC was simulated. Using the baseband power consumption results and the expected power consumption of the RF front end, the continuous powering feasibility in the near-field scenario was discussed using the maximum SAR-safe power transfer value from the literature.

- Power trend analysis in smaller technologies and in the subthreshold regime to understand how much power we could potentially save in communications circuitry. Added to the power reduction due to smaller technology nodes, the power consumption could be further reduced by using subthreshold voltages. For example, we could save energy per operation by up to 95% using subthreshold voltages in 130 nm standard bulk CMOS technology [65]. However, this reduction in energy per operation comes at the price of slower circuit speed.

As required by our application needs, detailed in the Introduction section, the proposed near-field communications accommodates a few centimeters of implantation depth. The choice of the 2.4-GHz ISM band provides enough bandwidth for high data rate communications. By constructing the link budget, the effect of different factors on the high data rate near-field communications was analyzed. Loops used in the near-field communications are less detuned by the presence of surrounding tissues [28] and they can also be used for transferring energy on the same link. Using higher frequencies than the conventional near field frequencies leads to smaller required loops for the transmitter and the receiver, which increases the suitability for implantation. The spread spectrum technique chosen gives immunity against the interference from other transmitters in the same 2.4-GHz ISM frequency band. It also gives the capability to add extra sensors transmitting to the same receiver at the same time.

To compare the suggested path to what has been reported in the literature, the inductive data and power links, as listed in Table 2.2, use lower frequencies and are therefore larger in size and lower in data rate. Using higher frequencies gives the advantage of smaller coils and higher data rates. The implantable far-field systems in Table 2.3 lack implantation depth advantage (a few cm) and if implanted deeply they are expected to have much deteriorated performance in terms of data rates with the same transmit power. The effect of other transmitters in the congested 2.4-GHz ISM band is not previously discussed and no system is used to mitigate interference. While using near-field communications reduces the range of communications, it decreases the path loss in biological tissues compared to far-field transmission. Using loop antennas and spread spectrum technique increases the immunity against other transmitters in the same 2.4-GHz ISM band. As discussed before, magnetic antennas are also less detuned in biological tissues compared to electric antennas.

5.1 Recommendations for Future Work

As discussed in the thesis, the power consumption of the RF front end is dominant and detailed optimizations of the baseband sections are not going to lead to significant improvements. Rather, the effort should be placed on the methods to reduce the power consumption of the RF stages, such as control or compression methods to lead to minimized on time for the RF front end. The RF stages should be reviewed to see how fast and efficiently (power-wise) they can be turned on and off since this has implications on optimal data packet sizing.

Based on our calculations and the assumptions that we took into account, we recommend using the 2.4-GHz ISM band in a near-field transmission scenario in order to achieve high data rate communications with the implanted device.

To reduce power consumption of the communications circuitry by scaling the technology size, technology nodes smaller than 65 nm are not necessarily required. This is because leakage currents may become significant in smaller technologies. For 65-nm technology; however, more design kits are available and lower fabrication costs are needed compared to smaller technology nodes. Therefore, the 65 nm technology node appears to be a good choice for immediate future fabrication.

According to the overall estimated power consumption of the implantable transmitter, a battery is required to boost the power as the SAR-safe RF power harvested is not enough to independently power the high data rate circuitry.

Bibliography

[1] Project SMART (Sensory Motor Adaptive Rehabilitation Technology). [Online]. Available: http://smartneuralprostheses.med.ualberta.ca/

[2] N. Canada. Brain facts. [Online]. Available: http://braincanada.ca/files/NeuroScience_Canada_Brain_Facts.pdf

[3] C. A. Balanis, *Antenna Theory: Analysis and Design*, 3rd ed. John Wiley and Sons, Inc., 2005.

[4] D. Cheng, *Field and Wave Electromagnetics.* Addison-Wesley, 1989.

[5] P. Li and R. Bashirullah, "A Wireless Power Interface for Rechargeable Battery Operated Medical Implants," *IEEE Trans. Circuits Syst. II: Express Briefs*, vol. 54, no. 10, pp. 912–916, 2007.

[6] S. Lee, H. Lee, M. Kiani, U. Jow, and M. Ghovanloo, "An Inductively Powered Scalable 32-channel Wireless Neural Recording System-on-a-Chip for Neuroscience Applications," *IEEE Trans. Biomed. Circuits Syst.*, vol. 4, no. 6, pp. 360–371, 2010.

[7] Y.-K. Song, W. Patterson, C. Bull, D. Borton, Y. Li, A. Nurmikko, and J. Simeral, "A Brain Implantable Microsystem with Hybrid RF/IR Telemetry for Advanced Neuroengineering Applications," in *Engineering in Medicine and Biology Society, 2007. EMBS 2007. 29th Annual International Conference of the IEEE*, 2007, pp. 445–448.

[8] M. Kiani and M. Ghovanloo, "An RFID-Based Closed-Loop Wireless Power Transmission System for Biomedical Applications," *IEEE Trans. Circuits Syst. II: Express Briefs*, vol. 57, no. 4, pp. 260–264, 2010.

[9] S. Kim, K. Zoschke, M. Klein, D. Black, K. Buschick, M. Toepper, P. Tathireddy, R. Harrison, H. Oppermann, and F. Solzbacher, "Switchable Polymer-Based Thin Film Coils as a Power Module for Wireless Neural Interfaces," *Sensors and Actuators A: Physical*, vol. 136, no. 1, pp. 467–474, 2007. [Online]. Available: http://linkinghub.elsevier.com/retrieve/pii/S0924424706006856

[10] A. K. RamRakhyani, S. Mirabbasi, and M. Chiao, "Design and Optimization of Resonance-Based Efficient Wireless Power Delivery Systems for Biomedical Implants," *IEEE Trans. Biomed. Circuits Syst.*, vol. 5, no. 1, pp. 48–63, 2011.

[11] M. Ghovanloo and K. Najafi, "A Wideband Frequency-Shift Keying Wireless Link for Inductively Powered Biomedical Implants," *IEEE Trans. Circuits Syst. II: Regular Papers*, vol. 51, no. 12, pp. 2374–2383, 2004.

[12] A. Sodagar, K. Wise, and K. Najafi, "A Wireless Implantable Microsystem for Multichannel Neural Recording," *IEEE Trans. Microw. Theory Tech.*, vol. 57, no. 10, pp. 2565–2573, 2009.

[13] R. R. Harrison, P. T. Watkins, R. J. Kier, R. O. Lovejoy, D. J. Black, B. Greger, and F. Solzbacher, "A Low-Power Integrated Circuit for a Wireless 100-Electrode Neural Recording System," *IEEE J. Solid-State Circuits*, vol. 42, no. 1, pp. 123 –133, 2007.

[14] R. R. Harrison, R. J. Kier, C. A. Chestek, V. Gilja, P. Nuyujukian, S. Ryu, B. Greger, F. Solzbacher, and K. V. Shenoy, "Wireless Neural Recording With Single Low-Power Integrated Circuit," *IEEE Trans. Neural Syst. Rehabil. Eng.*, vol. 17, no. 4, pp. 322–9, 2009.

[15] M. Mollazadeh, K. Murari, G. Cauwenberghs, and N. Thakor, "Wireless Micropower Instrumentation for Multimodal Acquisition of Electrical and Chemical Neural Activity," *IEEE Trans. Biomed. Circuits Syst.*, vol. 3, no. 6, pp. 388–397, 2009.

[16] M. Catrysse, B. Hermans, and R. Puers, "An inductive power system with integrated bi-directional data-transmission," *Sensors and Actuators A: Physical*, vol. 115, no. 2, pp. 221–229, 2004.

[17] M. Contaldo, B. Banerjee, D. Ruffieux, J. Chabloz, E. Le Roux, and C. C. Enz, "A 2.4-GHz BAW-Based Transceiver for Wireless Body Area Networks," *IEEE Trans. Biomed. Circuits Syst.*, vol. 4, no. 6, pp. 391–399, 2010.

[18] M. Anis, M. Ortmanns, and N. Wehn, "Fully Integrated UWB Impulse Transmitter and 402-to-405MHz Super-Regenerative Receiver for Medical Implant Devices," in *Proc. IEEE Int. Symp. on Circuits Syst. (ISCAS)*, 2010, pp. 1213–1215.

[19] P. D. Bradley, "An Ultra Low Power, High Performance Medical Implant Communication System (MICS) Transceiver for Implantable Devices," *IEEE Conf. on Biomed. Circuits Syst.*, pp. 158–161, 2006.

[20] Q. Zhang, P. Feng, Z. Geng, X. Yan, and N. Wu, "A 2.4-GHz Energy-Efficient Transmitter for Wireless Medical Applications," *IEEE Trans. Biomed. Circuits Syst.*, vol. 5, no. 99, p. 1, 2011.

[21] A. Kahn, E. Chow, O. Abdel-Latief, and P. Irazoqui, "Low-power, high data rate transceiver system for implantable prostheses," *International journal of telemedicine and applications*, vol. 2010, p. 4, 2010.

[22] J. Jung, S. Zhu, P. Liu, Y.-J. E. Chen, and D. Heo, "22-pJ/bit Energy-Efficient 2.4-GHz Implantable OOK Transmitter for Wireless Biotelemetry Systems: In Vitro Experiments Using Rat Skin-Mimic," *IEEE Trans. Microw. Theory Tech.*, vol. 58, no. 12, pp. 4102–4111, 2010.

[23] A. Poon, S. O'Driscoll, and T. Meng, "Optimal frequency for wireless power transmission into dispersive tissue," *IEEE Trans. Antennas Propag.*, vol. 58, no. 5, pp. 1739–1750, 2010.

[24] M. Mark, T. Bjorninen, L. Ukkonen, L. Sydanheimo, and J. Rabaey, "Sar reduction and link optimization for mm-size remotely powered wireless implants using segmented loop antennas," in *Biomedical Wireless Technologies, Networks, and Sensing Systems (BioWireleSS), IEEE Topical Conference on.* IEEE, 2011, pp. 7–10.

[25] M. Loy and I. Sylla, "ISM-Band and Short Range Device Antennas," Texas Instruments, Tech. Rep., 2005.

[26] "Handset connectivity technologies: Executive summary," Berg Insight, Tech. Rep., 2012. [Online]. Available: http://www.berginsight.com/ReportPDF/Summary/bi-hct3-sum.pdf

[27] M. M. Ahmadi and G. A. Jullien, "A Wireless-Implantable Microsystem for Continuous Blood Glucose Monitoring," *IEEE Trans. Biomed. Circuits Syst.*, vol. 3, no. 3, pp. 169–180, 2009.

[28] A. J. Johansson, "Wireless communication with medical implants: Antennas and propagation," Ph.D. dissertation, Lund University, 2004.

[29] J. Rabaey, M. Mark, D. Chen, C. Sutardja, C. Tang, S. Gowda, M. Wagner, and D. Werthimer, "Powering and communicating with mm-size implants," in *Design, Automation Test in Europe Conference Exhibition (DATE), 2011*, Mar. 2011, pp. 1–6.

[30] S. Roundy, P. Wright, and J. Rabaey, *Energy scavenging for wireless sensor networks: with special focus on vibrations.* Springer, 2004.

[31] N. Mano, "A 280 μw cm- 2 biofuel cell operating at low glucose concentration," *Chemical Communications*, no. 19, pp. 2221–2223, 2008.

[32] J. Paradiso and T. Starner, "Energy scavenging for mobile and wireless electronics," *Pervasive Computing, IEEE*, vol. 4, no. 1, pp. 18–27, 2005.

[33] E. Reilly and P. Wright, "Modeling, fabrication and stress compensation of an epitaxial thin film piezoelectric microscale energy scavenging device," *Journal of Micromechanics and Microengineering*, vol. 19, p. 095014, 2009.

[34] A. Poon, "Miniaturization of implantable wireless power receiver," in *Engineering in Medicine and Biology Society (EMBC). Annual International Conference of the.* IEEE, 2009, pp. 3217–3220.

[35] D. J. Griffiths, *Introduction to Electrodynamics*, 3rd ed. Prentice Hall, 1999.

[36] C. Gabriel, "Compilation of the Dielectric Properties of Body Tissues at RF and Microwave Frequencies," DTIC Document, Tech. Rep., 1996.

[37] A. Poon, S. O'Driscoll, and T. Meng, "Optimal operating frequency in wireless power transmission for implantable devices," in *Engineering in Medicine and Biology Society (EMBS). 29th Annual International Conference of the IEEE.* IEEE, 2007, pp. 5673–5678.

[38] W. C. Chew, *Waves and Fields in Inhomogeneous Media.* Wiley-IEEE Press, 1999.

[39] A. Yakovlev, S. Kim, and A. Poon, "Implantable biomedical devices: Wireless powering and communication," *Communications Magazine, IEEE*, vol. 50, no. 4, pp. 152–159, Apr. 2012.

[40] A. V. Vorst, A. Rosen, and Y. Kotsuka, *RF/microwave interaction with biological tissues*, ser. Wiley series in microwave and optical engineering. Hoboken, N.J. : John Wiley & Sons : IEEE, c2006., 2006.

[41] K. Watanabe, K. Miyamoto, T. Masuda, and K. Shimizu, "Use of ultrasonography to evaluate thickness of the erector spinae muscle in maximum flexion and extension of the lumbar spine," *Spine*, vol. 29, no. 13, p. 1472, 2004.

[42] M. Mark, T. Bjorninen, Y. Chen, S. Venkatraman, L. Ukkonen, L. Sydanheimo, J. Carmena, and J. Rabaey, "Wireless channel characterization for mm-size neural implants," in *Engineering in Medicine and Biology Society (EMBC), Annual International Conference of the IEEE.* IEEE, 2010, pp. 1565–1568.

[43] S. O'Driscoll, A. Poon, and T. Meng, "A mm-sized implantable power receiver with adaptive link compensation," in *Solid-State Circuits Conference-Digest of Technical Papers (ISSCC).* IEEE, 2009, pp. 294–295.

[44] M. Zargham and P. Gulak, "Maximum achievable efficiency in near-field coupled power-transfer systems," *IEEE Trans. Biomed. Circuits Syst.*, vol. 6, no. 3, pp. 228–245, 2012.

[45] S. O'Driscol, "Adaptive signal acquisition and power delivery for implanted medical devices," Ph.D. dissertation, Stanford University, July 2009.

[46] J. Do, D. Akos, and P. Enge, "L and S bands Spectrum Survey in the San Francisco Bay Area," in *Position Location and Navigation Symposium (PLANS)*, Apr. 2004, pp. 566–572.

[47] S. Nagaraj, S. Khan, C. Schlegel, and M. Burnashev, "Differential preamble detection in packet-based wireless networks," *IEEE Trans. Wireless Commun.*, vol. 8, no. 2, pp. 599–607, Feb. 2009.

[48] "Sharing between the meteorological aids service and medical implant communication systems (MICS) operating in the mobile service in the frequency band 401-406 MHz," *ITU-R SA.1346*, 1998.

[49] P. Soontornpipit *et al.*, "Effects of radiation and sar from wireless implanted medical devices on the human body." *Journal of the Medical Association of Thailand*, vol. 95, pp. S189–97, 2012.

[50] N. Rezaei, D. Majumdar, B. Cockburn, and C. Schlegel, "Electromagnetic energy and data transfer in biological tissues using loop antennas," *Procedia Computer Science*, vol. 19, pp. 908–913, 2013.

[51] R. E. Ziemer, "Fundamentals of spread spectrum modulation," *Synthesis Lectures on Communications*, vol. 2, no. 1, pp. 1–79, 2007.

[52] D. Kurup, W. Joseph, G. Vermeeren, and L. Martens, "In-body path loss model for homogeneous human tissues," *Electromagnetic Compatibility, IEEE Transactions on*, vol. 54, no. 3, pp. 556 –564, Jun. 2012.

[53] ——, "In-body path loss model for homogeneous human muscle, brain, fat and skin," in *Antennas and Propagation (EuCAP), 2010 Proceedings of the Fourth European Conference on*, Apr. 2010, pp. 1–4.

[54] S. Gabriel, R. Lau, and C. Gabriel, "The dielectric properties of biological tissues: III. Parametric models for the dielectric spectrum of tissues," *Physics in Medicine and Biology*, vol. 41, p. 2271, 1996.

[55] A. Kiourti and K. Nikita, "Miniature scalp-implantable antennas for telemetry in the MICS and ISM bands: Design, safety considerations and link budget analysis," *IEEE Trans. Antennas Propag.*, vol. 60, no. 8, pp. 3568–3575, 2012.

[56] "Operation within the bands 902-928 MHz, 2400-2483.5 MHz, and 5725-5850 MHz," Federal Communications Commission (FCC), Tech. Rep. 15.247.

[57] "Operation within the bands 902-928 MHz, 2400-2483.5 MHz, 5725-5875 MHZ, and 24.0-24.25 GHz," Federal Communications Commission (FCC), Tech. Rep. 15.249.

[58] A. Alomainy and Y. Hao, "Modeling and characterization of biotelemetric radio channel from ingested implants considering organ contents," *Antennas and Propagation, IEEE Transactions on*, vol. 57, no. 4, pp. 999–1005, 2009.

[59] R. Moore, "Effects of a surrounding conducting medium on antenna analysis," *IEEE Trans. Antennas Propag.*, vol. 11, no. 3, pp. 216–225, 1963.

[60] A. Sani, A. Alomainy, and Y. Hao, "Numerical characterization and link budget evaluation of wireless implants considering different digital human phantoms," *IEEE Trans. Microw. Theory Tech.*, vol. 57, no. 10, pp. 2605–2613, 2009.

[61] XFDTD, *version 7.* State College, PA: Remcom, 2012.

[62] M. Ahmadi, B. Cockburn, and C. Schlegel, "Low power asynchronous packet-based baseband transceiver for wireless sensor networks," in *Proc. IEEE Int. Midwest Symp. on Circuits and Systems (MWSCAS)*, Aug. 2012, pp. 940–943.

[63] N. Rezaei, D. Majumdar, B. Cockburn, and C. Schlegel, "Power analysis of a smart neural prosthesis communications system," in *Proc. 6th Canadian Summer School on Communications and Information Technology (CSSCIT)*, Aug. 2011, pp. 30–31.

[64] D. Bol, R. Ambroise, D. Flandre, and J.-D. Legat, "Interests and Limitations of Technology Scaling for Subthreshold Logic," *IEEE Trans. VLSI Syst.*, vol. 17, no. 10, pp. 1508–1519, 2009.

[65] D. Bol, "Pushing ultra-low-power digital circuits into the nanometer era," Ph.D. dissertation, Universitè Catholique de Louvain, December 2008.

[66] W. Zhao and Y. Cao, "New Generation of Predictive Technology Model for Sub-45 nm Early Design Exploration," *IEEE Trans. Electron Devices*, vol. 53, no. 11, pp. 2816–2823, 2006.

[67] A. Sedra and K. Smith, *Microelectronic Circuits.* Oxford University Press, USA, 1998, vol. 1.

[68] M. Alioto and G. Palumbo, "NAND/NOR adiabatic gates: power consumption evaluation and comparison versus the fan-in," *IEEE Trans. Circuits Syst. I: Fundamental Theory and Applications*, vol. 49, no. 9, pp. 1253–1262, Sep. 2002.

[69] J. Rabaey, *Low power design essentials.* Springer Verlag, 2009.

[70] A. Chandrakasan and R. Brodersen, *Low power digital CMOS design.* Kluwer Academic Pub, 1995.

[71] K. Roy, S. Mukhopadhyay, and H. Mahmoodi-Meimand, "Leakage current mechanisms and leakage reduction techniques in deep-submicrometer CMOS circuits," *Proc. IEEE*, vol. 91, no. 2, pp. 305–327, Feb. 2003.

[72] O. C. Akgun, J. N. Rodrigues, Y. Leblebici, and V. Öwall, "High-level energy estimation in the sub-VT domain: Simulation and measurement of a cardiac event detector," *IEEE Trans. Biomed. Circuits Syst.*, vol. 6, no. 1, p. 15, 2012.

Appendix A

Code for Calculating Energy Consumption

Here is a MATLAB code to calculate the dynamic power consumption of the baseband transmitter. Note that for the NMOS on current, we have used data from a figure in [65]. It also includes some test procedures, which can be uncommented whenever needed.

```
function [] = DynamicEnergy ()
clear all; clc;
global Vdd NP Cg_ext Cg_nom Cj Cg_sub W_eff IsubN tech_label
    alpha;
alpha = 0.5;
Vdd = 0.2:0.001:0.5; % subthreshold supply voltage values, [
    Vdd] = V
% xdata_power/xdata_freq from Lund
% Vdd =
    [0.104000000000000,0.112000000000000,0.120000000000000,0.128000000000000,0

NP = 3; % ratio of PMOS width over NMOS width
% Cg_ext Cg_nom Cj Cg_sub have the unit of [F/m]
```

```
Cg_ext = [0.82 0.81 0.83 0.87 0.93 0.91 0.88] * (1e-15/1e-6);
Cg_nom = [0.43 0.5 0.61 0.72 0.85 0.85 0.85] * (1e-15/1e-6);
Cj = [0.3 0.325 0.36 0.4 0.46 0.51 0.58] * (1e-15/1e-6);
Cg_sub = [0.08 0.1 0.13 0.165 0.21 0.27 0.34] * (1e-15/1e-6);
% Width and length of devices in different technologies
L_eff = [12.6,17.5,24.5,35,49,70,120]*1e-9; % [L_eff] = m
W_eff = 1.5 * L_eff;
Ion_nom = [1290 1250 1150 1030 890 840 820] *(1e-6/1e-6); % [Ion_nom] = A/m
tech_label = [32, 45, 65, 90, 130, 180, 250];
tech_label_text = ['32', '45', '65', '90', '130', '180', '250'];
tech = 5:10:65;
eta = [238,185,135,100,75,60,50]; % DIBL coefficient, [eta] = mV/V
S = [99,93,89.5,87 ,85,86.85,88.7]; % subthreshold swing, [S] = mV/dec
Ioff_nom = [350,200,62,19,4.5,0.11,0.002]; % [Ioff_nom] = nA/um
Vdd_nom = [0.9,1.0,1.1,1.2,1.3,1.8,2.5]; % [Vdd_nom] = V
I0 = ( Ioff_nom .* 10.^( -(eta.*Vdd_nom)./S ) )*1e-9; % subthreshold reference current
                                                                        % [I0] = A/um
% plot(tech, I0, tech, Ioff_nom*1e-9);
```

```

% From Fig. 1.2 in p. 6 of Bol Thesis, we find the Ion vs Vdd for 130nm (fitted)
Ion_130nm_fit = 1.355e-10*exp(25.2*Vdd)*1e6;

IsubN = zeros(7,length(Vdd));
T_del = zeros(7,length(Vdd));
L_D = 7; % Logic depth
[~, ~, C_inv_FO4] = inverterPower(4, 1, 16e6); % Capacitance unit = F/m
for i = 1:7
    A=0; B=0;
    % Changing unit of W_eff to 'um'
    % Subthreshold leakage current of an NMOS, [IsubN] = A
    IsubN(i,:) = (W_eff(i)*1e6) .* I0(i) .* 10.^((eta(i).*Vdd)./S(i)) .* ...
        (1-exp(-Vdd/26e-3));

%     % Calculating the delay for one operation
%     A = L_D * (C_inv_FO4(i)*1e-6) .* Vdd; % Changing capacitance unit to F/um
%     B = I0(i) * 10.^( (((eta(i)*1e-3)+1).*Vdd)./(S(i)*1e-3) );
%     T_del(i,:) = A./B;
end

% %%% Test %%%
% figure;
% semilogy(Vdd, IsubN);
```

```
% title('Subtheeshold Current');
% legend('32 nm','45 nm','65 nm','90 nm','130 nm','180 nm','250 nm',2);

%%%%%%%%%%%

% % Testing MOSFET internal capacitance values
% plot(tech_label, Cj * (1e15/1e6),'-o', tech_label, Cg_ext* (1e15/1e6),'-o', tech_label, Cg_sub* (1e15/1e6),'-o', tech_label, Cg_nom* (1e15/1e6),'-o');
% xlabel('Technology node (nm)'); ylabel('C (fF/{\mum})');
% legend('Cj', 'C_{g,ext}', 'C_{g,sub}', 'C_{g,nom}');
% set(gca,'XTick',tech_label)
% set (gca, 'XTickLabel', {'32','45','65', '90', '130', '180', '250'});


% % plotting the subthreshold leakage current of an NMOS
% figure;
% % plot(Vdd, IsubN ./ (W_eff(i)*1e6)); % per width unit
% plot(Vdd, IsubN);
% legend('32', '45', '65', '90', '130', '180', '250');
% xlabel('Supply Voltage (V_{dd})'); ylabel('Leakage Current of NMOS (A)');

f2 = 5e6; % f_clck_chip
f1 = f2/16; % f_clk_bit
n = 16; % number of bits in shift register

```

```
% % Plotting the S and eta parameters
% [AX,H1,H2] = plotyy(tech,S,tech,eta,'plot');
% set(get(AX(1),'Ylabel'),'String','S');
% set(get(AX(2),'Ylabel'),'String','\eta');
% axes(AX(1)); axis([0 70 80 100]);
% axes(AX(2)); axis([0 70 0 400]);

% % Verifying the operation throughput constraint (T_op < T_del)
% T_op = 1/f1;
% for i = 1:7
%     for j = 1:length(Vdd)
%         if T_op < T_del(i,j)
%             fprintf('Throughput constraint violated in technology %1.0f nm and supply volyage %2.2f V\n',tech(i),Vdd(j));
%         end
%     end
% end

%%%%%%
% % Verifying throughput constraint in nominal voltage and different
% % technologies
% A = -1; % Inverter gain
% FO = 4;
% % Switching capacitance
% Cg_ext_eff = 0.5 * Cg_ext * (1-A);
% Cdyn_int = (Cg_ext_eff + Cj)*(1+NP);
```

```
% % Fan-out capacitance
% Cg_ext_eff_FO = 0.5 * Cg_ext + 0.5 * Cg_ext * (1-A);
% Cdyn_FO = FO * (1+NP) * (Cg_ext_eff_FO + Cg_nom);
% % Total switching capacitance at the output nodess
% Cdyn_nom = Cdyn_int + Cdyn_FO;
% T_del_nom = zeros(7,1);
% for i = 1:7
%       A=0; B=0;
%       % Calculating the delay for one operation
%       A = L_D * Cdyn_nom(i) * Vdd_nom(i);
%       B = Ion_nom(i);
%       T_del_nom(i,1) = A/B;
% end
% % Verifying the operation throughput constraint (T_op <
    T_del)
% T_op = 1/f1;
% for i = 1:7
%       if T_op < T_del_nom(i,1)
%             fprintf('Throughput constraint violated in
    technology %1.0f nm and nominal voltage\n',tech(i));
%       end
% end
%%%%%%

% Test function
testPowers;
%%%%%%%%%%

% Calculation total power consumption
```

```
[Pstat_shiftReg, Pdyn_shiftReg] = shiftRegisterPower(n,f2);
[Pstat_MUX, Pdyn_MUX] = MUXPower(f2);
[Pstat_diffEncoder, Pdyn_diffEncoder] = diffEncoderPower(f1);
[Pstat_flipFlop, Pdyn_flipFlop] = flipFlopPower(f1);
Pstat = 2*Pstat_shiftReg + Pstat_MUX + Pstat_diffEncoder + Pstat_flipFlop;
Pdyn = 2*Pdyn_shiftReg + Pdyn_MUX + Pdyn_diffEncoder + Pdyn_flipFlop;
Ptotal = Pstat + Pdyn;

% % Portion in 65 nm
% technology_number = 3;
% mux_portion =  (Pstat_MUX + Pdyn_MUX)./Ptotal;
% sr_portion =  (2*Pstat_shiftReg + 2*Pdyn_shiftReg)./Ptotal;
% diffEncoder_portion = ( Pstat_diffEncoder + Pstat_flipFlop + Pdyn_diffEncoder + Pdyn_flipFlop)./Ptotal;
% pie([mux_portion(technology_number,length(Vdd)),sr_portion(technology_number,length(Vdd)),diffEncoder_portion(technology_number,length(Vdd))])
% legend('Multiplexer','Shift Registers', 'Differential Encoder');

%%%% Plotting the Power %%%%
% scrsz = get(0,'ScreenSize');
% figure('Position',[scrsz(3)*0.01,scrsz(3)*0.04,scrsz(3)*0.87,scrsz(4)*0.5]); hold on;
% subplot(1,3,1);
```

```
% h = plot (Vdd, Pdyn*1e6, 'linewidth', 2);
% xlabel('V_{dd}[V]','fontsize',16); ylabel('P_{dyn}[\muW]','fontsize',16);
% legend('32 nm','45 nm','65 nm','90 nm','130 nm','180 nm','250 nm',2);
% set(gca, 'fontsize', 14);
% subplot(1,3,2);
% plot (Vdd, Pstat*1e6, 'linewidth', 2);
% xlabel('V_{dd}[V]','fontsize',16); ylabel('P_{stat}[\muW]','fontsize',16);
% legend('32 nm','45 nm','65 nm','90 nm','130 nm','180 nm','250 nm',2);
% set(gca, 'fontsize', 14);
% subplot(1,3,3);
% plot (Vdd, Ptotal*1e6, 'linewidth', 2);
% xlabel('V_{dd}[V]','fontsize',16); ylabel('E_{tot}/{op}[\muW]','fontsize',16);
% legend('32 nm','45 nm','65 nm','90 nm','130 nm','180 nm','250 nm',2);
% set(gca, 'fontsize', 14);
%%%%%%%%%%%%%%%%%%%%%%

% %%%%% Plotting power in a specific Vdd versus technology %%%%%
% plot(tech_label,Ptotal(:,length(Vdd))*1e6,'-o', tech_label,Pstat(:,length(Vdd))*1e6,'-o', tech_label,Pdyn(:,length(Vdd))*1e6,'-o', 'linewidth',2);
% xlabel('Technology node (nm)','FontSize',16); ylabel('Total power consumption (\muW)','FontSize',16);
```

```
% set(gca,'XTick',tech_label,'FontSize',12);
% set (gca, 'XTickLabel', {'32','45','65', '90', '130', '180', '250'});
% %%%%%%%%%%%%%%%%%%%%%%%%%%%%%%%%%%%%%%%%%%%%%%%%%%%%%%%%%%%%%%

%%%% Energy Consumption %%%%
[~, ~, Cdyn_NAND] = NANDPower(1, 0.5, 5e6, 2);
[~, ~, Cdyn_inv] = inverterPower(1, 0.5, 5e6);

IonN = zeros(7,length(Vdd)); % NMOS on current in subthreshold region
Tdel_NAND = zeros(7,length(Vdd));
Tdel_inv = zeros(7,length(Vdd));
ydata_freq = [0.0874554710859387,0.103865772714840,0.123722816510791,0.147769289731254,

scaling_factor = [1290 1250 1150 1030 890 840 820] *(1e-6/1e-6) / 890;
for i = 1:7
    % Subthreshold ON current of an NMOS, [IonN] = A
%     IonN(i,:) = (I0(i)*1e6) .* 10.^(((eta(i)+1).*Vdd)./S(i));
    IonN(i,:) = Ion_130nm_fit*(3.97/6.5)*scaling_factor(i); % first scaling is
    % to keep the same ration between dynamic and static (between Ion for multiplier used and our solution)
    % we know the ration in dynamic case
```

```
    % second scaling is technology scaling
    Ion_NAND(i,:) = 0.5 * 2 * (1+NP) * IonN(i,:);
    Ion_inv(i,:) = 0.5 * 1 * (1+NP) * IonN(i,:);
    Tdel_NAND(i,:) = (Cdyn_NAND(i)*Vdd)./Ion_NAND(i,:);
    Tdel_inv(i,:) = (Cdyn_inv(i)*Vdd)./Ion_inv(i,:);
    %%%
%       Estat(i,:) = Pstat(i,:) ./ ydata_freq;

end

% plotting Ion_NAND
% figure
% plot(IonN(5,:),Ion_130nm_fit);
% semilogy(Vdd, Ion_NAND(5,:),'k');
% legend('Ion-NAND test');
% hold on;
% semilogy(Vdd, Tdel_NAND(5,:));
% legend('Tdel-NAND test');
% semilogy(Vdd, 1./Ion_NAND(5,:),'r');

Tdel = 5*Tdel_NAND + Tdel_inv;
Edyn = Pdyn /f2;
Estat = Pstat .* Tdel;
Etotal = Edyn + Estat;

figure;
semilogy(Vdd,1./Tdel,'linewidth', 2);
title('Frequency','fontsize',16);
```

```
xlabel('V_{dd} [V]','fontsize',16); ylabel('Maximum Possible Frequency [Hz]','fontsize',16);
set(gca, 'fontsize', 14);

% plot(Vdd, (1./Tdel)/1e6,'linewidth',2);
% xlabel('V_{dd}[V]','fontsize',16); ylabel('Maximum Clock Frequency [MHz]','fontsize',16);
% legend('32 nm','45 nm','65 nm','90 nm','130 nm','180 nm','250 nm',2);
% set(gca, 'fontsize', 14);

%%%% Plotting the Energy per Operation %%%%%
scrsz = get(0,'ScreenSize');
figure('Position',[scrsz(3)*0.01,scrsz(3)*0.04,scrsz(3)*0.87,scrsz(4)*0.5]); hold on;
subplot(1,3,1);
semilogy (Vdd, Edyn, 'linewidth', 2);
xlabel('V_{dd}[V]','fontsize',16); ylabel('E_{dyn}[J]','fontsize',16);
legend('32 nm','45 nm','65 nm','90 nm','130 nm','180 nm','250 nm',2);
set(gca, 'fontsize', 14);
subplot(1,3,2);
semilogy (Vdd, Estat, 'linewidth', 2);
xlabel('V_{dd}[V]','fontsize',16); ylabel('E_{stat}[J]','fontsize',16);
legend('32 nm','45 nm','65 nm','90 nm','130 nm','180 nm','250 nm',2);
set(gca, 'fontsize', 14);
```

```
subplot(1,3,3);
semilogy (Vdd, Etotal, 'linewidth', 2);
xlabel('V_{dd}[V]','fontsize',16); ylabel('E_{tot}[J]','fontsize',16);
legend('32 nm','45 nm','65 nm','90 nm','130 nm','180 nm','250 nm',2);
set(gca, 'fontsize', 14);
hold on;
semilogy (Vdd, Estat, 'linewidth', 2, 'LineStyle', '-.');
legend('32 nm','45 nm','65 nm','90 nm','130 nm','180 nm','250 nm',2);
axis([0.2 0.5 1e-16 1e-13]);
%%%%%%%%%%%%%%%%%%%



%%%%%%%%%%%% New Code for Calibration - Power %%%%%%%%%%%%
figure;
plot(Vdd, Ptotal*1e6, 'linewidth', 2);
xlabel('V_{dd}[V]','fontsize',16); ylabel('P_{tot}[\muW]','fontsize',16);
legend('32 nm','45 nm','65 nm','90 nm','130 nm','180 nm','250 nm',2);
set(gca, 'fontsize', 14);

%%% Now trying to calibrate with Bol2009
% Energy numbers from Bol2009 for a multiplier
Edyn_Bol = 4.53e-15*exp(4.98*Vdd);
Estat_Bol = 2.47e-13*exp(-10.67*Vdd);
```

```
figure;
plot(Edyn(3,:), Edyn_Bol,'linewidth',2);
title('Dynamic Energy Calibration','fontsize',16);
xlabel('Calculated Dyncamic Energy','fontsize',14); ylabel('Dynamic Energy from [Bol2009] for a Multiplier','fontsize',14);
set(gca, 'fontsize', 14);

figure;
plot(Estat(3,:), Estat_Bol, 'linewidth', 2);
title('Static Energy Calibration','fontsize',16);
xlabel('Calculated Static Energy','fontsize',14); ylabel('Static Energy from [Bol2009] for a Multiplier','fontsize',14);
set(gca, 'fontsize', 14);
%%%%%%%%%%%%%%%%%%%%%%%%%%%%%%%%%%%%%%%%%%%%%%%%%%%%%%%%%%

%%%%%%%%%%%%%%%%%%%%%%%%%%%%%%%%%%%%%%%%%%%%%%%%%%%%%%%%%%%

% Calculating the energy consumption with consideration of throughput
% constraint
% T_op = 1/f1;
% for i = 1:7
%     startV = 0;
%     for j = 1:length(Vdd)
%         if T_op < T_del(i,j)
%             fprintf('Throughput constraint violated in technology %1.0f nm and supply volyage %2.3f V\n',tech(i)
```

```
,Vdd(j));
%             else
%                 if startV == 0
%                     startV = 1;
%                     numberV(i) = j; % The first place that throughput validation is satisfied
%                     fprintf('First valid voltage at %3.0f nm technology is: %2.3f V\n', tech(i), Vdd(numberV(i)));
%                 end
%                 Estat(i,j) = Pstat(i,j) * T_del(i,j);
%                 Edyn(i,j) = Pdyn(i,j) * T_del(i,j);
%                 Etot(i,j) = Estat(i,j) + Edyn(i,j);
%             end
%         end
%         if startV ==0
%             numberV(i) = length(Vdd);
%             Estat(i,:)=zeros(1,length(Vdd));
%             Edyn(i,:)=zeros(1,length(Vdd));
%             Etot(i,:)=zeros(1,length(Vdd));
%         end
% end
% figure; hold on;
% for i = 1:7
%         plot(Vdd(numberV(i):length(Vdd)), Estat(i, numberV(i):length(Estat(i,:))));
% end
% figure; hold on;
% for i = 1:7
```

```
%       plot(Vdd(numberV(i):length(Vdd)), Edyn(i, numberV(i):length(Edyn(i,:))));
% end
% figure; hold on;
% for i = 1:7
%       plot(Vdd(numberV(i):length(Vdd)), Etot(i, numberV(i):length(Etot(i,:))));
% end
end

function [] = testPowers()
global Vdd NP Cg_ext Cg_nom Cj Cg_sub W_eff IsubN tech_label;
% List of technology nodes for testing purposes
% tech = [32 45 65 90 130 180 250];
%%%% Just for test %%%%
% plot(tech,Cg_ext, tech,Cg_nom, tech,Cj, tech,Cg_sub);
% legend('Cg\_ext','Cg\_nom','Cj','Cg\_sub');
% [Pstat_inverter, Pdyn_inverter, C_inv_FO4] = inverterPower(4, 1, 16e6);
% plot(tech_label, C_inv_FO4 * (1e15/1e6));
% xlabel('Technology node (nm)'); ylabel('C_{INV,FO4} (fF/{\mum})');
% set(gca,'XTick',tech_label);
% set (gca, 'XTickLabel', {'32','45','65', '90', '130', '180', '250'});
% plot (Vdd, Pdyn_inverter);
% plot (Vdd, Pstat_inverter);
% legend('32', '45', '65', '90', '130', '180', '250');
```

```
% xlabel('Supply Voltage (V_{dd})'); ylabel('Static power consumption of an inverter (W)');
% xlabel('Supply Voltage (V)'); ylabel('Dynamic power consumption of a FO4 inverter (W)');
% [Pstat_NAND, Pdyn_NAND, Cdyn_NAND] = NANDPower(4, 1, 16e6, 2);
% plot (Vdd, Pdyn_NAND)
% [Pstat_NOR, Pdyn_NOR] = NORPower(4, 1, 16e6, 2);
% plot (Vdd, Pdyn_NOR)
% [Pstat_XOR, Pdyn_XOR] = XORPower(16e6);
% plot (Vdd, Pdyn_XOR)
% [Pstat_flipFlop, Pdyn_flipFlop] = flipFlopPower(16e6);
% plot (Vdd, Pdyn_flipFlop)
% [Pstat_shiftReg, Pdyn_shiftReg] = shiftRegisterPower(16,16e6);
% plot (Vdd, Pdyn_shiftReg)
% [Pstat_diffEncoder, Pdyn_diffEncoder] = diffEncoderPower(16e6);
% plot (Vdd, Pdyn_diffEncoder)
% [Pstat_MUX, Pdyn_MUX] = MUXPower(16e6);
% plot (Vdd, Pdyn_MUX)
end

function [Pstat, Pdyn, Cdyn] = inverterPower(FO, alpha, f)
global Vdd NP Cg_ext Cj Cg_sub W_eff IsubN;
% FO: fan-out number
% Tdel: operation delay
% alpha: switching factor
A = -1; % Inverter gain
```

```
% Switching capacitance
Cg_ext_eff = 0.5 * Cg_ext * (1-A);
Cdyn_int = (Cg_ext_eff + Cj)*(1+NP);
% Fan-out capacitance
Cg_ext_eff_FO = 0.5 * Cg_ext + 0.5 * Cg_ext * (1-A);
Cdyn_FO = FO * (1+NP) * (Cg_ext_eff_FO + Cg_sub);
% Total switching capacitance at the output nodess
Cdyn = Cdyn_int + Cdyn_FO;
% Leakage current
I_leak_inv = IsubN * 0.5 * (1+NP);
% %%%%% Testing Inverter Leakage %%%%
% figure;
% plot(Vdd, I_leak_inv);
% legend('32', '45', '65', '90', '130', '180', '250');
% xlabel('Supply Voltage (V)'); ylabel('Leakage Current of an inverter (A)');
% %%%%%%%%%%%%%%%%%%%%%%%%%%%%%%%%%%%
Pdyn = zeros(7,length(Vdd)); Pstat = zeros(7,length(Vdd));
for i = 1:7
    Pdyn(i,:) = 0.5 * alpha * Cdyn(i) * Vdd.^2 .* W_eff(i) * f;
    Pstat(i,:) = Vdd .* I_leak_inv(i);
end
end

function [Pstat, Pdyn, Cdyn] = NANDPower(FO, alpha, f, m)
global Vdd NP Cg_ext Cj Cg_sub W_eff IsubN;
% FO: fan-out number
% Tdel: operation delay
```

```
% alpha: switching factor
% m: number of inputs
A = -1; % Inverter gain
% Switching capacitance
Cg_ext_eff = 0.5 * Cg_ext * (1-A);
Cdyn_int = m*(Cg_ext_eff + Cj)*(1+NP);
% Fan-out capacitance
Cg_ext_eff_FO = 0.5 * Cg_ext + 0.5 * Cg_ext * (1-A);
Cdyn_FO = FO * (1+NP) * (Cg_ext_eff_FO + Cg_sub);
% Total switching capacitance at the output node
Cdyn = Cdyn_int + Cdyn_FO;
% Leakage current
I_leak_NAND = IsubN * 0.5 * m * (1+NP);
Pdyn = zeros(7,length(Vdd)); Pstat = zeros(7,length(Vdd));
for i = 1:7
    Pdyn(i,:) = 0.5 * alpha * Cdyn(i) * Vdd.^2 .* W_eff(i) *
        f;
    Pstat(i,:) = Vdd .* I_leak_NAND(i);
end
end

function [Pstat, Pdyn] = NORPower(FO, alpha, f, m)
global Vdd NP Cg_ext Cj Cg_sub W_eff;
% FO: fan-out number
% Tdel: operation delay
% alpha: switching factor
% m: number of inputs
A = -1; % Inverter gain
% Switching capacitance
```

```
Cg_ext_eff = 0.5 * Cg_ext * (1-A);
Cdyn_int = m*(Cg_ext_eff + Cj)*(1+NP);
% Fan-out capacitance
Cg_ext_eff_FO = 0.5 * Cg_ext + 0.5 * Cg_ext * (1-A);
Cdyn_FO = FO * (1+NP) * (Cg_ext_eff_FO + Cg_sub);
% Total switching capacitance at the output node
Cdyn = Cdyn_int + Cdyn_FO;
% Leakage current
I_leak_NOR = IsubN * 0.5 * m * (1+NP);
Pdyn = zeros(7,length(Vdd)); Pstat = zeros(7,length(Vdd));
for i = 1:7
    Pdyn(i,:) = 0.5 * alpha * Cdyn(i) * Vdd.^2 .* W_eff(i) *
        f;
    Pstat(i,:) = Vdd .* I_leak_NOR(i);
end
end

function [Pstat, Pdyn] = XORPower(f)
global alpha;
FO_avg = 1.25;
% alpha = 1;
[Pstat_NAND, Pdyn_NAND,Cdyn_NAND] = NANDPower(FO_avg, alpha,
    f, 2);
Pstat = Pstat_NAND * 4;
Pdyn = Pdyn_NAND * 4;
end

function [Pstat, Pdyn] = flipFlopPower(f)
global alpha;
```

```
FO_NAND3 = 2; FO_NAND2_avg = 2;
% alpha = 1;
[Pstat_NAND2, Pdyn_NAND2,Cdyn_NAND2] = NANDPower(
    FO_NAND2_avg, alpha, f, 2);
[Pstat_NAND3, Pdyn_NAND3,Cdyn_NAND3] = NANDPower(FO_NAND3,
    alpha, f, 3);
Pstat = Pstat_NAND2 * 5 + Pstat_NAND3;
Pdyn = Pdyn_NAND2 * 5 + Pdyn_NAND3;
end

function [Pstat, Pdyn] = shiftRegisterPower(n,f)
global alpha;
FO_inverter = n-1; FO_NAND = 1;
% alpha = 1;
[Pstat_inverter, Pdyn_inverter, C_inv_FO4] = inverterPower(
    FO_inverter, alpha, f);
[Pstat_NAND, Pdyn_NAND, Cdyn_NAND] = NANDPower(FO_NAND,
    alpha, f, 2);
[Pstat_flipFlop, Pdyn_flipFlop] = flipFlopPower(f);
Pstat = Pstat_inverter + 3*(n-1)*Pstat_NAND + n*
    Pstat_flipFlop;
Pdyn = Pdyn_inverter + 3*(n-1)*Pdyn_NAND + n*Pdyn_flipFlop;
end

function [Pstat, Pdyn] = diffEncoderPower(f)
[Pstat_XOR, Pdyn_XOR] = XORPower(f);
[Pstat_flipFlop, Pdyn_flipFlop] = flipFlopPower(f);
Pstat = Pstat_XOR + Pstat_flipFlop;
Pdyn = Pdyn_XOR + Pdyn_flipFlop;
```

```
end

function [Pstat, Pdyn] = MUXPower(f)
global alpha;
FO_NAND = 1; FO_inverter = 1;
% alpha = 1;
[Pstat_inverter, Pdyn_inverter, C_inv_FO4] = inverterPower(
    FO_inverter, alpha, f);
[Pstat_NAND, Pdyn_NAND, Cdyn_NAND] = NANDPower(FO_NAND,
    alpha, f, 2);
Pstat = Pstat_inverter + 3*Pstat_NAND;
Pdyn = Pdyn_inverter + 3*Pdyn_NAND;
end
```